

Methods for Building Self-Folding Machines

A dissertation presented
by
Samuel Makepeace Felton
to
The School of Engineering and Applied Sciences
in partial fulfillment of the requirements
for the degree of
Doctor of Philosophy
in the subject of
Engineering Sciences

Harvard University
Cambridge, Massachusetts
April 2015

© 2015 -*Samuel Makepeace Felton*
All rights reserved.

Dissertation Advisor:

Robert J. Wood

Author:

Samuel Makepeace Felton

Methods for Building Self-Folding Machines

Abstract

Origami can turn a sheet of paper into complex three-dimensional shapes, and similar folding techniques can be used to build structures and mechanisms. However, folding by hand can be difficult and time consuming. This has led to the development of self-folding materials that transform themselves from flat sheets into 3D shapes by bending themselves along hinges. A variety of self-folding methods have been demonstrated at a variety of length scales, but they have not yet been used to build complex machines.

This dissertation demonstrates that self-folding can produce functional machines with a new laminate we refer to as a shape memory composite. We characterize the behavior of this composite with models and experimental data, and use this information to develop design rules for self-folding. We apply these rules to create devices at multiple length scales, including a model crane, a crawling robot, a lamp, and a model ship.

Contents

1	Introduction	1
1.1	Folding in Art	1
1.2	Folding in Mathematics	2
1.3	Linkages	3
1.4	Folding in Nature	4
1.5	Folding in Engineering	5
1.6	Printable Manufacturing	6
1.7	Self-Folding	7
1.8	Contributions and Chapter Organization	8
2	Self-Folding a Machine	10
2.1	Introduction	10
2.2	Design	12
2.2.1	Composite Design	12
2.2.2	Inchworm Design	14
2.2.3	Angle Control	15
2.2.4	Circuit Design	16
2.3	Fabrication	16
2.4	Results	17
2.5	Discussion	18
3	Models for Self-Folding Hinges	20
3.1	Introduction	20
3.2	Unidirectional Electrical Folding	21
3.2.1	Design and Fabrication	21
3.2.2	Model Design	22
3.2.3	Thermal Behavior	22
3.2.4	Torque Behavior	29
3.2.5	Free Displacement Behavior	33
3.2.6	Sample Structures	35
3.3	Bidirectional Electrical Folding	36
3.3.1	Design	36
3.3.2	Thermal Behavior	37
3.3.3	Torque Behavior	39

3.3.4	Maximum Feature Size	40
3.3.5	Minimum Feature Size	41
3.3.6	Angle Control	42
3.4	Uniformly Activated Folding	43
3.4.1	Design	43
3.4.2	Maximum Feature Size	44
3.4.3	Angle Control	45
3.4.4	Sample Structures	46
3.5	Discussion	47
4	Practical Self-Folding	49
4.1	Introduction	49
4.2	Design	50
4.2.1	Geometries	50
4.2.2	Mechanisms	52
4.2.3	Autonomous Folding	55
4.3	Fabrication	57
4.4	Results	58
4.5	Discussion	59
4.5.1	Design Process	59
4.5.2	Adaptability	60
4.5.3	Energy Consumption	61
4.5.4	Manufacturing Comparison	63
5	Sensors for Self-Folding Machines	66
5.1	Introduction	66
5.2	Capacitive Touch Sensor	67
5.2.1	Model	68
5.2.2	Results	69
5.3	Mechanical Switch	69
5.4	Electromagnetic Velocity Sensor	71
5.4.1	Model	71
5.4.2	Results	73
5.5	Lamp	74
5.6	Discussion	75
6	Self-Folding at the Millimeter Scale	77
6.1	Introduction	77
6.2	First Generation	78
6.2.1	Composite Design	78
6.2.2	Fabrication	79
6.2.3	Models and Results	80
6.3	Second Generation	83
6.3.1	Composite Design	83

6.3.2	Fabrication	85
6.3.3	Models and Results	86
6.4	Discussion	92
7	Future Work and Conclusion	95
7.1	Introduction	95
7.2	Improving Shape Memory Composites	96
7.3	Alternative Self-Folding Methods	97
7.3.1	Pneumatics	97
7.3.2	Shape Memory Alloys	98
7.3.3	3D Printing	98
7.4	Components	99
7.4.1	Printable Sensors	99
7.4.2	Printable Actuators	99
7.5	Conclusion	100
Appendix A	Parts and Materials	112
A.1	Inchworm Composite	112
A.2	Inchworm Composite Cost	112
A.3	Unidirectional Paper Composite	112
A.4	Bidirectional Paper Composite	112
A.5	Bidirectional Composite Cost	113
A.6	Uniformly Heated Paper Composite	113
A.7	Uniformly Heated Composite Cost	113
A.8	Crawling Robot Components	113
A.9	Millimeter-Scale Composite 1	113
A.10	Millimeter-Scale Composite 2	114
Appendix B	Thermal Model	115
B.1	Solution for PDE	115
B.2	Derivation of Convection Coefficient	115
B.3	1D Approximation	119
B.4	Derivation of Bulk Conductivity and Diffusivity Terms	120
B.5	Derivation of Core Convection Term	120
B.6	Validation of Core Convection Approximation	121
B.7	Derivation of Dissipation Term	122
B.8	Derivation of Regime Transition Time	122
B.9	Validation of Regime Transition Model	124
B.10	Explanation of the Virtual Surface Thickness	124
Appendix C	Mechanical Model	126
C.1	Values for Determining Maximum Face Size	126
C.1.1	Bidirectional Composite	126
C.1.2	Uniformly Heated Composite	126
C.1.3	Millimeter Scale Composite	126

C.2	Shape Memory Polymer Characterization	127
C.2.1	Thick Polyolefin	127
C.2.2	Polystyrene	128
C.2.3	Thin Polyolefin	128
C.3	Angular Dependence of Hinge Torque	130
Appendix D Manufacturing Estimates		134
D.1	3D Printing	134
D.2	Injection Molding	134
D.3	Milling	136
D.4	Sheet Metal Stamping	136
D.5	Resistive Self-Folding	138
D.6	Oven Self-Folding	138

To my wife Sarah.

Author List

The following authors contributed to this thesis:

Dr. Daniel Aukes, to Chapter 6

Kaitlyn Becker, to Chapter 6

Prof. Erik Demaine, to Chapters 1, 3, and 4

Prof. Cagdas Onal, to Chapters 2 and 3

Prof. Daniela Rus, to Chapters 2, 3, and 4

Brian Shin, to Chapters 3 and 5

Prof. Michael Tolley, to Chapters 2, 3, 4, 5, and 6

Acknowledgments

I would first like to thank Rob Wood for giving me the opportunity to work in his lab and on this project. His guidance was instrumental in everything that we've achieved. I owe a great deal to the rest of the Harvard Microrobotics Lab as well. Numerous people contributed to this work in both large and small ways. Thank you to Dan Aukes, Kait Becker, Brian Shin, and Mike Tolley, and for the hard work they contributed to this research. Thank you to Mike Smith and Hetchen Ehrenfeld for their assistance with the all of the equipment and logistics involved with research. Thank you to Daniel Vogt for assistance with all things related to 3D printing. Thank you to my collaborators at other institutions for their time and expertise, including Erik Demaine, Sangbae Kim, Daniela Rus, and Joseph Sun at MIT; Kyu-Jin Cho and Dae-Young Lee at Seoul National University; and Cagdas Onal at WPI.

Research costs money, and I'd like to thank the National Defense Science and Engineering Fellowship, the National Science Foundation, the Wyss Institute, and the School of Engineering and Applied Sciences for their financial support.

Finally, I'd like to thank my friends and family for the encouragement, advice, and help that has allowed me to reach this point. Thank you to my parents and my sister Anna for their love and support for every step I've made in my life. Thank you to my wife Sarah for your unwavering patience, your daily support, and being the best partner in life I could hope for.

The secret to productivity in so many fields—and in origami—is letting dead people do your work for you.

Robert Lang

1

Introduction

1.1 Folding in Art

Origami is a Japanese art form in which paper is folded into intricate 2D and 3D shapes (Figure 1.1A). This and other types of paper-folding represent an interesting fusion of art and math. Artistically, the folder must decide what shapes they want to express and the appropriate folds for creating them [1, 2]. In many cases there are multiple fold patterns which can produce similar geometries but vary aesthetically, such as producing smooth, wrinkled, or tightly ribbed surfaces. Many origamists also choose to represent shapes derived from existing forms, such as animals or flowers, and must select which features to include and which to abstract away.

From a technical perspective, origami can be abstracted to a geometric problem in which each face of a folded structure is an infinitesimally thin polygon and each fold a line segment. This enables the experienced folder to predict the final geometry from a given

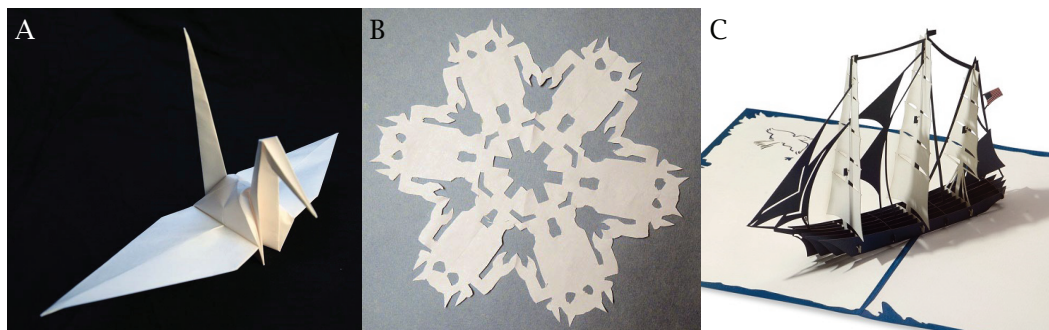


Figure 1.1: Folding is the basis for several artistic disciplines. (A) An origami crane. (B) An example of kirigami. (C) A pop-up card (©2014 LovePop).

fold pattern, even though the untrained observer may see no relation between the two. To be a skilled origamist requires talent in both of these areas.

Origami is not the only fold-based art form. Kirigami is a related discipline in which a single piece of paper is folded and cut (Figure 1.1B) [3]. This is commonly used today to make snowflake patterns. Pop-up books and cards use multiple sheets of paper, folded and glued together, to create a mechanism with a single rotational degree of freedom that lies flat in one configuration, and pops into a 3D shape when ‘opened’ or unfolded (Figure 1.1C) [4, 5]. In all of these art forms there is a mathematical relationship between the fold and cut lines and the final shape. Perhaps because of this, the lessons learned in origami can be applied to both artistic endeavors and technical problems.

1.2 Folding in Mathematics

Computational origami is a relatively new branch of mathematics that explores the geometric nature of folding [6]. It has resulted in important proofs regarding the capabilities of folding to produce arbitrary shapes. In 2001, it was proven that a single rectangular piece of paper could be folded into any polygon or polyhedral shell [7]. While this was the first proof of universality for origami, it was practically infeasible. The solution resembles a strip of paper wrapped back and forth, resulting in wasted paper and folds through multiple layers. A more practical solution was developed in the form of Origamizer, a free software program which can generate a fold pattern for a given polyhedron (Figure 1.2) [8]. Originally applicable to a wide range of polyhedra, a similar algorithm was later proved to be universally applicable to any polyhedron [9].

Other capabilities of folding have been mathematically demonstrated as well. Ben-

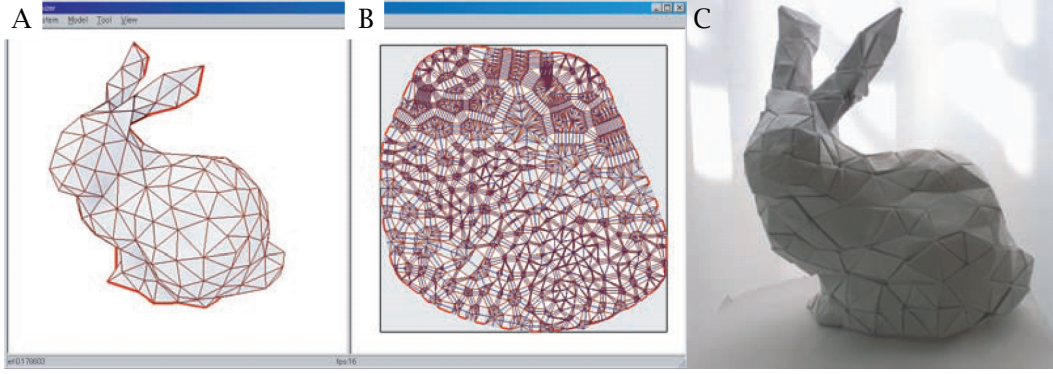


Figure 1.2: Origamizer is a free computer program capable of transforming a polyhedron into a planar crease pattern (source: Tachi [8] ©2010 IEEE). (A) A polyhedral model approximating the Stanford bunny. (B) The planar fold pattern generated from the model using the Origamizer algorithm. (C) The folded model.

bernou et al. developed and demonstrated a universal fold pattern that is capable of reproducing any shape made of unit cubes [10]. Abel et al. developed algorithms for designing pop-up cards, and proved any polygon can be deployed under a variety of conditions by opening the structure [11]. These and other results provide an extensive framework with which to study and use folding.

1.3 Linkages

Linkages are a common class of mechanisms comprising an interconnected set of rigid elements and freely-rotating joints [6]. Folded sheets can be treated as linkage mechanisms in which each face represents a rigid element and each fold a joint with a single degree of freedom. Because of this relation, linkages provide a framework for studying the kinematics of folded structures, and computational geometry has established that a broad range of kinematic results are possible.

The Kempe Universality Theorem states that a 2D linkage system can trace any polynomial curve. The first published proof of this theorem established a more general result, allowing the trace of any algebraic set defined by a system of polynomials [12]. This proof was subsequently simplified and generalized to an asymptotically optimal algorithm for linkage construction in arbitrary dimensions [13]. Furthermore, a practical algorithm has been developed that generates a linkage design which approximates a desired motion (as required by a robot, for example) [14].

1.4 Folding in Nature

Folded structures and mechanisms exist in nature at a wide range of length scales. For example, most proteins start as a peptide chain and fold themselves into their functional shape [15]. Proteins will also use folding to modulate their function [16]; tyrosine kinases are enzymes that can be switched between active and inactive states by a partial unfolding in the catalytic domain (Figure 1.3A) [17], and RNA folding alters its proton binding behavior [18].

Similar behavior can be seen at larger scales as well; the *Schrankia microphylla* plant will fold its leaves and expose thorns as a defense mechanism [19]. Folding is used to increase the surface area inside a constrained volume such as the human brain (Figure 1.3B) [20] or the inner surface of the intestine, which is folded at different length scales into *plicae circulares*, villi, and microvilli, increasing the surface over 600-fold [21, 22]. Folded patterns can also be used to deploy large structures such as leaves [23], and dynamic folding mechanisms allow insect wings to fold beneath their rigid carapace (Figure 1.3C) [24].

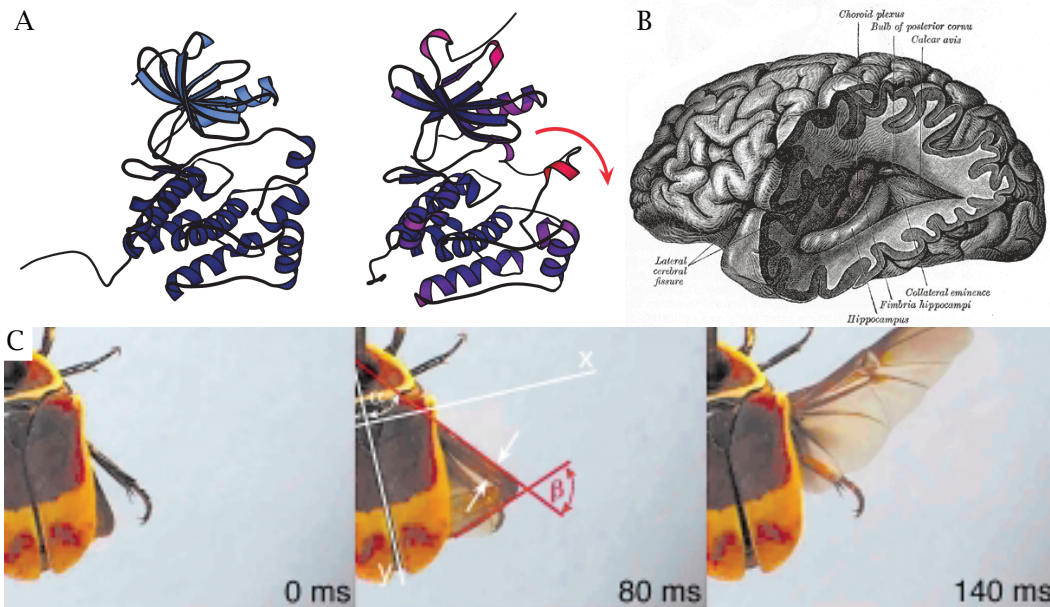


Figure 1.3: Natural systems use folded structures in a variety of ways. (A) Proteins can fold and unfold to change their functionality (source: Yang et al. [17]). (B) The human brain is folded, increasing its surface area (source: Gray [21]). (C) Beetle wings fold underneath their carapace for protection (source: Haas et al. [25] ©2001 Elsevier).

1.5 Folding in Engineering

Folded structures and mechanisms have also been used in a variety of engineering applications. Folded materials are used to create stiff, lightweight structures such as corrugated sheets (Figure 1.4A) [26], and devices with a large surface area can be folded into small volumes to make transportation and storage easier. This has applications in shipping [27], satellite deployment in space (Figure 1.4B) [28, 29], disaster response [30, 31], and military expeditionary capabilities (Figure 1.4C) [32].

Folding can produce sophisticated mechanisms by creating different functional components from a single sheet: A hinge can act as a flexural spring or a freely rotating joint, while a flat face can be a leaf spring or a rigid plate. These elements have been combined to create folded devices such as origami wheels that change shape for increased mobility or performance (Figure 1.4D) [33, 34], and an electroactive film that is folded into a bi-morph actuator (Figure 1.4E) [35]. Folded structures can replicate mechanical joints with many degrees-of-freedom and arbitrary ranges-of-motion (Figure 1.4F) [36], and flexure joints have operational advantages over more traditional bearing joints, including negligible friction losses and monolithic construction [37, 38]. Springs and other features can even be embedded in laminate structures, resulting in 3D mechanisms that emerge from

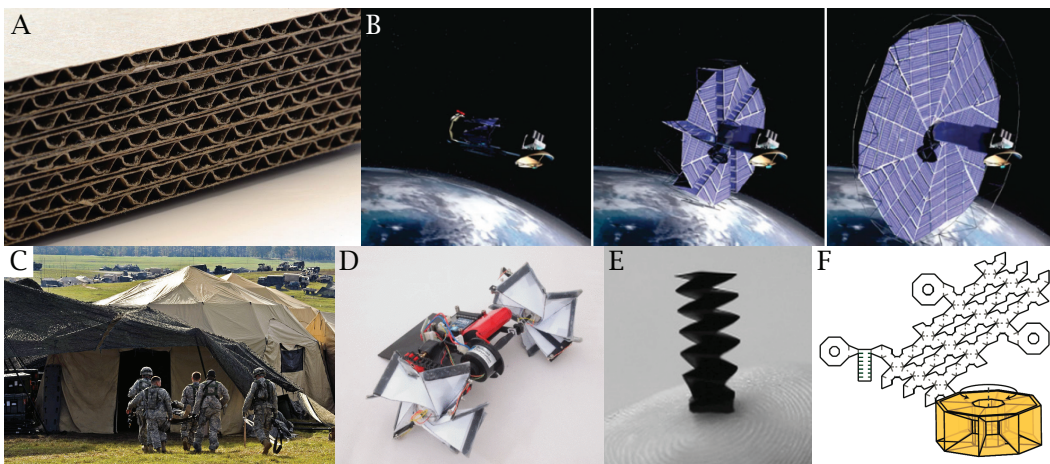


Figure 1.4: Folded structures are used in engineering for a variety of purposes. (A) Corrugation in cardboard increases its stiffness without significantly increasing its weight. (B) Folding can be used to fit a large solar panel into a small volume for deployment in space (source: Zirbel et al. [29] ©2010 ASME). (C) Tents and other foldable structures are critical for the military's expeditionary operations (source: TSgt. Joselito Aribuabo, USAF). (D) An origami wheel that can change its radius (source: Lee et al. [33] ©2013 IEEE). (E) An actuator folded out of paper (source: Okuzaki et al. [35]). (F) Folding can create a variety of functional transmissions, including this rotary joint (source: Sung et al. [36] ©2013 ASME).

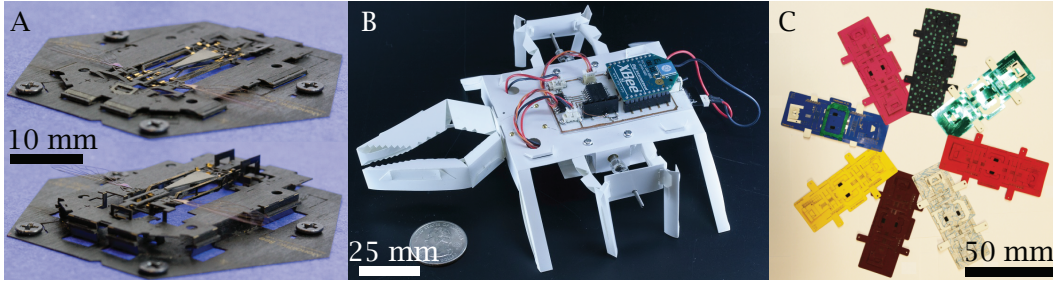


Figure 1.5: Complete, functional machines can be built by folding flat materials. (A) A robotic bee assembled using Pop-Up Book MEMS (Source: Sreetharan et al. [40] ©2013 IOP Publishing). (B) A printed origami robot folded from a sheet of plastic (source: Onal et al. [44] ©2015 IEEE). (C) Several copies of the Foldscope, a folded microscope (source: Cybulski et al. [45]).

flat sheets [39].

Complete and functional machines have been made by folding flat laminates. Many mesoscale robots have been built by folding carbon-fiber laminates, including the flying RoboBee (Figure 1.5A) [40] and the crawling HAMR [41] and myriapod robot [42]. These robots are machined using lasers and lithographic etching and then folded into their functional 3D form because 2D machining methods are easier at the millimeter scale than more traditional methods such as milling and lathing. Larger machines have been folded from sheets of plastic and paper in order to reduce manufacturing costs, including robots (Figure 1.5B) [43, 44] and microscopes (Figure 1.5C) [45]. This fabrication style has led to the creation of algorithmic design tools for folding, which harness the computational nature of origami. PopupCAD is a design program tailored for designing laminate folded structures [46], and geometric algorithms can compose cut-and-fold patterns for a given machine geometry [47].

1.6 Printable Manufacturing

Our interest in origami-inspired engineering comes from our goal of printable manufacturing—methods for quickly and inexpensively building machines from digital plans with a minimal amount of capital investment and training. This capability is most often associated with 3D printing, and research has shown that additive manufacturing is capable of functional components such as actuators [48], sensors [49], and batteries [50]. However, planar fabrication has its own advantages. In addition to the benefits of folded structures listed above such as high strength-to-weight ratios and low costs, these structures are often faster to fabricate because only a limited number of layers (generally less than 10 for

our applications) need to be machined. In comparison, when a 3D printer builds a structure, it must deposit each layer individually up to the final structural height, resulting in hundreds or thousands of layers. Planar manufacturing also has a large number of machining and assembly options, including laser and water jet cutting, lithography, etching, spin coating, and pick-and-place installation of discrete components. Despite these advantages, folded manufacturing has one noticeable limitation. Although the unfolded sheets can be machined quickly, it can be time-consuming and difficult to fold them by hand. For this reason, we wanted to develop a method for the machines to fold themselves.

1.7 Self-Folding

Self-folding is a fabrication technique in which a flat structure bends itself along hinges, resulting in 3D features [51]. A variety of self-folding methods have already been demonstrated. One method relies on differential stress between two layers in a laminate. This stress can be induced by a temperature increase in thermally mismatched materials [52] or swelling a hydrogel on contact with water (Figure 1.6D) [53]. Alternatively, one layer can be prestressed during fabrication and then physically constrained by a sacrificial layer until released for self-folding (Figure 1.6B-C) [54]. This technique is often used for sub-millimeter features and sub-micron thick films in which only a small stress is necessary to induce folding. Folding is usually activated by a global stimulus, resulting in simultaneous folding of all hinges. However, there are examples of focusing the stimulus on individual hinges to achieve sequential folding [55].

Another class of self-folding utilizes shape memory alloy hinges. These hinges are mechanically preprogrammed, first by bending them into their folded state, then heating, unfolding, and cooling them. They retain their unfolded shape until heated, at which point they fold again. These hinges have been installed as discrete components connecting rigid faces (Figure 1.6G) [56] and programmed along a single nitinol wire to demonstrate self-tying knots [57]. This technique is often used when hinges need to be folded individually because each hinge can be heated separately.

There are a variety of other self-folding techniques that are actuated by magnetic fields (Figure 1.6A) [58], capillary forces (Figure 1.6E) [59], pneumatics (Figure 1.6F) [60], or shape memory polymers (Figure 1.6H) [61]. The method used often depends on its application, and these applications usually fall into two categories. The first is in the assembly of

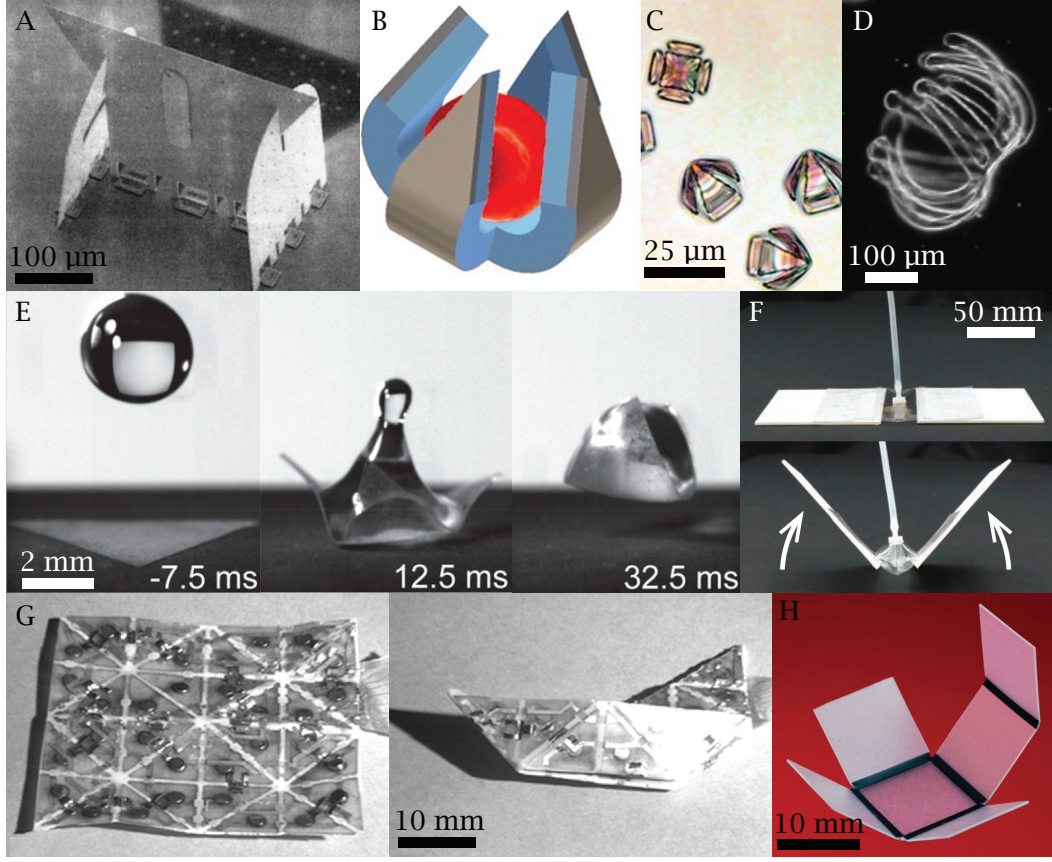


Figure 1.6: A variety of self-folding techniques have been developed that are actuated by many different phenomena and materials, including: (A) magnetic fields (source: Yi et al. [58] ©1999 IEEE), (B-C) prestressed layers (source: Malachowski et al. [62] ©2014 ACS), (D) polymer swelling (source: Guan et al. [53] ©2005 ACS), (E) capillary forces (source: Antkowiak et al. [59]), (F) pneumatic pouches (source: Niiyama et al. [60] ©2014 IEEE), (G) shape memory alloys (source: Hawkes et al. [56]), and (H) shape memory polymers (source: Liu et al. [61] ©2012 RSC).

structures that are difficult to reach or manipulate. Examples include self-folding within the body [62], in space [29], or at sizes that are too small for manual manipulation [63]. The second application is to speed up and parallelize foldable structures. For example, a manually folded robot can take up to one hour to fold by hand [44]. A similarly sized self-folding robot can fold itself in about five minutes [64].

1.8 Contributions and Chapter Organization

The purpose of this dissertation is to determine if self-folding can produce functional structures and machines, and if so, develop design rules and determine the limitations of self-folding with respect to scale, complexity, and functionality. During our research we developed a new self-folding technique enabled by shape memory composites—a laminate

sheet consisting of one or more layers of shape memory polymer and one or more layers of a structural substrate. We explored variations of this composite at different sizes and with different stimuli for triggering the folding process. We identified features and abilities necessary for functional self-folding, and used these composites to produce them. We also investigated ways to embed mechanisms and sensors into these machines.

Chapter 2 explains our initial attempt to build a self-folding system. We outline the features we judged to be critical for creating self-folding machines. We developed our new self-folding technique, the shape memory composite, and used it to build a functional inchworm robot.

Chapter 3 explores the important properties of self-folding hinges. We identified torque, angular control, and minimum feature size as parameters that define the design space for self-folding. We developed analytical models that incorporate the thermodynamics and mechanical properties of these hinges in order to predict their performance, and validated these models with experimental data.

Chapter 4 presents our efforts to build a fully-autonomous self-folding machine. We set out to demonstrate that the self-folding process could produce machines with arbitrary structures and mechanisms, without human intervention or external equipment. We designed and built a self-folding crawling machine which demonstrated key features necessary for these capabilities.

Chapter 5 explores different techniques for embedding sensors in self-folding machines. We designed and built three sensors: a capacitive touch sensor, a bistable switching mechanism, and an electromagnetic velocity sensor. We also built a self-folding lamp to demonstrate the efficacy of these sensors in a functional machine.

Chapter 6 explores a new shape memory composite design that is capable of self-folding millimeter-scale features. This design incorporated new materials, new adhesives, and new machining methods. We demonstrated the composite is capable of self-folding hinges as small as 0.5 mm, and used it to build a self-folding model ship and a model bumblebee.

Chapter 7 details possible avenues for future research, including current limitations and likely avenues for overcoming them.

Everything is theoretically impossible, until it is done.

Robert A. Heinlein

2

Self-Folding a Machine

2.1 Introduction

In order to establish the feasibility of self-folding machines, we began by attempting to build one. This chapter outlines our efforts to build a self-folding inchworm robot that is capable of locomotion. Much of the content is previously published [65].

When we began our investigation into self-folding machines, the ability to fold functional, printable robots by hand had already been demonstrated [66]. These robots were folded from a single sheet of plastic, with a flexible circuit bonded to one side and electromechanical components installed before folding. The plastic sheet acted as both the rigid structure of the robot and the flexural joints. In order to create a similar, self-folded robot, we needed an actuation method for folding that suited the machine: It had to be inexpensive and fast to produce in low volume; it had to be able to produce durable structures in a typical indoors environment; it had to work at length scales of roughly 1 to

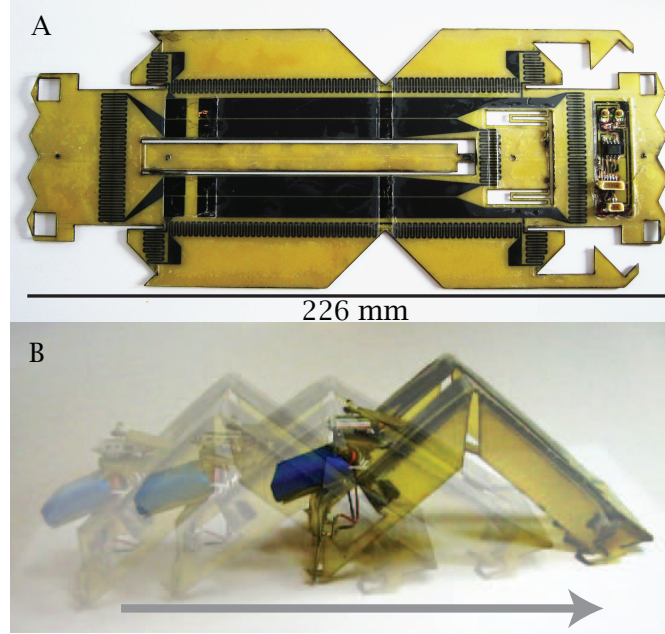


Figure 2.1: (A) The inchworm before it has folded into its functional shape. (B) The folded inchworm, after the servo and battery has been added. This robot weighs 29 g, and moves at a rate of 2 mm/s.

30 cm; it had to be capable of complex fold patterns and sequential folding for multiple fold steps; and it needed to be capable of flexural hinges for dynamic mechanisms.

Many self-folding methods have been invented and demonstrated, but most are not suitable for printable machines. Some can only form fragile structures in specific situations, such as aqueous environments [53]. Others can only produce a minimal amount of torque at their hinges and are only suited to sub-millimeter scale structures [54, 62, 67]. Others require expensive external devices for actuation, such as lasers [55] or magnetic field generators [58]. A few are functionally appropriate, but incompatible with printable manufacturing. Shape memory alloy hinges, for example, require discrete installation and individual programming, which increase cost and fabrication time [56].

One existing self-folding method, developed by Liu et al. [61], came close to our requirements by using shape memory polymers (SMPs). SMPs are polymers that transition from a glass to a rubber phase when heated above a certain temperature. During this transition, the material can undergo a shape memory effect; if the material is deformed in its rubber state and then cooled to its glass state, it will hold this new shape until it is reheated back to its rubber state, at which point it will return to its original geometry, effectively ‘remembering’ its original shape. This effect is often used to create contractile

sheets, such as shrink wrap or heat shrink tubing. In these applications, The SMP has three functional parameters: The transition temperature T_g at which the material changes shape, the shrink ratio S_R between its initial and contracted lengths, and the directions in which shrinking occurs.

In this case, the SMP was prestretched polystyrene (PS), which was programmed to shrink bidirectionally by 50% when heated. These PS sheets were induced to self-fold, first by printing black lines on them, and then shining a light on them. The black lines absorbed the energy from the light and selectively heated the sheet on one side only, which caused that side to contract and the sheet to bend. This technique was inexpensive, printable, and operated close to the length scales we were interested in. It did have two noticeable drawbacks, however. The first is that the polymer sheets were not suited for repeated bending, like we would need in a folded joint. The second is that the folding occurs simultaneously, when the light is turned on. This can make folding complex shapes more difficult, as some patterns must be folded sequentially.

In order for a self-folding method to be capable of producing a machine, we identified four principle capabilities that it must demonstrate: (I) sequential folding for multiple fold steps, (II) mountain (convex side up) and valley (convex side down) folds for complex shapes, (III) angle-controlled folds for precise geometries, and (IV) flexural hinges for dynamic mechanisms. We developed a novel technique for self-folding that combined SMPs with resistive circuits, a plastic substrate, and structural features to achieve these requirements. To demonstrate this technique, we designed and built an inchworm robot shown in Figure 2.1. This device was chosen because it embodies all of the challenges we wished to address: it requires a specific and functional structure and a dynamic motion to achieve locomotion, which together require all of our principle capabilities.

2.2 Design

2.2.1 Composite Design

Self-folding robots require one-time, rigid folds to create the structure of the robot and flexural hinges for movement. To build these features, we designed a new self-folding method that we call a shape memory composite (SMC). This composite comprises two outer layers of contractile SMP, a plastic substrate layer, and a flexible circuit board (Fig-

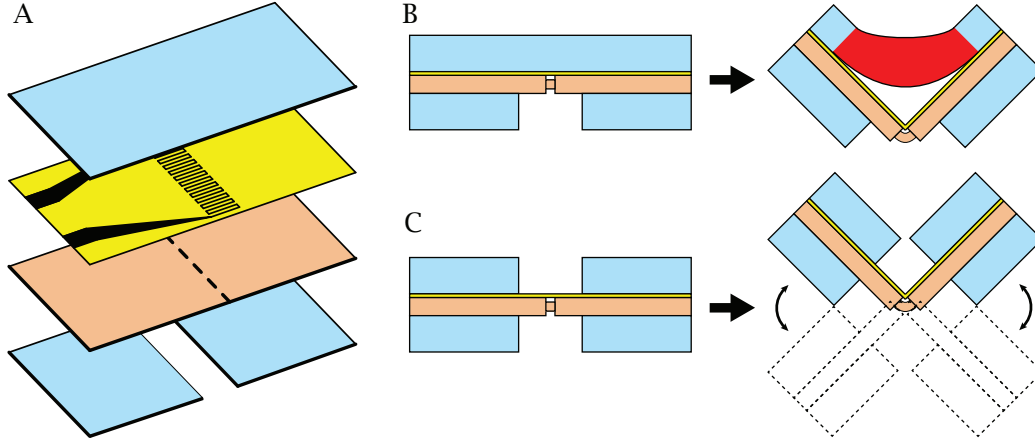


Figure 2.2: (A) The shape memory composite includes four layers: a flexible circuit (yellow), a plastic substrate (brown), and two layers of SMP (blue). The shape memory composite is capable of both one-time self-folding hinges and repeatable flexural hinges. (B) Self-folding hinges are built into the composite by removing a strip of SMP from the convex side. Folding occurs when the concave SMP contracts. (B) Dynamic hinges are created by weakening the substrate and removing the contractile layer from both sides.

ure 2.2A). Resistive heating elements are embedded along each self-folding hinge on the flexible circuit. To activate folding, the heating element is supplied with current, which causes the SMP to heat up and contract locally along the hinge. When the SMP on the concave side contracts, it pulls the faces on either side of the hinge together, causing the hinge to fold (Figure 2.2B). The plastic substrate is perforated along the hinge, increasing its flexibility and localizing the bending to a fold. A one-millimeter wide strip is removed from the convex SMP layer to bias the folding in one direction and prevent antagonistic contraction. Both mountain and valley folds can be made by cutting gaps into the SMP on either side of the composite. Flexural hinges are created by removing strips of the SMP layer from both sides, allowing the substrate to bend freely (Figure 2.2C). Because the SMP is only heated locally, individual hinges can be activated separately, allowing for sequential folding. The flexible circuit also contains the electronics to power and control the robot. In some hinges, additional SMP from the concave side was removed at the hinge ends where traces could not be fit to ensure that the unactivated SMP did not prevent folding.

Materials were chosen for their physical properties, cost, and ease of use. A 125 μm thick sheet of Polyetheretherketone (PEEK) is used as the passive substrate due to its high flexural strength (163 MPa [68]) and resistance to fatigue along folds. PS was chosen for the contractile layer due to its high S_R (2-to-1, or a contraction to 50% of its original length) when heated above its relatively low T_g (105 $^{\circ}\text{C}$). It is also one of the only commercially

available SMPs that was thick enough (250 μm) for our applications. Most SMPs are either too thin to produce enough contractile force (such as shrink wrap) or only shrink in one direction (such as heat shrink tubing). The flexible circuit board is made from a laminate consisting of an 18 μm copper layer and a 12 μm sheet of polyimide (CuPI). More details are in Appendix A.1.

2.2.2 Inchworm Design

An inchworm robot (Figure 2.1) was chosen to demonstrate our new self-folding technique because it required each of the four capabilities mentioned earlier. The body is composed of two halves connected by a dynamic hinge in the middle. A slider crank mechanism actuates the hinge, causing the inchworm to contract and extend. Locomotion is achieved by angling the ‘feet’ at the bottom of the front and back walls (Figure 2.3A-B) to create asymmetric friction so that they slide in one direction, and push the robot forward in the other. The front wall fold angle relative to the robot body is 45° and the back wall fold angle is 135° . Side walls (Figure 2.3C) are included at right angles to the robot body to improve structural rigidity. The servo is mounted on a platform that folds up 45° from the body (Figure 2.3D). The servo is driven by a 0.3 Hz triangle wave from a microcontroller

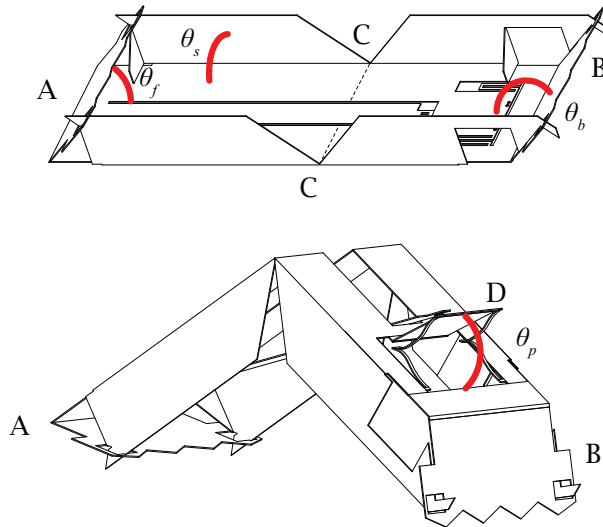


Figure 2.3: The inchworm robot consists of a front wall (A) and back wall (B) angled to create ‘feet’ with asymmetric friction. The front wall fold angle θ_f is 45° and the back wall fold angle θ_b is 135° . The robot also includes side walls (C) with fold angles θ_s of 90° , and a servo platform (D) with a fold angle θ_p of 45° . The top image represents the inchworm robot after the folding of its front, back, and side walls. The bottom image represents an upright and completely folded inchworm.

(ATtiny13, Atmel), and powered by a 7.4 V lithium polymer battery (EFLB1202S20, E-flite).

2.2.3 Angle Control

One challenge of self-folding is achieving precise folds without human observation and intervention. Effecting accurate and repeatable fold angles through hinge design alone would require precise fabrication and thermal control; instead we rely on mechanical stops to physically limit the fold angle. The side-walls fold first, and include triangular tabs at the far ends which fold simultaneously with the walls. The tabs act as mechanical stops for the side walls, producing a right angle (Figure 2.4A-B). Because of its geometry, this stop fold is tolerant of a large range of angles. Front and back walls fold next, aligning off of the side walls to achieve angles of 45° and 135° , respectively. Slots on the folding walls and tabs on the side walls aid in the alignment (Figure 2.4C-D). The servo platform includes the single valley fold in the structure. Its angle is controlled by serpentine tethers cut into the PEEK layer (Figure 2.4E-F). These tethers do not fully extend, but instead act like springs against the platform's hinge torque. The necessary length for constricting the platform to 45° was found experimentally.

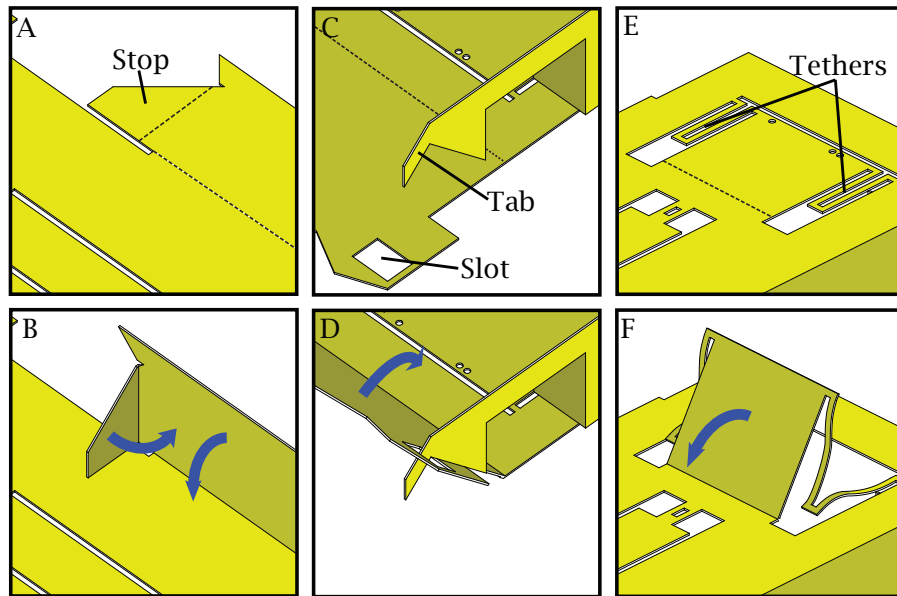


Figure 2.4: In order to limit fold angles, stops were included in the design. (A-B) Initial stops were designed to fold simultaneously with the side walls. These stops would create a 90° angle in the wall fold as long as the stop was not parallel with the side wall. (C-D) The front and back walls were designed to fold after the side walls. Slots were included in the front and back walls to align with tabs on the side walls. (E-F) The servo platform was limited by tethers cut in the PEEK layer. These tethers would not fully extend, but instead acted like springs that resist the actuated fold.

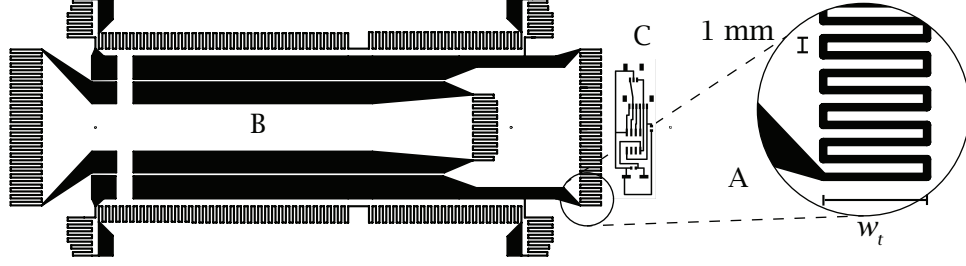


Figure 2.5: The CuPI layer includes two independent circuits: the fold-activating heating circuit, and the servo control circuit. (A) The bulk of the layer is a collection of resistive circuits patterned to maximize the current path in order to produce and distribute heat. The traces are 0.5 mm thick, with a peak-to-peak height w_t varying from 4.5 to 8 mm. (B) Portions of the activating circuit designed to carry current without producing heat were made as wide as possible to reduce resistance, preventing unintended heating. (C) The trace of the circuit used to drive the servo.

2.2.4 Circuit Design

In order to achieve local and sequential folding, we used joule heating from resistive traces embedded on a flexible circuit board to selectively activate the SMP. The heat generated by a resistor is equal to I^2R —where I is the current and R is the resistance—and R is inversely proportional to the trace cross-sectional area. In order to generate sufficient heat with a reasonable current, the traces were made 0.5 mm wide, the lower limit of our copper etching technique. A serpentine trace pattern was used that increased the resistance and distributed the heat over a larger area (Figure 2.5A). Both the peak-to-peak trace height and hinge length affected the temperature of the hinge. Therefore, for each hinge, the trace height was determined empirically to ensure sufficient folding without excessive warping or peeling. Along non-heating portions, the trace width was made as wide as possible (under geometric constraints) in order to minimize unwanted heating and deformation (Figure 2.5B). When possible, traces shared non-heating paths in order to simplify the circuit design. The flexible circuit also included a separate set of traces for connecting the discrete electronic components and controlling the servo (Figure 2.5C).

2.3 Fabrication

The robot was fabricated in five steps. The circuit design was printed directly onto the CuPI in wax using a solid ink printer (Colorqube, Xerox), and then etched in ferric chloride (CE-100, Transene) (Figure 2.6A) to produce the flexible circuit layer. Each layer (PEEK, CuPI, and two layers of PS) was cut with layer-specific features using a commercial CO₂

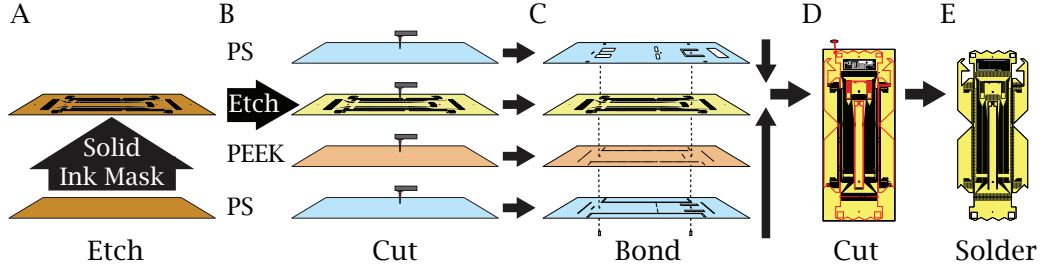


Figure 2.6: The 2D composite is fabricated in five steps. (A) The CuPI is masked and etched to produce the flexible circuit board. (B) Each of the four layers is machined with individual features defining the self-folding and flexural hinges. (C) The layers are pin-aligned and bonded with silicone tape. (D) The composite is cut into its final outline. (E) Electrical components are installed.

laser machining system (VLS2.3, Universal Laser Systems) that defined the flexural and self-folding hinges (Figure 2.6B). These layers were aligned with two pins and manually bonded with 50 μm silicone tape (Figure 2.6C). The composite was laser-cut again into the final shape to prevent misaligned edges (Figure 2.6D). Wires and electronic components were then soldered on (Figure 2.6E). The unfolded structure weighed 17 g.

2.4 Results

Self-folding occurred with minimal human intervention: The folding process was induced by supplying two amperes from an external supply for a fixed amount of time to each set of resistive traces in sequence; each mountain fold was activated for 60 s, and the valley fold was activated for 90 s (Figure 2.7). The robot was manually flipped before valley folding so that the hinge folded upwards and was not blocked by the table surface. Based on resistance measurements of the circuit, the folding process consumed ≈ 900 J.

After completion of the folding process and manual addition of a servo and battery, the inchworm robot weighed 29 g and measured 145 mm in its extended position. The robot was capable of moving on paper at a rate of 2 mm/s for a 0.3 Hz contraction frequency, or 0.8 body lengths per minute, and consumed 0.9 W during locomotion. Due to the complexity of asymmetric surface friction, this speed was irregular (Figure 2.8). The stroke length of the foot displacement measured 10 mm; therefore only 20% of the motion was converted into locomotion, and the rest was lost to slippage. The contraction frequency was chosen because higher frequencies resulted in even more slippage.

Effectiveness of the angle-control techniques was evaluated by measuring the final angle

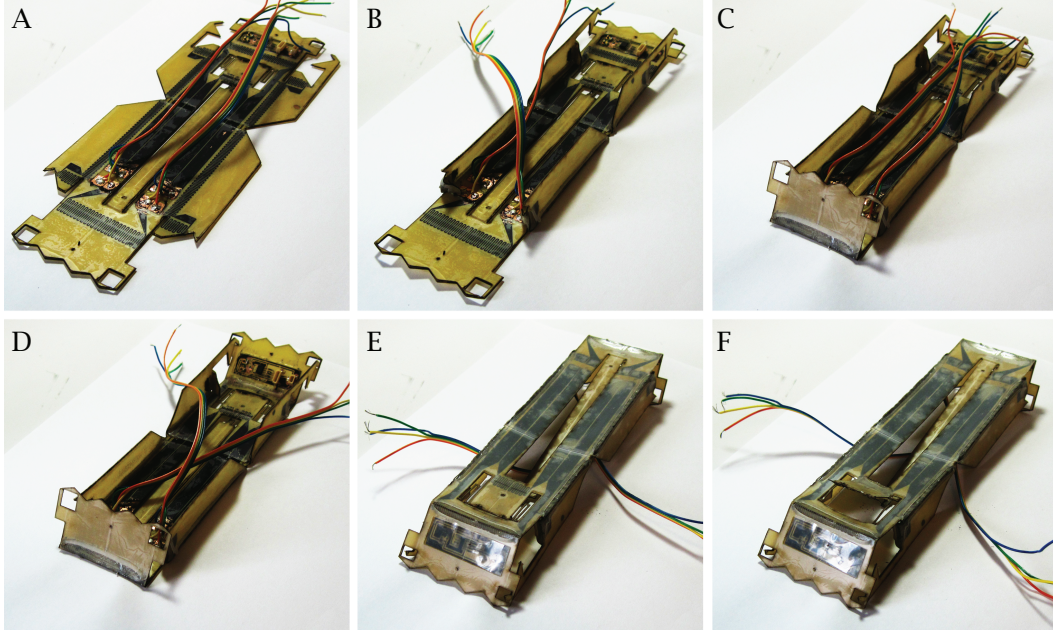


Figure 2.7: The robot folded in five sequential steps. Each set of resistive traces was supplied two amperes of current for 60 s, except for the servo platform, which took 90 s. (A) The initial 2D configuration. (B) The side walls folded first, and the left and right sides were folded in separate steps. (C) the front wall and (D) the back wall were folded next. (E) The inchworm is flipped over by hand, and (F) the servo platform folded.

of each fold (Figure 2.3); over the three robots tested, the twelve sidewalls exhibited an angle θ_s on their tabbed edge of $88^\circ \pm 4^\circ$ (standard deviation), compared to a planned angle of 90° ; these side walls also exhibited angle variance along the wall length; farther from the mechanical stop on the tabbed edge, the walls folded farther inward, so the entire wall is curved. Along all of the hinges the PEEK substrate exhibited deformations, likely due to melting or softening, which increased angle variance.

The front and back walls were more repeatable, likely due to stops at both ends. The back wall angle θ_b was $135^\circ \pm 1^\circ$ compared to a planned angle of 135° and the front wall angle θ_f was $60^\circ \pm 3^\circ$, even though the mechanical limit of the fold was 45° . This difference is likely due to an observed relaxation of the fold angle when the hinge cooled. The tethers were a less accurate control method; the angle of the servo platform θ_p was $52^\circ \pm 10^\circ$, compared to a planned angle of 45° .

2.5 Discussion

The self-folding technique used here demonstrated solutions to the four principle requirements for a self-folding robot. Sequential activation, mountain-valley folding, and the flex-

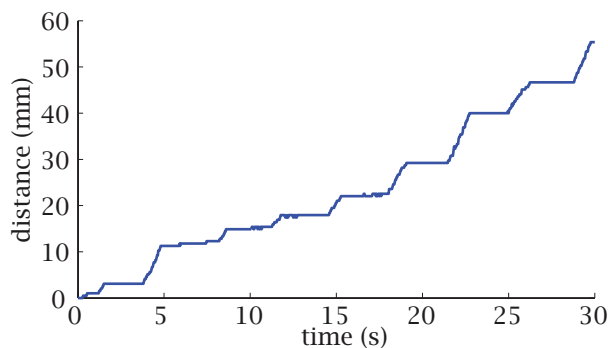


Figure 2.8: The displacement of the front edge of the inchworm robot over time. The flat regions represent times when the inchworm is contracting. The irregular size of the steps demonstrates the unpredictability of asymmetric surface friction as a driving force.

ural hinges all performed as expected. Mechanical stops proved adequate for approximate angle control, but not for high-precision fabrication. The slight curvature observed along nominally flat surfaces is also an obstacle to geometric precision, and different substrates may do a better job of maintaining their shape.

Greater precision could be achieved with feedback control; however, the sensors would need to be inexpensive and unobtrusive. An alternative way to increase precision would be to choose hinge parameters (such as trace size and material thickness) that would produce accurate fold angles without stops. Unfortunately, the variables affecting folding speed and angle are difficult to quantify. SMPs often exhibit viscoelastic behavior and the thermal dynamics in the hinge are complex and time-dependent. The substrate is also experiencing changes as it is heated, and the bonds between the three layers will often fail, further complicating an analytical model. However, even if the model couldn't predict an exact fold angle, it may be able to ensure that the hinge folded at a minimum to the mechanical stop. Such a model could be used to automate hinge design, and so would be a valuable tool for rapidly prototyping a wide range of machines.

The biggest obstacle towards achieving completely autonomous self-folding is insufficient hinge torque. The inchworm robot needed to be manually flipped because the actuated folds were not able to lift the body of the inchworm. Similarly, the servo and battery had to be attached after folding, because the hinges were incapable of lifting them. Once the hinges are capable of lifting the weight of the body, a self-folding robot could transform from a planar structure to a fully operational machine without human intervention.

Essentially, all models are wrong, but some are useful.

George E. P. Box

3

Models for Self-Folding Hinges

3.1 Introduction

With the inchworm in Chapter 2 we demonstrated a new self-folding method—the SMC. We also recognized that the scope of machines we could fold was limited by the SMC capabilities. One limitation was the machine size; our maximum machine size was limited by the torque the hinges could exert, and our minimum feature size was limited by mechanical stops and fabrication methods. We also recognized a limit to our machine complexity due to the ratio between our maximum machine size and minimum feature size. This ratio indicates the maximum number of features we could install. Finally, the precision of our folding technique limited the precision and functionality of our machines.

In this chapter we introduce three new SMCs: an electrically activated hinge that folds in one direction, an electrically activated hinge that folds in both directions, and a hinge activated by uniform heating, such as on a hot plate or in an oven. We characterize these

composites with a combination of analytical and numerical models in order to predict the folding torque, the precision of the final fold angle, and the thermal and mechanical physics which influence these behaviors. We designed and built test hinges and measured their temperature, torque, and displacement while varying hinge characteristics such as the SMP thickness, the resistive trace size, the supplied current, and the hinge geometry. After using the experiments to validate our models, we developed design rules to relate key design parameters to hinge performance. Much of the content in this chapter is previously published [64, 69, 70], but some of the models have been modified to reflect our improved understanding of these systems.

3.2 Unidirectional Electrical Folding

3.2.1 Design and Fabrication

The first composite we developed consists of three layers: an SMP layer on top, a paper substrate layer on bottom, and a flexural layer between the two that also serves as a flexible circuit board (Figure 3.1A). The substrate is weakened along the hinges by scoring the substrate along a line (Figure 3.1B-C). Resistive circuits at each hinge are included on the flexible circuit board to induce localized SMP contraction via joule heating. This layer is flexible, and has minimal impact on the mechanics of the composite. Folds can be activated

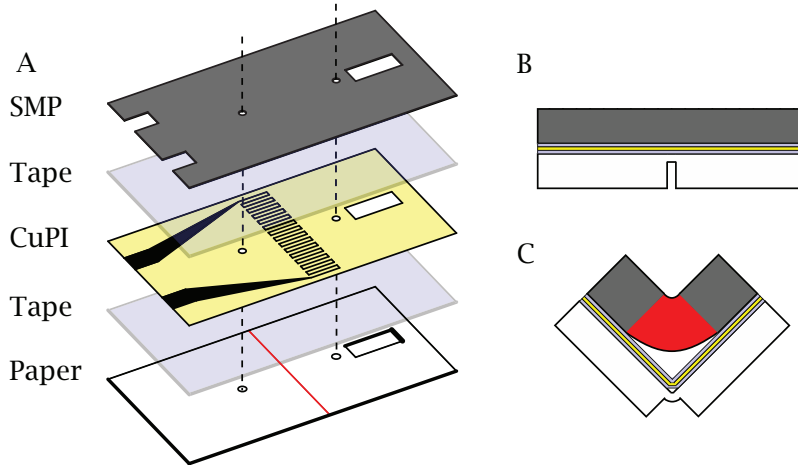


Figure 3.1: (A) The unidirectional SMC is assembled from three functional layers: The contractile SMP, the paper substrate, and the flexible circuit (CuPI). The layers are bonded together with silicone tape. The flexible circuit is embedded with a resistive copper trace arranged in a serpentine pattern to maximize heat generation. The paper is scored along the hinge with a partial-depth cut (red line). (B-C) Upon activation, the SMP contracts, causing the composite to bend at the hinge.

simultaneously or sequentially by supplying current to the appropriate circuit.

The substrate in the new composite is 510 μm thick paper; it does not melt or warp under the relatively high temperatures at which the hinges operate ($\approx 150^\circ\text{C}$), and it is stiffer than plastic relative to its weight. For the SMP we used polyolefin (PO) that shrinks uniaxially by 50% when heated above its transition temperature $T_g = 95^\circ\text{C}$. PO was chosen for the following experiments because it is commercially available in a variety of thicknesses, allowing us to observe the effect of this variation on hinge behavior. The PO was extracted from heat shrink tubing, and we used a variety of thicknesses ranging from 410 to 690 μm . The resistive circuit was made from CuPI. The resistive traces were 0.5 mm wide, and arranged in a serpentine pattern with a peak-to-peak height w_t .

The composite was assembled by laser-cutting each layer separately using a commercial CO_2 laser machining system (VLS 2.3, Universal Laser Systems), aligning them with pins, and bonding them together with 50 μm silicone tape. The copper circuit was etched with ferric chloride (CE-100, Transene) and masked by a solid ink printer (Colorcube, Xerox). Material details are available in Appendix A.3.

3.2.2 Model Design

In order to predict the hinge torque, we consider our hinge as two separate systems: the thermal system determines whether the SMP is in a glass or a rubber state, and therefore how much of the material is under stress, and the mechanical model correlates this stress to torque around the hinge. We model our hinge statically, assuming it is held in the flat formation. We’ve observed that, as a hinge folds, the torque due to SMP contraction increases while the torque due to gravity decreases. Therefore, if the hinge exerts enough torque that it begins to fold, it will generally continue to fold to completion (Appendix C.3). Because of this, the hinge torque in the flat state is the limiting factor in determining whether or not a hinge will fold, and we use this configuration as a ‘worst-case’ scenario for our models.

3.2.3 Thermal Behavior

Model

Developing a transient thermal model of the resistively heated hinge presents many challenges. It is a three-dimensional system in which thermal diffusion, convection, and re-

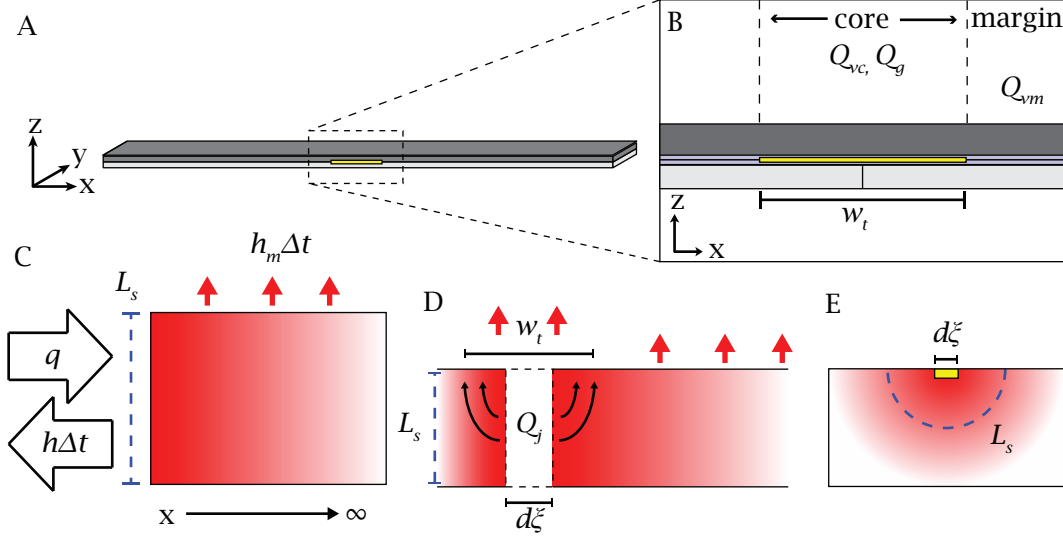


Figure 3.2: (A) The thermal model predicts the temperature of the composite in a flat state. (B) The hinge is divided into two regions: the core represents the region of width w_t embedded with the heating circuit, undergoing heat generation Q_g and convection Q_{vc} ; the margin is the rest of the hinge, heated by diffusion from the core and cooled by a lesser convection Q_{vm} . (C) This system can be modeled as a semi-infinite 1D system with constant heat flux q and convection h along a boundary surface of length L_c (blue), and additional convection h_m along its length. (D) The heat generated from a particular slice of the core with length $d\xi$ is Q_j , a fraction of Q_g . In our translation from 2D to 1D, we calculate the specific heat transfer coefficient h by relating it to the surface convection h_c along the trace width w_t . (E) To account for conduction into the table surface, we define L_c to include an additional thickness which accounts for heat flux into the table. This extra thickness can be thought of as a semicircle around the point source.

sistive heating are all significant factors. In order to develop a single governing model, we make three simplifying assumptions. For the following equations, we define all temperatures T_i as the difference between the absolute temperature and the environmental temperature in Kelvin, so that the environmental temperature $T_\infty = 0$.

First, we treat the SMP layer as a 1D system (Figure 3.2A). The geometry of the hinge is effectively constant in the y -direction, so we assume that the hinge is isothermal in that direction. Experimentally we observed that there were variations in the temperature at the edges of the material, but these regions are relatively small and difficult to model (Appendix B.3). In the z -direction (vertical), we find that the difference between the inner temperature of the SMP T and the surface temperature T_s is relatively small compared to the difference between T_s and T_∞ . This small temperature difference is represented by the ratio $C_s = T_s/T$. For all of our experimental hinges, $C_s > 0.9$. Therefore, for the sake of simplification, we assume the material is isothermal in the z -direction. We use C_s when comparing our model to experimental thermal data because the SMP temperature is measured at the surface using thermal imaging. Because of these assumptions, we only

consider thermal diffusion in the x-dimension.

Our second assumption is that the composite is divided into two adjacent but distinct regions: the core consists of all material directly above and below the electrical trace, and the margin is all material outside of the core (Figure 3.2B). The core is undergoing both a convective heat flux Q_{vc} with a transfer coefficient h_c from the center of the hinge into the air, and a constant heat flux Q_g generated by the resistive heater. Thermal energy is diffusing from the core to the marginal area, which is experiencing a lesser convection Q_{vm} with a corresponding coefficient h_m . The difference in convection is due to the significantly higher temperature at the core, which results in a higher convection coefficient (Appendix B.2).

The thermodynamics of a 1D system undergoing diffusion and dissipation can be expressed by the partial differential equation (PDE) (3.1) as a function of time t and distance from the hinge x . α represents the thermal diffusivity and β is the dissipation factor along the marginal region (Appendix B.7).

$$\frac{\partial T}{\partial t} = \alpha \frac{\partial^2 T}{\partial x^2} - \beta T \quad (3.1)$$

Because this equation is linear, we can find the answer by considering the solution T_n due to the heat flux Q_j out of a single point along the resistive trace with infinitesimal width $d\xi$. We then integrate this solution along the width of the trace w_t , effectively summing each individual thermal profile to provide us with the complete solution (Appendix B.1).

$$Q_j = \frac{Q_g}{w_t} d\xi \quad (3.2)$$

$$T(x, t) = \int_{x-w_t/2}^{x+w_t/2} T_n(\xi, t) d\xi \quad (3.3)$$

Because the 1D system with a point heat source is symmetric around the source, it can be modeled as a semi-infinite region with heat flux occurring along the boundary surface (Figure 3.2C). This surface is orthogonal to the direction of diffusion and has a characteristic length L_c , which is equivalent to the thickness of the composite t_c multiplied by 2, to account for the fact that the heat flux is occurring in both directions along the hinge. The surface is undergoing a constant heat flux q and convection with a transfer coefficient h . The rest of the region is undergoing dissipation due to convection with a transfer coefficient h_m . The solution T_n to this system is governed by the PDE and the

following boundary conditions:

$$T_n(x, 0) = 0 \quad (3.4)$$

$$-k \left. \frac{\partial T_n(x, t)}{\partial x} \right|_{x=0} = q - hT_n(0, t) \quad (3.5)$$

These boundary conditions define that T_n begins at $T_\infty = 0$ for all points x , and that the conduction at the point source $x = 0$ is equal to the heat generation q due to the resistive heater reduced by the convection hT_n at that point.

In the physical system, convection is not actually acting on the orthogonal plane; Instead it is occurring along the length of the trace w_t (Figure 3.2D). Therefore, h can be approximated as a function of w_t , h_c , and L_c . We validated this approximation by comparing analytical and numerical solutions for the hinges in Appendix B.6.

This equation is not explicitly solvable with the given boundary conditions. Instead, we can consider the solution in two different regimes. When $T = 0$, the dissipation term βT is negligible. In this situation, the problem is similar to the transient, semi-infinite system with surface convection, and we can find an explicit solution that fits the PDE and the boundary conditions of our ideal 1D system [71].

$$\frac{\partial T_i}{\partial t} = \alpha \frac{\partial^2 T_i}{\partial x^2} \quad (3.6)$$

$$T_i(x, t) = \frac{q}{h} \left[\operatorname{erfc} \left(\frac{x}{\sqrt{4\alpha t}} \right) - \exp \left(\frac{hx}{k} + \frac{h^2 \alpha t}{k^2} \right) \operatorname{erfc} \left(\frac{x}{\sqrt{4\alpha t}} + \frac{h\sqrt{\alpha t}}{k} \right) \right] \quad (3.7)$$

erfc is the complementary error function and k is the thermal conductivity. Definitions for k and α in terms of material properties and composite geometry can be found in Appendix B.4.

As the solution approaches a steady state, the time derivative term becomes negligible and the PDE can be approximated as the following:

$$\alpha \frac{\partial^2 T_o}{\partial x^2} = \beta T_o \quad (3.8)$$

$$T_o(x) = \left(\frac{q}{h + k\sqrt{\frac{\beta}{\alpha}}} \right) \exp \left(-\sqrt{\frac{\beta}{\alpha}} x \right) \quad (3.9)$$

We can then combine these two solutions using a sigmoidal equation F_s that smooths the transition between these two regimes across a range centered around time t_r (Ap-

pendix B.8).

$$t_r = \log \left(\frac{k\sqrt{\frac{\beta}{\alpha}}}{h + k\sqrt{\frac{\beta}{\alpha}}} \right) \frac{k^2}{\alpha h^2} \quad (3.10)$$

$$F_s = \frac{1}{1 + \exp(5(1 - t/t_r))} \quad (3.11)$$

$$T(x, t) = T_i(x, t) + F_s(T_o(x) - T_i(x, t)) \quad (3.12)$$

Our use of a 1D model assumes that the composite is insulated from the surface it is resting on. In practice, when the composite is resting on a material (such as plastic or particleboard) with a thermal conductivity of 0.05 W/(m K) or greater, a substantial amount of heat will conduct through that material, resulting in 2D diffusion. We cannot solve for the 2D system with the given boundary conditions, so instead we adapt the 1D solution by incorporating the table surface into the model as an additional composite layer. The thickness t_v of this virtual layer can be thought of as a semicircle around the hinge, so that our analytical model effectively sweeps the 1D solution in a radial pattern around the heat source (Figure 3.2E). As the temperature diffuses outward, t_v increases, and we approximate this with Equation (3.13) (Appendix B.10).

$$t_v = (12 \text{ mm}) \left[1 - \exp \left(-0.025 \sqrt{t/(1 \text{ s})} \right) \right] \quad (3.13)$$

The primary effect of t_v is reducing q and h through t_c and L_c . t_c is the sum of the thicknesses of the n layers, including the paper thickness t_p , the SMP thickness t_s , the adhesive thickness t_d , and t_v .

$$L_c = 2t_c = 2 \sum_{i=0}^n t_i = 2(t_s + t_p + 2t_d + t_v) \quad (3.14)$$

$$q = \frac{Q_j}{L_c L_h} = \frac{I^2 R_0}{w_t L_c L_h} \quad (3.15)$$

In our physical system, the increasing hinge temperature is increasing the resistance of the circuit, which increases the power generated. Fortunately, this effect can be lumped in with the convection term in the model. The derivation and validation of this term can be found in Appendix B.5, and the complete term can be found in Equation (3.16).

$$h = \frac{h_c L_h w_t - I^2 R_0 \alpha_{tc}}{L_c L_h} \quad (3.16)$$

We built a two-dimensional finite element analysis (FEA) model in COMSOL to help validate our experimental results. The FEA allowed us to confirm our geometric assumptions and physical parameters, and test a larger range of variables.

Experimental Methods

To validate our thermal model, we built and activated experimental structures consisting of two faces connected by a single hinge and measured the temperature of their SMP layer. Test hinges for all experiments were 30 mm wide. One face was 30 mm long with copper pads at the bottom edge for connection to a power supply. The other face was 27 mm long, with a slot near the far edge designed to fit a weighted hook for torque testing in later experiments (Section 3.2.4).

When measuring the temperature of the hinge, both faces of the test hinge were secured to a horizontal piece of acrylic to maintain a flat state. A set amount of current was supplied to the resistive circuit, and the SMP surface temperature was measured with a thermal camera (T440, FLIR) at a rate of two hertz for five minutes. The core temperature was determined by averaging the surface temperature over the length above the trace, and the marginal temperature was determined from the temperature profile along the midline of the SMP, perpendicular to the hinge (Figure 3.3). Five samples were used for

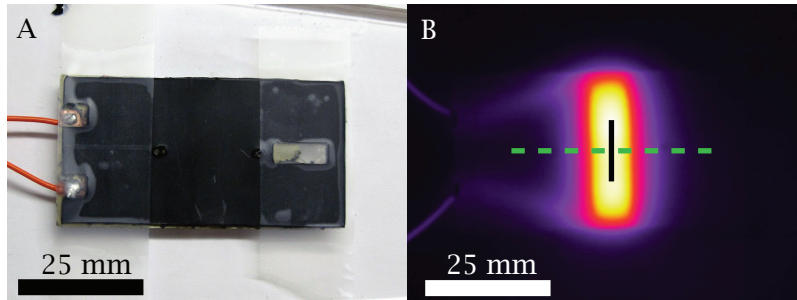


Figure 3.3: The experimental setup used to measure the hinge SMP temperature, viewed in the visual spectrum (A), as well as through a thermal camera (B). The core temperature was determined by averaging the temperature of each pixel along the solid black line. The marginal temperature was determined by measuring the temperature profile along the dashed green line.

each experiment.

Results

We first observed the effects of SMP thickness on the temperature profile. We measured the core temperature as a function of time for hinges with an SMP thickness of 410 μm and 690 μm , and found that the standard deviation of the measurements were larger than the mean difference between the two sets of hinges. The model predicts that T_s of the hinge with 690 μm SMP will always be 9% less than that of the hinge with 410 μm SMP. Measured temperatures supported this calculation; after the first minute of activation, the measured T_s of the 690 μm SMP remained within 10% of the temperature of the 410 μm SMP. The predicted difference in T_s between the two thicknesses is derived mostly from the difference in C_s between the models; the model predicts almost identical inner temperatures for the two hinge designs.

We then observed the effect of time and current on the temperature. We measured the core temperature $T(0, t)$ of hinges with 690 μm thick SMP layers, when their heating circuits were supplied with either 2 A or 1.75 A (Figure 3.5A). The data indicates that our model is effectively capturing the relationship between temperature and time. We measured the temperature profile $T(x, t)$ of the SMP as a function of distance from the hinge line (Figure 3.5) at $t = 150$ s and $t = 300$ s. In the margin, the models and experimental data all

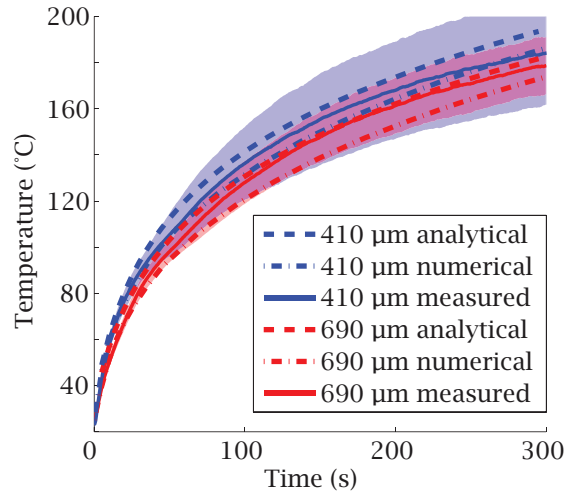


Figure 3.4: Hinges with SMP thicknesses of 690 μm and 410 μm were supplied with two amperes for five minutes. The measured, analytically modeled, and FEA modeled temperatures at the center of the hinge are plotted as a function of time. The shaded region indicates standard deviation, $N=5$.

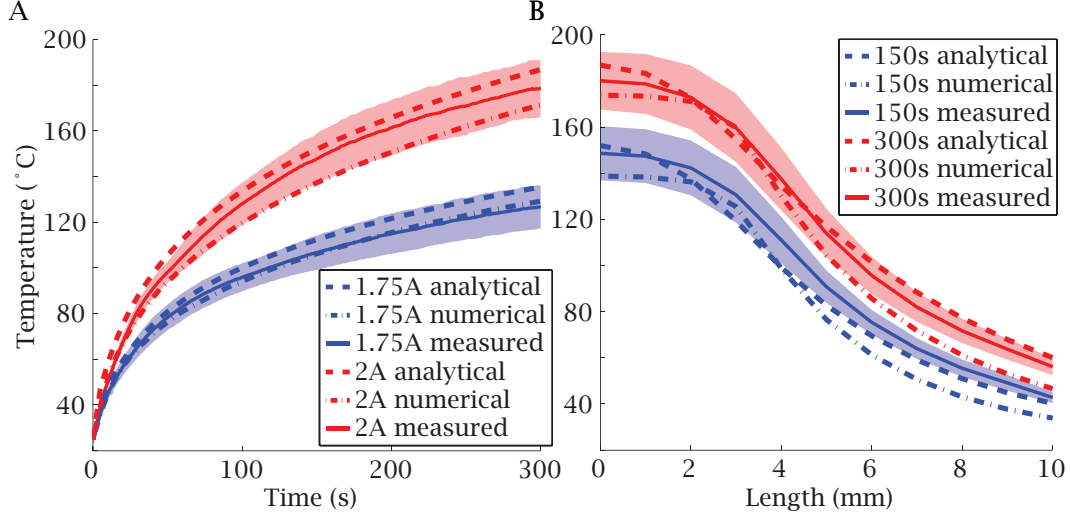


Figure 3.5: (A) Hinges were supplied with either 2 A or 1.75 A for five minutes. The measured, analytically modeled, and FEA modeled temperatures at the center of the hinge are plotted as a function of time. (B) The thermal profile of these hinges was measured at 150 s and 300 s. The measured, analytically modeled, and FEA modeled temperatures are plotted as a function of distance from the hinge. In both plots, the shaded region indicates standard deviation, N=5.

show that temperature decreases with distance from the hinge.

3.2.4 Torque Behavior

Model

The temperature profile of the SMP is used to predict the torque of the hinge through a mechanical model with two components. First, we use the temperature model to calculate the strain and stress in the SMP. As the SMP temperature increases, the material transforms from a glass to a rubber state as a function of temperature, changing its material properties and its resting length (Figure 3.6A). Second, we use the SMP stress to calculate the torque exerted on the folding face by the SMP, based on the hinge geometry.

At room temperature, the SMP stress σ and strain ϵ are uniformly zero. However, as the material temperature exceeds the transition temperature and the SMP is held in place (Section 3.2.2), a strain is induced by the shape memory effect. For the PO with a shrink ratio of 2-to-1, the contractile strain is one. We use the estimate from Tobushi et al. [72] that the material transition occurs linearly over a temperature range $2T_r$ so that:

$$\epsilon = \frac{T(0, t) - T_g + T_r}{2T_r} \quad T_g - T_r < T(0, t) < T_g + T_r \quad (3.17)$$

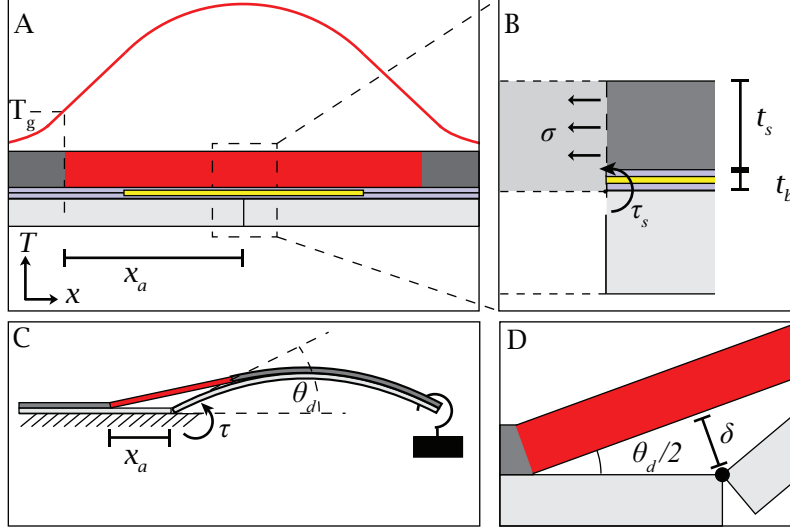


Figure 3.6: (A) The mechanical model uses the thermal model (red line) to determine the width x_a of the SMP that is under contractile stress. (B) In a static state, the torque τ_s can be determined by the contractile stress σ , the SMP thickness t_s , and the lever arm t_b . (C-D) Under large loads the SMP will delaminate and the face will bend, resulting in a small deformation angle θ_d and increasing the lever arm by a distance δ .

The strain corresponds with a stress. For this hinge we model the PO as elastic up to $\epsilon = 1$ based on experimental data (Appendix C.2.1). We assume that the SMP is under plane strain because it is constrained in the y-direction by the substrate. Therefore:

$$\sigma = \frac{E\epsilon}{1 - \nu^2} = \begin{cases} 0 & T(0, t) < T_g - T_r \\ \frac{4E}{3} \left(\frac{T(0, t) - T_g + T_r}{2T_r} \right) & T_g - T_r < T(0, t) < T_g + T_r \\ \frac{4E}{3} & T(0, t) > T_g + T_r \end{cases} \quad (3.18)$$

where the Poisson's ratio $\nu = 0.5$. The Young's modulus E varies along with the phase transition, and is roughly an order of magnitude greater when the SMP is in a glass phase. However, the glass portion of the SMP is at rest when held in place, so only E of the rubber phase is considered in our model.

This stress produces a torque τ_s around the pivot point of the hinge (Figure 3.6B). This pivot point is assumed to be at the interface between the substrate and the adhesive. The steady state torque is determined by integrating the stress σ through the thickness of the

SMP.

$$\begin{aligned}\tau_s &= \int_{t_b}^{t_s+t_b} \sigma x L_h dx \\ &= \frac{(t_s^2 + 2t_b t_s) \sigma L_h}{2}\end{aligned}\tag{3.19}$$

where t_b is the combined thickness of the copper-polyimide and the silicone tape.

This model is sufficient if the composite is effectively rigid and static. However, we observed that there is additional torque resulting from deformation of the hinge (Figure 3.6C). Specifically, in our experimental setup there is a point load at the end of one hinge face that balances the hinge torque in order to measure the blocked torque. This point load causes the hinge face to bend, resulting in a small displacement angle θ_d . Any non-zero angle will increase the torque by increasing the lever-arm. The deformation raises the SMP layer away from the pivot by a length δ , which can be included in our model, resulting in a modified torque equation.

$$\begin{aligned}\tau &= \int_{t_b+\delta}^{t_s+t_b+\delta} \sigma x L_h dx \\ &= \frac{(t_s^2 + 2(t_b + \delta) t_s) \sigma L_h}{2} \\ &= \tau_s + \delta t_s \sigma L_h = \tau_s + \tau_d\end{aligned}\tag{3.20}$$

We can separate this additional torque as a new term τ_d , representing the additional deformation torque. In order to solve for δ , we must first determine θ_d , which is dependent on the stiffness k_b of the folding face and its radius of curvature ρ .

$$\rho = \frac{k_b}{\tau}\tag{3.21}$$

$$2\theta_d \rho = L_f\tag{3.22}$$

$$\theta_d = \frac{L_f \tau}{2k_b}\tag{3.23}$$

δ can be deduced from the geometry of the hinge (Figure 3.6D).

$$\begin{aligned}\delta &= x_a \sin(\theta_d/2) \approx x_a \theta_d/2 \\ &= \frac{x_a L_f \tau}{4k_b}\end{aligned}\tag{3.24}$$

Equations (3.20) and (3.24) express τ_d as a function of τ . We can rearrange these equations in order to solve for an explicit solution to τ .

$$\tau = \tau_s + \frac{\tau x_a L_f t_s \sigma L_h}{4k_b} \quad (3.25)$$

$$\tau = \frac{\tau_s}{1 - \frac{x_a L_f t_s \sigma L_h}{4k_b}} \quad (3.26)$$

Experimental Methods

The sample hinges have the same design as in Section 3.2.3. The 30 mm face of each sample was secured with tape to a horizontal piece of acrylic, and the 27 mm face was blocked by a weight hooked through the slot. This weight rested on a scale (PL 303, Mettler Toledo). A fixed amount of current was supplied to the resistive circuit for five minutes. When folding was triggered, the sample exerted a force on the weight to balance the hinge torque. The torque was deduced from the change in weight registered by the scale, indicating the point load applied on the weight by the folding face. Data was collected with Matlab at approximately 8.3 Hz. Five samples were used for each experiment.

Results

We measured and compared the blocked torque exerted by hinges with a six millimeter wide trace and SMP thicknesses of 410 μm , 560 μm , and 690 μm when activated by two amperes and held in a flat configuration (Figure 3.7A). The torque exhibited two regimes. The first, characterized by a rapid increase in torque and lasting approximately 50 s, is governed by the rise in core temperature, until the material in the core has full transitioned. The second regime exhibits a steady or slowly increasing torque, governed by the deformation occurring in the hinge face. At 560 μm and 690 μm , the experiments match the model assumptions of slowly increasing deformation, resulting in both a larger initial torque during the first regime, and a slow increase in torque during the second. At 410 μm , the experiment does not exhibit any growth in the second regime, and instead resembles the model without deformation; it is possible that the torque exerted from the 410 μm SMP is not large enough to cause deformation.

The torque was also measured for hinges with a 560 μm SMP layer at 2 A with a three millimeter trace, and at 1.5 A with a six millimeter wide trace. When the trace width was

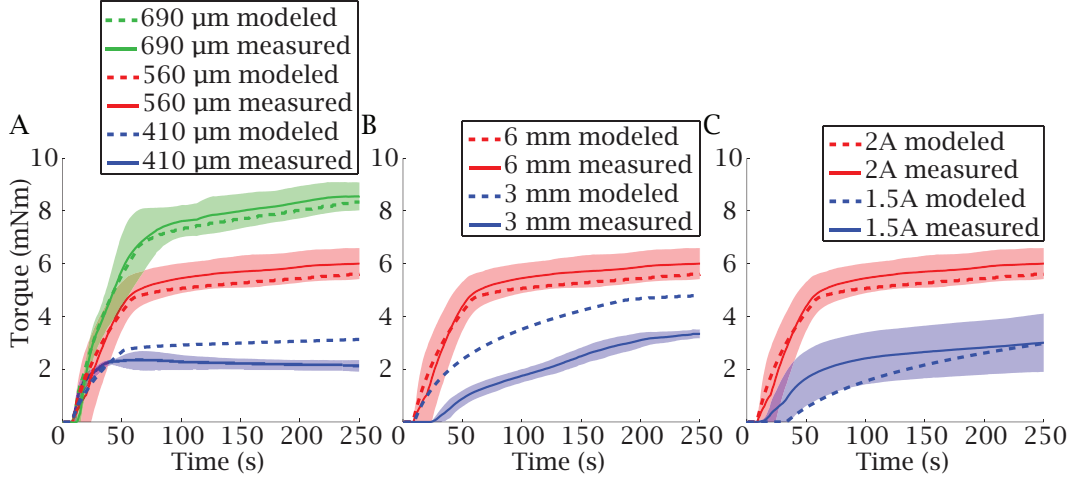


Figure 3.7: Experimental hinges were built and supplied with a fixed amount of current while their tip was blocked and the resulting torque was measured. This torque is plotted as function of time, along with the predicted torque from our analytical model. The shaded region indicates standard deviation, $N=5$. (A) Hinges with three different SMP thicknesses: 410 μm , 560 μm , and 690 μm . (B) Hinges with a 6 mm wide trace and a 3 mm wide trace. (C) Hinges supplied with 2 A and 1.5 A.

reduced to three millimeters, the model predicts a decrease in torque (Figure 3.7B), but the measured torque is still noticeably lower than what is predicted by the model. The trace width affects the torque by two means: a reduced trace produces less heat, slowing the SMP transition, and the small core leads to a smaller active width, reducing the deformation torque. It is also possible that the smaller width interferes with our assumption of a fixed strain. If the activated length is small, the unactivated SMP may deform enough to substantially reduce its length and strain.

In the case of a reduced current, the model and the experiments both indicate a lower torque that builds more slowly (Figure 3.7C). However, based on our measurements there appears to be significant variability. We predict that this current is heating the SMP into its transition range but not out of it, so small variations in temperature may have large effects on the SMP stress and hinge torque.

3.2.5 Free Displacement Behavior

Model

The geometry of the hinge during folding is inherently 2D, which makes quantitative analysis intractable. However, we can predict certain behaviors based on our qualitative understanding. First, if we consider a symmetric hinge that folds to completion, we can

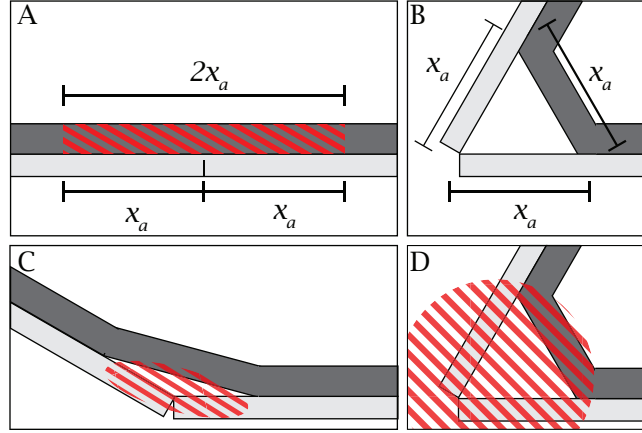


Figure 3.8: (A-B) When a hinge folds, the SMP and each face form a triangle, from which the maximum fold angle can be predicted. In the case of the PO with a 2-to-1 shrink ratio, this produces an equilateral triangle with an inner angle of 60° and a fold angle of 120° . (C) As the SMP folds, it separates from the substrate. If the thermal energy is not sufficient, the SMP will cease to be heated above the transition temperature, and not fold to completion. (D) If the heat is more than sufficient, the SMP will continue to transition to its rubber phase until it has completely contracted.

determine that there's a maximum fold angle based on the SMP shrink ratio. In the case of an SMP with a 2-to-1 shrink ratio, this maximum angle is 120° (Figure 3.8A-B). In general, for a n -to-1 shrink ratio, we expect a maximum fold angle of $2 \arccos\left(\frac{1}{n}\right)$.

From observation, we also know that under certain situations, namely when the thermal energy output is reduced, the hinge does not fold to completion. This can be explained by the idea that, as the hinge folds, the SMP lifts away from the heating element. As the distance between the two increases, the temperature of the SMP decreases and eventually falls below the transition temperature, at which point the SMP stops contracting (Figure 3.8 C-D). Alternatively, it may be that the SMP temperature is settling at a temperature near the transition temperature, resulting in an SMP layer that is partially rubber and partially glass, and therefore exhibits partial strain recovery.

Experimental Methods

The sample hinges had the same design as in Section 3.2.3. The 30 mm face of the hinge was secured to a horizontal piece of acrylic, and a fixed amount of current was supplied to the resistive circuit for five minutes. The 27 mm face was allowed to move freely. The process was recorded using a camera (Powershot A1100 IS, Canon), and the angle between the moving face and the horizontal surface was determined via image processing at half-second intervals. Three samples were used for each experiment.

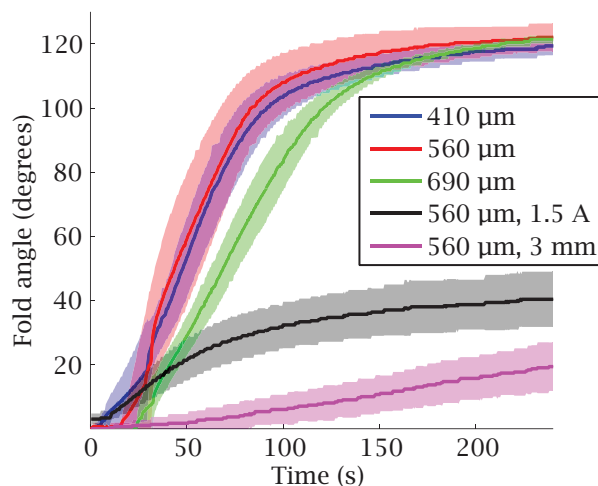


Figure 3.9: Experimental hinges were supplied with current and allowed to fold freely. Angular displacement is plotted as function of time. The shaded region indicates standard deviation, $N=3$. Designs include hinges with three different SMP thicknesses: $410\text{ }\mu\text{m}$, $560\text{ }\mu\text{m}$, and $690\text{ }\mu\text{m}$. Each hinge contained a 6 mm wide trace and was supplied with 2 A. In addition, hinges with $560\text{ }\mu\text{m}$ thick SMP were measured that included a 3 mm wide trace and supplied with 2 A, and contained a 6 mm wide trace and supplied with 1.5 A

Results

As can be seen in Figure 3.9 the SMP thickness does not have a significant effect on displacement. However, decreasing the current to 1.5 A or decreasing the trace width to three millimeters causes a significant decrease in displacement. One interesting behavior is that the hinges often bend slightly ($\approx 5^\circ$) in the opposite direction before folding. We believe this is due to expansion of the SMP as its temperature increases, but before it transitions into a rubber state.

3.2.6 Sample Structures

In order to demonstrate the functionality and versatility of these composites, we built two self-folding structures using PS as the SMP layer instead of PO. PS was only available in one thickness ($250\text{ }\mu\text{m}$) and so was not appropriate for the earlier characterization experiments. However, it shrinks bidirectionally, which is necessary for orthogonal hinges in a single composite. We constructed a self-folding pyramid, seen in Figure 3.10A-B, to demonstrate concurrent folding into a polyhedron. The four folds were simultaneously activated by linking the resistive circuits in series. We also built a self-locking slot-and-tab assembly, seen in Figure 3.10C-F. This mechanism first actuated the folds to fit the slot

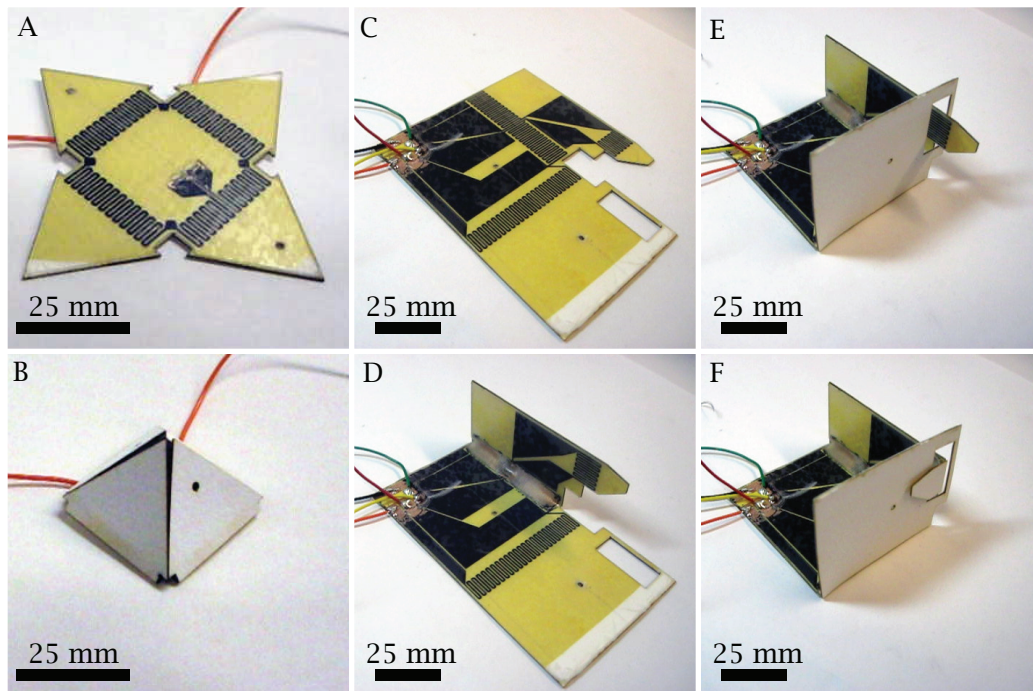


Figure 3.10: (A-B) A pyramid folded through simultaneous activation of four hinges. (C-F) A locking slot and tab assembly folded through sequential activation of three hinges.

into the tab, and then actuated another hinge within the tab to hold the slot in place. This mechanism demonstrates the efficacy and potential applications of sequential folding. In both structures, hinges were activated with two amperes for one to two minutes, so that all examples completed their self-folding in less than four minutes.

3.3 Bidirectional Electrical Folding

3.3.1 Design

The unidirectional composite is simple to make, but functional folding requires that we be able to fold in both directions. We designed a similar composite that is capable of bidirectional folding using five layers (Figure 3.11A). This composite is symmetric on either side and consists of a flexible circuit layer in the center sandwiched between two layers of a paper substrate, and two outer layers of SMP. We use the same paper substrate and CuPI flexible circuit as were used in the unidirectional hinges, and PS as the SMP layer.

Self-folding hinges are made by cutting slits into the paper and PS on the convex side of the fold, and a wider gap into the paper on the concave side. This allows the SMP on the

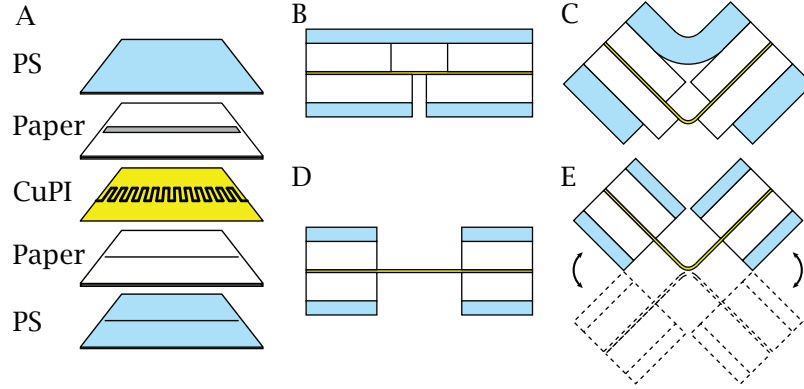


Figure 3.11: (A) The bidirectional composite consists of five layers: two outer layers of PS, two layers of paper, and a CuPI layer in the middle bearing a flexible circuit. (B) A structural hinge, designed to fold once when activated and then become static. A gap in the upper paper layer and slits in the bottom layers of paper and PS allow the hinge to bend. (C) When activated, the PS on the concave side pulls the two faces together, bending the CuPI along the hinge. (D-E) A dynamic hinge, designed to bend freely and repeatedly around the CuPI layer.

concave side to contract and the composite to bend at the circuit layer (Figure 3.11B-C). In this way, the CuPI doubles as the flexural layer for our hinges. Because this layer is much thinner than the rest of the composite, it substantially increases the flexibility of our hinges.

Flexural hinges are made by cutting gaps into both paper and SMP layers at the hinge so that the flexural layer can bend freely (Figure 3.11D-E). The range of bending is determined by the gap width, and dynamic hinges that bend in only one direction can be created by cutting a slit of negligible width on the convex side.

3.3.2 Thermal Behavior

Model

We adapted our previous model to predict the behavior of our new composite. In addition to changing the thermal properties to match the new composite, we also ran our experiments with the test hinges elevated so that both sides were exposed to air. This allowed us to disregard the assumptions regarding the table surface and virtual thickness t_v in accounting for conduction in the z-direction, and determine if the rest of our model was accurate. In this situation, L_c is equal to the composite thickness $t_c = 2t_s + 2t_p + 4t_d$. h_c and h_m are increased to account for convection on both sides of the composite (Appendix B.2).

Experimental Methods

To confirm our model, we measured the SMP temperature using similar methods as in Section 3.2.3. We built experimental laminate rectangles that were 40 mm wide and 60 mm long, with a 6 mm wide trace running parallel to the width of the rectangle. The trace was located 20 mm from one edge, similar to a self-folding hinge with a 20 mm face, but these rectangles did not have any of the mechanical features of a hinge in order to prevent folding during the experiments.

In order to remove the effect of conduction through the table surface, the test structures were suspended about the ground so that the resistive trace was approximately 20 mm from the edge of the supporting structure and exposed to the air on the top and bottom. Each trace was supplied with either 1.5 A or 2 A, and four samples were measured in each set.

Results

Figure 3.12A displays the measured temperature at the center of the heating element when supplied with a fixed amount of current (1.5 A or 2 A), as well as the predicted temperature from the analytical and FEA models. The models and the data both show the temperature asymptotically approaching a maximum temperature. It is interesting to note that the tem-

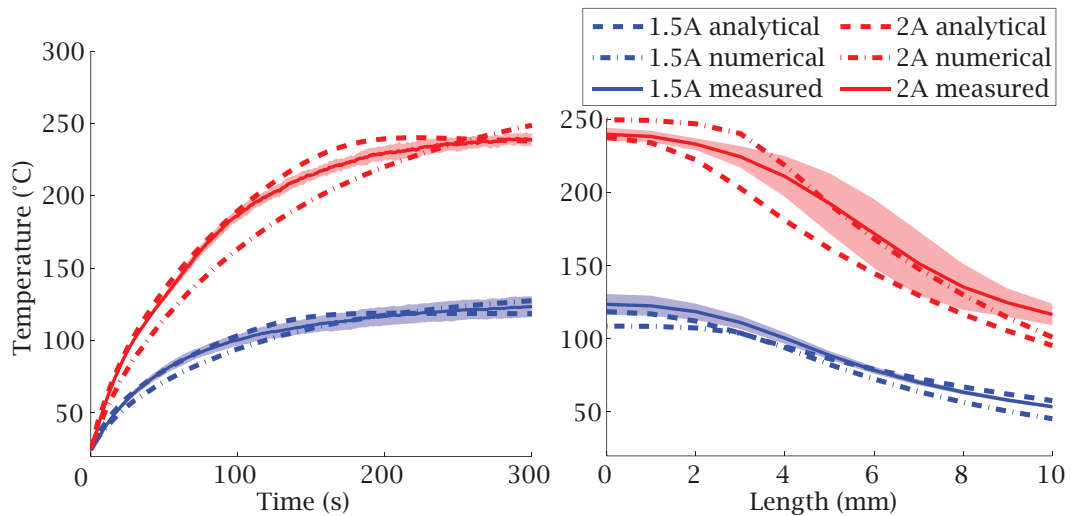


Figure 3.12: Test structures were supplied with either 1.5 A or 2 A for five minutes. (A) Measured, analytically modeled, and FEA modeled temperatures of the structure center are plotted as a function of time. (B) Measured, analytically modeled, and FEA modeled temperature profiles of the structures after 300 s are plotted as a function of the distance away from the hinge. In both plots, the shaded region indicates standard deviation, N=4.

perature in the FEA model increases more slowly than in the experimental results. This is likely due in part to our assumption in the model of a constant convection coefficient, when in fact this coefficient is dependent on temperature. Because of this, the numerical model overestimates the amount of heat lost to convection in the beginning of the simulation.

Figure 3.12B displays the temperature profile of the structure as a function of distance from the heating element after being supplied with a fixed amount of current (1.5 A or 2 A) for 300 s, along with the predicted temperature from the analytical and FEA models. The model and data both indicate the temperature decays as a function of distance.

3.3.3 Torque Behavior

Model

The mechanical model of the bidirectional composite is similar to that of the unidirectional composite, but there are two notable differences. First, the offset t_b between the SMP and the point of rotation is much larger because of the paper layer between the two. Second, the composite is significantly stiffer, so the deformation torque τ_d does not contribute to the predicted torque. We also observe experimentally that the PS does not act elastically at its contractile strain, so we instead measure the contractile stress σ directly during contraction (Appendix C.2.2), and use this value in our model as corresponding to maximum strain.

Experimental Methods

We built experimental hinges that were 40 mm wide, with one 40 mm long and one 20 mm long face. Each hinge had a 1 mm gap width. A hole was placed at the end of the 20 mm face and the 40 mm face was secured 20 mm from the edge, so that the hinge was suspended above the ground 20 mm from the supporting edge. These hinges were tested and analyzed according to methods similar to those in Section 3.2.4, with the mass hooked through the hole at the end of the 20 mm face. Hinges were supplied with 1.75 A so that the steady state temperature was above T_g but not enough to melt the PS.

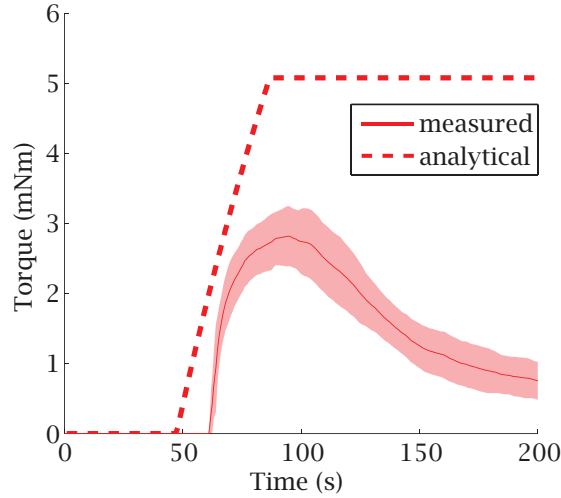


Figure 3.13: Experimental hinges were built and supplied with 1.75 A while their tip was blocked and the resulting torque was measured. This torque is plotted as function of time, along with the predicted torque from our analytical model. The shaded region indicates standard deviation, $N=4$.

Results

The measured torque is plotted as a function of time along with the model torque (Figure 3.13). The rise in measured torque occurs at approximately the same time as the model predicts, and they both reach half of their peak torque at 65 s. The measured torque then declines by approximately 75%. This is likely due to a combination of viscoelastic relaxation of the material and melting of the PS. Our model does not account for either of these effects, but this decay does not generally affect hinge performance because once the face begins to fold, the stress on the SMP will decrease, preventing this relaxation (Appendix C.3).

The peak measured torque (2.8 mNm) is also significantly less than the predicted torque (5.1 mNm). This may be related to our assumption that the temperature is constant in the y-direction when in reality this is not true (Appendix B.3). If the center activates before the edges, this region will also start relaxing before the edges reach peak stress, so that at any given point in time, only a partial width region of the hinge is under peak stress.

3.3.4 Maximum Feature Size

One important characteristic that is governed by the hinge torque is maximum face length. In a typical use case, the hinge must overcome the force of gravity to lift one or both of the folding faces, and this force increases as the size of the folding face increases. To

quantify this, we consider a rectangular face being folded from a flat state parallel to the ground. For this model, we assume that the mechanical behavior of the SMP is quasistatic, and that if the hinge begins to fold, it will continue to fold to completion (Appendix C.3). Therefore, the face length L_f is at its maximum L_{max} when the hinge torque τ_s is equal to the torque due to gravity τ_g in the flat state, for a given hinge length L_h and composite area density ρ_A . Relevant values can be found in Appendix C.1.1.

$$\tau_s = \frac{(2.8 \text{ mNm})}{(40 \text{ mm})} L_h \quad (3.27)$$

$$\tau_g = g \rho_A L_h L_f^2 / 2 = L_h (9.8 \text{ m/s}^2) (1.52 \text{ kg/m}^2) L_f^2 / 2 \quad (3.28)$$

$$\tau_s = \tau_g |_{L_f=L_{max}} \quad (3.29)$$

$$L_{max} = 97 \text{ mm} \quad (3.30)$$

Based on the peak measured hinge torque, we calculate that this composite can fold a rectangular face with a maximum length of 97 mm.

3.3.5 Minimum Feature Size

We observed that if a folding face became too small, the SMP would delaminate from the paper when activated, preventing folding. To quantify the minimum possible feature size that could be folded, an experimental structure was built consisting of a static base at-

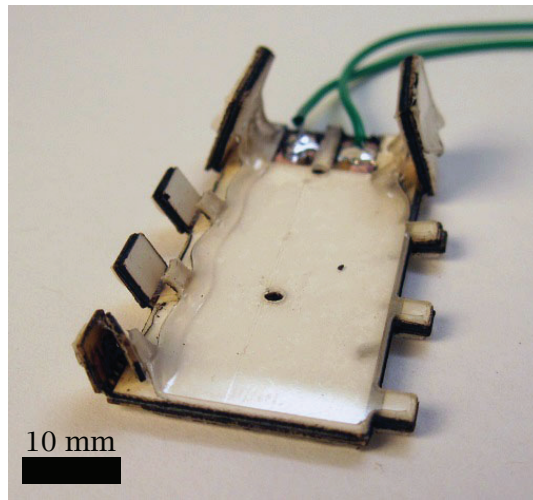


Figure 3.14: Square self-folding faces were built that were 10 mm, 5 mm, and 3 mm long to determine the minimum face size that could be folded. The 10 mm faces (background) folded successfully. The 3 mm faces (right) did not fold, while the 5 mm faces (left) folded and then delaminated.

tached to eight square folding faces: two 10 mm long faces, three 5 mm long faces, and three 3 mm long faces (Figure 3.14). This structure was supplied first with 2.25 A for one minute, and then 2.5 A for two minutes to stimulate folding. The 5 mm and 10 mm faces folded after 90 s, and the 5 mm faces subsequently delaminated between 135 s and 150 s. The 3 mm faces never folded, likely because the hinge was too short to produce enough thermal energy. These results indicate that the minimum face size is approximately 100 mm², although smaller faces may be possible if their temperature is closely controlled.

3.3.6 Angle Control

Model

In this composite the final fold angle θ of a hinge is dependent on the gap width w_g of the paper on the concave side. As the hinge folds, the paper on either side of the hinge eventually comes into contact, stopping the fold from progressing (Figure 3.15A). By varying w_g , we can control when this stop occurs. Based on the geometry of the hinge, including w_g and the paper thickness t_p , we can solve for θ using Equation (3.31).

$$\theta = 2 \arctan(w_g/2t_p) \quad (3.31)$$

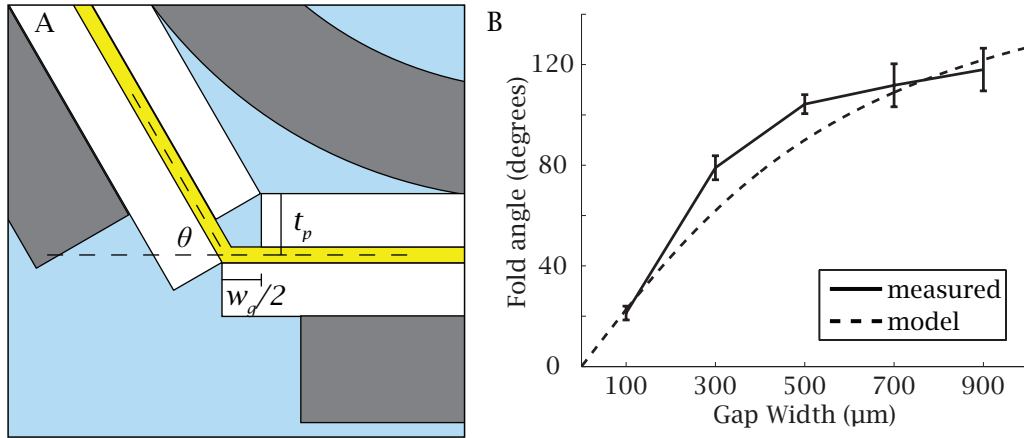


Figure 3.15: (A) A geometric model was developed to predict the final fold angle θ based on the paper thickness t_p and the gap width w_g . (B) The final fold angles of test hinges with gaps ranging from 100 to 900 μm were plotted as a function of gap width (solid line) along with the model predictions (dashed line). Error bars indicate standard deviation, $N=4$.

Results

To demonstrate this, we created test structures with self-folding faces that were 30 mm long and 30 mm wide. These hinges were tested while secured to the ground on one side. We supplied the resistive circuits with 2.5 A for two to three minutes, until self-folding was complete. We measured θ as a function of w_g , and compared this data to our model (Figure 3.15B). There is a positive correlation between w_g and θ but the measured angle is greater than the model predicts; we believe this is because the model assumes that the paper is incompressible, but in reality the corners deform under load. The maximum fold angle is limited by the shrink ratio of the PS layer, in this case limiting the angle to approximately 120° (Section 3.2.5).

3.4 Uniformly Activated Folding

3.4.1 Design

An alternative SMC design consists of two paper substrate layers and one SMP layer in the middle (Figure 3.16). It was designed to be activated in an oven or on a hot plate, and is capable of bidirectional folds. Hinges are programmed into the composite by cutting a line into the convex paper layer and a wider gap into the concave layer. Like the bidirectional electric hinges, the final fold angle can be programmed into the hinge by varying the gap width of the concave substrate. This composite is faster and less expensive to build because it uses fewer layers and no circuit layer. However, it must be activated uniformly, and so cannot fold in sequential steps. It also cannot be programmed with passive hinges because it does not contain a flexural layer.

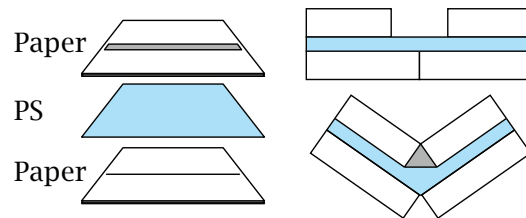


Figure 3.16: The uniformly heated composite consists of two layers of paper and one layer of polystyrene (PS) in the middle. Folding occurs when the PS contracts, and the fold angle is determined by the gap width cut into the paper on the concave side.

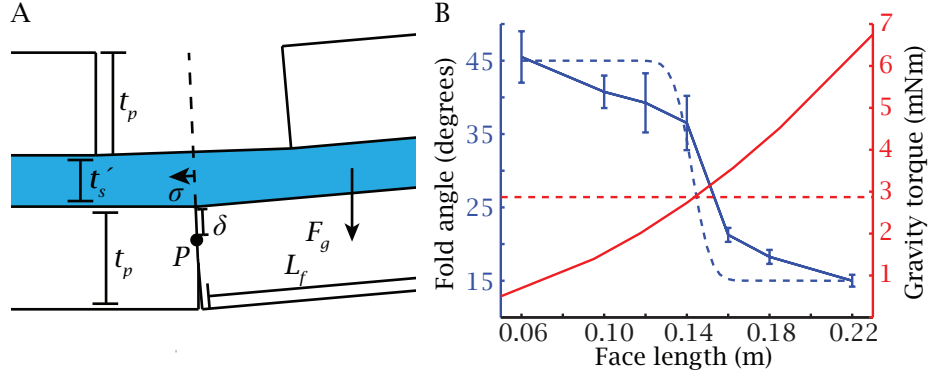


Figure 3.17: (A) The torque model for the uniformly heated self-folding hinges. In order to fold, the torque induced by the stress σ must overcome the torque from gravity. This balance is dependent on the thicknesses of the paper t_p and the SMP t'_s , the length L_f of the folding face, and the distance δ of the rotation point P from the bottom of the SMP. (B) The final fold angles of hinges are plotted in blue as a function of the folding face length. This is plotted over the moment on the face due to gravity (red), as well as the torque exerted by the hinge (red dashed line), and the predicted fold angles based on our model (blue dashed line). Error bars indicate standard deviation, $N=4$.

3.4.2 Maximum Feature Size

The torque model for this SMC is similar to previous models (Section 3.2.4). τ_s is dependent on the stress σ and thickness t'_s of the activated SMP, as well as the distance δ between the SMP and the point of rotation P , and the activated width L'_h of the SMP (Figure 3.17). In this case, δ is primarily caused by deformation of the paper as the substrate on either side of the hinge is compressed. We use $t'_s = 2t_s$ and $L'_h = L_h/2$ because we observed that under uniform heating conditions the composite was unable to constrain the SMP, so it would contract in the y-direction and expand in the z-direction.

$$\tau_s = \sigma L'_h t'_s (t'_s/2 + \delta) \quad (3.32)$$

The moment due to gravity is due to the length L_f of the folding face and the mass m of the composite.

$$\tau_g = g L_h \rho_A \frac{L_f^2}{2} \quad (3.33)$$

The maximum face length is assumed to be when these two torques balance out.

$$\tau_s = \tau_g|_{L=L_{max}} \quad (3.34)$$

$$L_{max} = \sqrt{\frac{\sigma t'_s (t'_s/2 + \delta)}{g\rho_A}} \quad (3.35)$$

We created test hinges that were 30 mm wide and had arbitrary lengths in order to characterize the folding torque of the self-folding composite. One side of these hinges was held flat in the oven, while the other was allowed to move freely during folding. The lengths of the moving faces varied from 60 to 220 mm. The final fold angle of these hinges is shown in Figure 3.17. This data is compared to the calculated moment exerted on these self-folding hinges due to gravity, as well as the calculated torque exerted by the hinges. We expected that the hinges with faces shorter than the maximum length would fold completely to a final angle of approximately 45°, while those with insufficient torque to overcome gravity would remain at 0°. Instead, as the face length exceeds the maximum length, the final angle gradually decreased. All of our samples showed minor angular deflections of at least 15°. We believe that this is due to the viscoelastic properties of the SMP. At the higher loads associated with face lengths near the maximum length, we'd expect to see relaxation of the SMP. It is also possible that some residual stress is exhibited as the material cools and hardens, resulting in partial folding regardless of face length.

3.4.3 Angle Control

The final fold angle θ is mechanically programmed into the composite by cutting the gap in the concave substrate at a particular width w_g . When the hinge folds to the desired angle, the two substrate layers on either face come into contact and physically stop the folding process. This control method is particularly important in this composite because it is uniformly heated and the folding process cannot be controlled through electricity. Equation (3.36) relates w_g to θ based on the geometry of the hinge.

$$\theta = 2 \arctan \left(\frac{w_g}{t_p + t'_s + \delta} \right) \quad (3.36)$$

The final fold angles for test hinges with gap widths ranging from 0.25 to 12 mm were measured and compared to our analytical model (Figure 3.18). In general the model

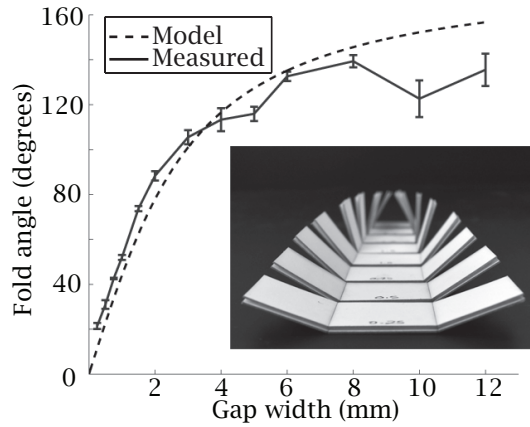


Figure 3.18: The measured angle of the uniformly heated hinges as a function of gap width (solid line), as well as the analytical model (dashed line). Error bars indicated standard deviation, $N=4$.

matches our experimental results, with standard deviations of 5° or less. However, as the w_g becomes larger than 8 mm, the hinges start becoming less precise and less predictable.

3.4.4 Sample Structures

To demonstrate this technique we built two example structures. Self-folding was activated by heating each structure in a 130°C oven for less than four minutes. The first structure was a regular icosahedron. This shape was folded from a net which includes three polygonal chains, each consisting of six faces. The fact that the distal faces were able to align demonstrates that the hinges were reliable enough to prevent error propagation along the chains. The second structure was a Miura fold, demonstrating the effectiveness of this method in folding many hinges simultaneously. This work would have been difficult to accomplish by hand because each fold would have to be creased individually. The structure only has a single degree of freedom, so a manual folder would have to rely on the

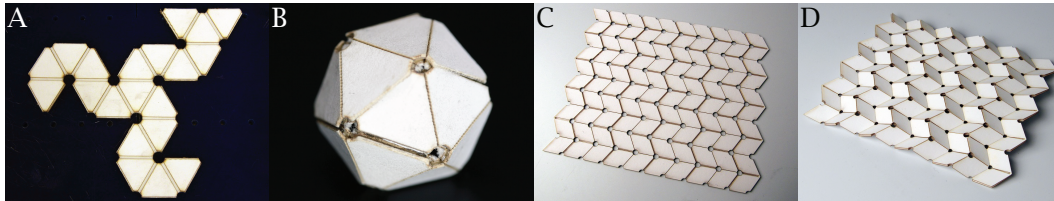


Figure 3.19: Structural samples were built using the uniformly heated composite and heated in a 130°C oven for less than four minutes. (A-B) A self-folding icosahedron before (A) and after (B) folding. (C-D) A Miura pattern before (C) and after (D) folding.

compliance of the material to fold each crease independently.

3.5 Discussion

Each composite presented in this chapter has strengths and weaknesses regarding functional folding. The unidirectional composite is simple to build while allowing for sequential folding, but can only fold in one direction, and cannot reliably produce arbitrary fold angles. The bidirectional electric composite has greater functionality, including higher torques for a given SMP layer, angular control, and folding in both directions. However, the extra layers increase the cost and time of building a device. The uniformly heated composite is least expensive and easiest method, and has the best angular precision, but the uniform folding limits the geometries it can achieve, and lack of dynamic hinges make it ill-suited for machines.

These models and results inform us about certain design rules and limitations to consider as we build more self-folding machines. The torque is governed primarily by the SMP thickness, the SMP contractile stress, and the distance between the SMP and the flexural layer. Because the SMP thickness and stress are fixed for a given off-the-shelf SMP, we can only increase our torque by increasing the offset between SMP and flexural layer.

Current and trace width do not have a large effect on the maximum torque, but they do govern whether that maximum is reached, and how quickly folding is activated. This means that trace width can be used to adjust when a hinge folds, and create sequential folds along a single circuit. Our model also indicates that conduction plays a greater role than convection in heat loss from our hinge, and the thermal conductivity of the surface on which the composite rests will have a substantial effect on hinge behavior.

The data indicates that we cannot achieve angular precision less than 5° with our given materials, which limits our spatial resolution. This appears to be caused by the relaxation we see in the SMP, and the apparent deformability of paper. Our model also indicates that substrate density is the largest contributor to composite weight, which limits maximum face size. With the development of appropriate materials, such as stiffer, lighter substrates and SMPs with greater contractile stress, we believe that these characteristics can be improved.

The analytical model differs noticeably from the experimental measurements, and relies on several simplifying assumptions. It is unlikely to be reliable for designing a self-folding

hinge *de novo*. However, it does provide insight into the relationship between key design parameters and hinge behavior, and is therefore useful for modifying existing hinge designs and predicting gross behavior, such as whether or not a hinge will fold. It's also interesting that even the numerical models differ from the measured values. This could be due to many factors, such as our assumption that the convection coefficient is constant, despite the fact that this value is known to vary with temperature. These linearizing assumptions are necessary, but make predictions difficult.

The material properties of the shape memory polymers are substantially more complicated than our models predict. The mechanics of these polymers undergoing a shape transition are complicated by three factors. The first is that the properties of an SMP in between phases are not well documented. Several efforts have been made to capture the polymer behavior in transition [73–75], but simplified models often miss certain aspects, and more complex models are not useful for identifying larger trends. Another complicating factor is that the material is viscoelastic, and its behavior is dependent on the stress and strain history. Because the material is not actually straining or stressing in our models, but instead transitioning between phases, this behavior is also dependent on the phase-change model. Thirdly, we are operating under strains of 100% or greater, beyond the normal elastic regime of many of these materials. In many of these cases we can apply a 'worst-case' scenario, and find some analytic model for which the generated stress is always greater than some function of time and temperature. This could be used to guarantee that a hinge folds, but would not provide an accurate time-dependent prediction.

In theory there is no difference between theory and practice.

Jan L. A. van de Snepscheut

4

Practical Self-Folding

4.1 Introduction

Chapters 2 and 3 have explored the hinge characteristics necessary for functional self-folding. However, we still need to determine methods for combining these hinges to create arbitrary self-folding machines. In this chapter we demonstrate three broad capabilities necessary for producing any machine: (I) The ability to produce complex geometries, (II) the ability to produce complex mechanisms, and (III) the ability to self-fold autonomously. We identify a minimum set of features, based in part on geometric proofs, that can be combined to achieve these capabilities. We recreate these features using SMCs in two products: an origami-inspired crane structure that demonstrates complex geometry, and a crawling machine that represents both a complex structure and a functional device (Figure 4.1). Much of the content in this chapter is previously published [64, 69].

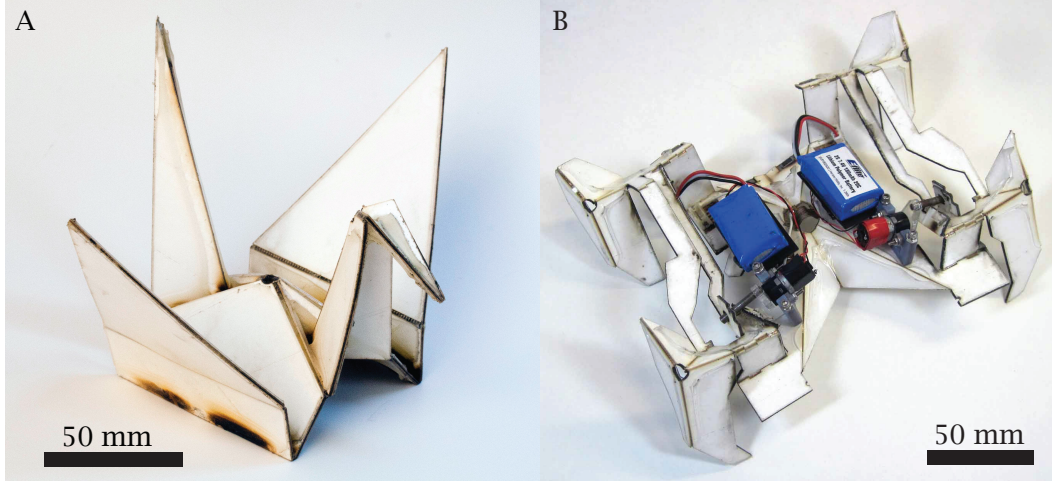


Figure 4.1: (A) An origami-inspired self-folding crane. (B) An autonomously self-folding crawling robot.

4.2 Design

For these devices we use the bidirectional SMC presented in Section 3.3. Self-folding and dynamic hinges are programmed into the composite with layer-specific features, and the final fold angles are controlled through the width of the gap cut into the substrate.

4.2.1 Geometries

The first capability we wish to implement is the production of complex geometries. In theory, a single sheet of paper can be folded into any polyhedral shape [7]. In particular, Origamizer is a practical approach to automating the design of origami fold patterns implemented as free software [8, 9]. This program relies on two features: the ability to fold a crease by an arbitrary angle in a desired direction, up to 180° , and the ability for these

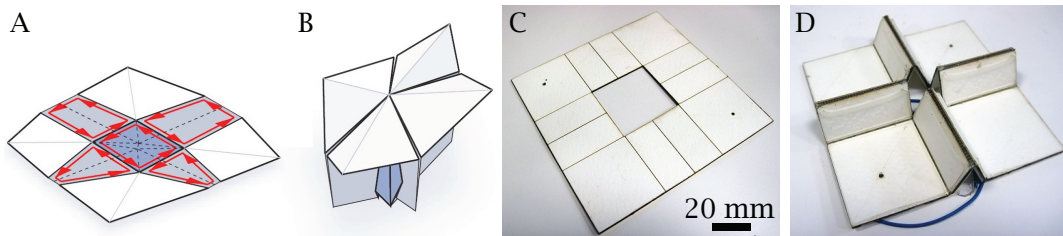


Figure 4.2: (A) Origamizer uses cyclic folds to create concave surfaces. (B) These cyclic folds tuck material into a polyhedral shell (source: Tachi [8] ©2010 IEEE). (C) A self-folding cyclic pattern. This technique has the benefit of being able to cut holes and remove extra material. (D) The cyclic fold closes the hole.

creases to be connected together in any cyclic fold—a collection of creases radiating outward from a point or area. These cyclic folds are necessary for folding concave surfaces, and in Origamizer are used to ‘tuck’ paper inside of the polyhedral shell (Figure 4.2A-B). To demonstrate this concept, we built a standalone self-folding cyclic pattern consisting of twelve hinges (Figure 4.2C-D). Because we can cut holes into our composite, the cyclic fold ‘closes’ the hole instead of tucking the material.

The first feature has already been demonstrated—In Section 3.3.6 we showed that a hinge can fold to an arbitrary angle up to 135° , and folds up to 180° can be approximated with two adjacent 90° folds, as can be seen in Section 5.4. The second feature, cyclic folding, is demonstrated in our two example products, the origami-inspired crane structure and the crawling machine. The crane fold pattern contains four cyclic folds: one cyclic fold with six hinges creates the body, two cyclic folds, each with four hinges, connect the neck and the tail to the body, and one four-edge cyclic fold forms the head. The four-hinged folds are sometimes referred to as four-edge, single vertex (FESV) folds. The FESV fold is noteworthy because it is the subunit of the Miura pattern [28], a well-known fold pattern that can reduce a large surface area into a small volume. It is also notable for having a single degree of freedom, so that each fold angle can be defined by any other fold angle.

In the machine, cyclic folds are included in the fold pattern to create the body and the legs (Figure 4.3G-H). The robot’s body is formed with a six-hinge cyclic fold, which stiffens the body and raises it from the ground, while angling the legs downward (Figure 4.3H). Each leg consists of a FESV fold (Figure 4.3G). Because this fold has a single degree of freedom, the redundant actuation of the folds interact constructively to increase the effective force of the folding. This is necessary because pushing the linkage system into position requires a relatively high force.

Beyond these theoretical requirements, there are physical limitations which must be considered. First, the spatial resolution of a folded structure is limited by the thickness of the folded sheet. The algorithm mentioned above assumes an infinitesimally thin material. Additional rules and algorithms for so-called ‘thick origami’ can be used to account for the non-zero thickness of physical sheets [76]. Second, our composite has a minimum face area depending on the adhesive strength between layers (Section 3.3.5), and this also limits the spatial resolution. Third, a cyclic fold in a real material often produces a high stress at its vertex. To prevent this, we remove a circle at each point where more than

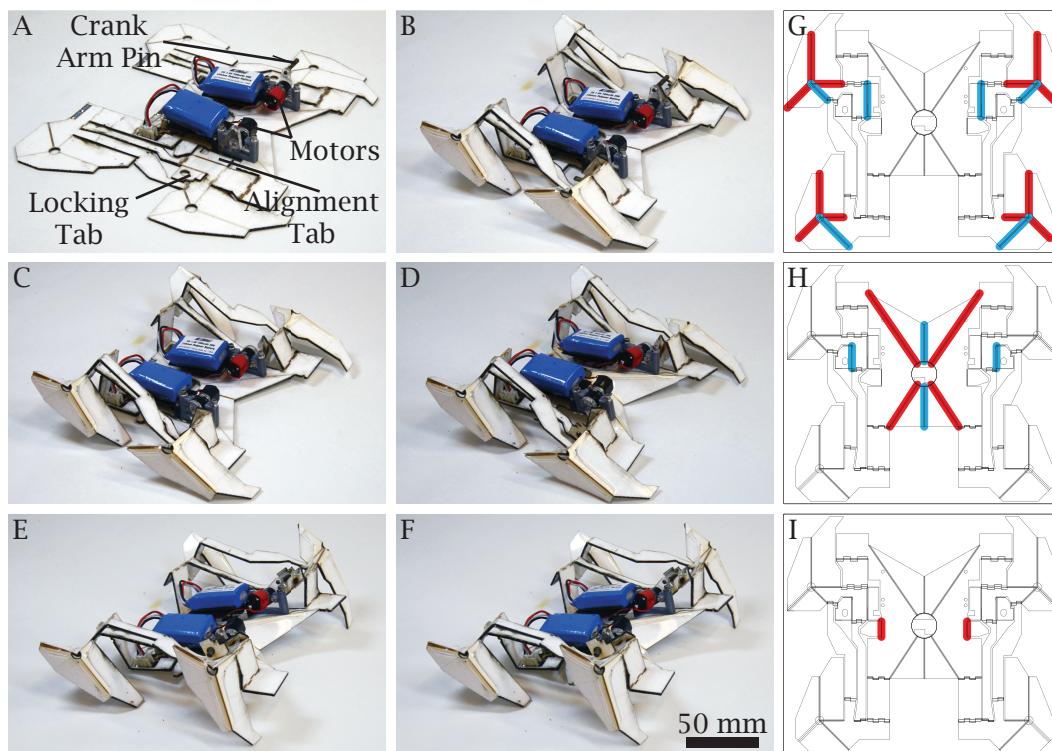


Figure 4.3: The robot folds itself in five steps, three of which are self-folding. (A-F) Depict the robot in each stage of assembly, and (G-I) show the fold pattern and active hinges. Activated mountain folds are highlighted in red, and valley folds in blue. (A) The robot begins in a flat conformation. Folding is initiated 10 s after the batteries are connected. (B, G) The outer legs and alignment tabs fold first. As the legs fold, they bring the linkages into position. (C) The motors rotate 180°, pushing the crank arm pins into notches in the alignment tabs. (D, H) Next, the body and locking tabs fold. (E) The motors turn another 180°, causing the robot to stand up. (F, I) Smaller middle legs fold down for added stability. Once the final folds cool and become rigid, the robot is assembled and ready for operation.

two hinges meet. In the crane and the crawler, these circles are 4 to 17 mm in diameter. Finally, care must be taken that the folds are actuated in the right order. When laid flat, a fold pattern exists at a singularity. It is possible for some hinges to fold in the wrong direction, and if this happens they will be locked into the incorrect position. This can be overcome by adjusting the resistive traces to ensure that vulnerable hinges are activated slightly earlier than their neighbors, biasing their fold in the right direction.

4.2.2 Mechanisms

The second capability we demonstrate is the ability to produce arbitrary mechanisms. In our device, this is accomplished with linkage assemblies—a collection of rigid elements connected by freely rotating joints. It is mathematically possible to trace any algebraic curve [12, 13] with an appropriate linkage mechanism, effectively producing any smooth

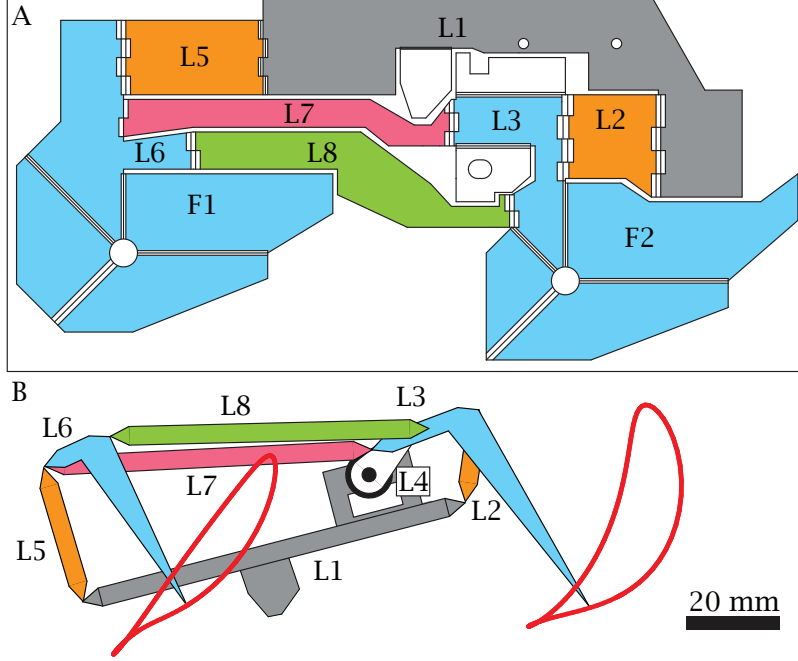


Figure 4.4: (A) The linkages before self-assembly takes place. (B) The linkage assembly after coupling with the motor. The front (right) leg is driven by a four-bar linkage (L1-L4), and the rear (left) leg is driven by an eight-bar linkage (L1-L8). The kinematics of the linkages produce walking trajectories in the front and rear feet when driven by the motors (shown in red). The middle leg (gray) supports the robot when the outer legs are raised. Linkage lengths are given in Table 4.1.

motion. These assemblies can also approximate any curve with a reasonable number of elements [14], indicating this is a functional and versatile method for producing arbitrary motions. To apply these results to self-folding, we need to produce general linkage assemblies with our composite. We demonstrate this by including two symmetric eight-bar linkages in the robot's design. Flat faces act as the rigid elements, and these faces are connected to each other with flexural hinges that act as rotating joints.

Each linkage assembly is driven by one motor and actuates a front and back leg along trajectories that replicate a walking motion (Figure 4.4). The design is built around a standard four-bar linkage that produces the front leg trajectory. Four additional elements are added to produce a similar trajectory in the rear leg. The design was selected to demonstrate that we can combine these linkages in relatively complex assemblies, as well as to reduce the number of motors required for walking while enabling differential actuation

Table 4.1: Linkage lengths.

Linkage	L1	L2	L3	L4	L5	L6	L7	L8	F1	F2
Length	85.0	20.0	24.5	10.0	30.0	15.0	68.5	70.5	50.0	45.0

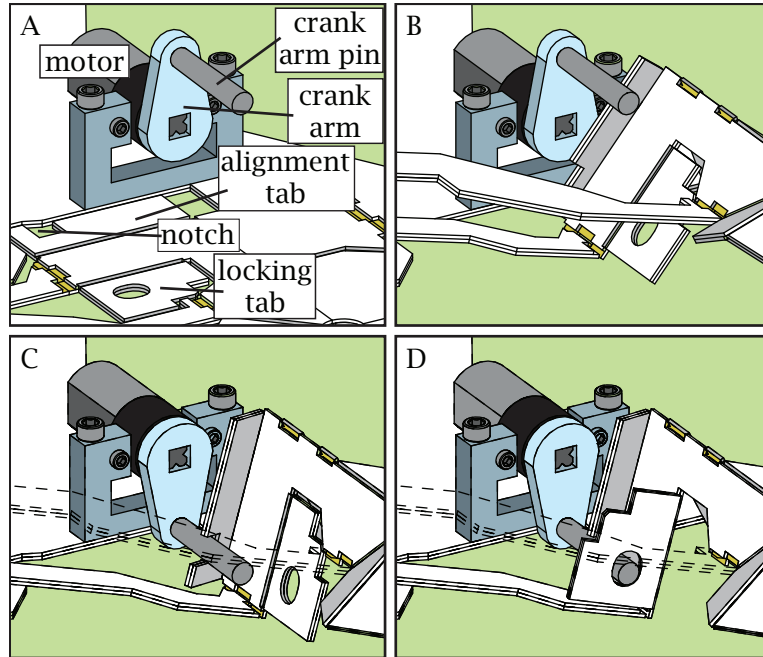


Figure 4.5: The motor couples to the linkage assembly in three steps. (A) Before folding starts, the linkages are in plane with the composite and the crank arm is oriented upward. (B) The legs and linkages fold into position, and the alignment tab folds into place. (C) The motor rotates 180°, pushing the crank arm pin into the alignment notch. (D) The locking tab folds over the pin, coupling the pin to the linkage. In (C) and (D) the obscuring linkage is displayed in outline only for clarity.

for steering.

These linkages also demonstrate precision alignment by requiring that the crank arm pin couple into a specific slot on the linkage mechanism. This is accomplished by first folding tabs with an alignment notch during the folding of the legs (Figure 4.5B). After the legs have folded and the linkages are in position, the motors rotate 180°, pushing the crank arm pin into the notch (Figure 4.5C). A locking tab on the far side of the linkage then folds around the pin, coupling it with the linkage mechanism (Figure 4.5D).

Two additional, static legs are included in the middle of the body to provide stability (Figure 4.4B). The gait is designed so that the front and back legs of one side plant and move simultaneously. Each side alternates planting so that when the legs on the left side are planted, the legs on the right side are in the air. The middle leg is positioned to support the robot when the dynamic legs are up by providing three points of contact – the middle leg on one side and the dynamic legs on the other.

In addition to the desired foot trajectory, there are other considerations when designing linkages for folded machines. The linkage design is constrained so that the lengths sum

to zero. This ensures that the linkages can lay in a flat conformation prior to folding, and do not have to change length during assembly (Figure 4.4A). While it is possible to change the effective length of linkages through folding, we chose not to in order to simplify the design.

There are tradeoffs to be made when determining the linkage widths. Wider linkages and hinges can support larger loads and mitigate off-axis twisting. In the crawling machine, the off-axis stiffness of the hinges are increased by castellating the hinges—meaning that the hinge line is staggered in a square wave pattern. However, even with castellation, we observed that the minimum linkage width is at least seven millimeters in our crawling robot, and is dependent on the location of the hinge in the fold pattern. We determined the minimum widths through iteration of the robot design.

However, there are also reasons to make the linkages narrow. Because the machine is cut from a single sheet, the linkages are arranged side-by-side, and each additional linkage must be placed farther from the machine's center. This becomes an issue if the area of the machine is limited for fabrication or material reasons. It also increases the distance between the center of gravity and the end point of the mechanism, resulting in a higher off-axis torque, which deforms the linkage trajectory and increases joint fatigue. This problem is exacerbated by the presence of coupling features, which must also be a certain size or risk delaminating, and must be included within the linkages. In the case of our machine, the total width of the linkage assembly varies from 15 to 32 mm.

Finally, the linkage design is constrained by the torque exerted by the folding hinges during assembly. During the folding process, the linkages must be lifted against gravity, the passive hinges must be folded into the correct position, and the feet must move slightly, overcoming ground friction. Some linkage designs require more torque to self-assemble than the actuated folds can provide. The final linkage design for the robot was selected with these constraints in mind and using a combination of kinematic simulations and prototype testing.

4.2.3 Autonomous Folding

The third capability of the composite, autonomous folding, is demonstrated by the robot through embedded circuitry and an onboard power supply (Figure 4.6). Both assembly and locomotion are controlled by a single microcontroller with six outputs: three binary outputs to control folding, and one binary and two pulse-width-modulation outputs to

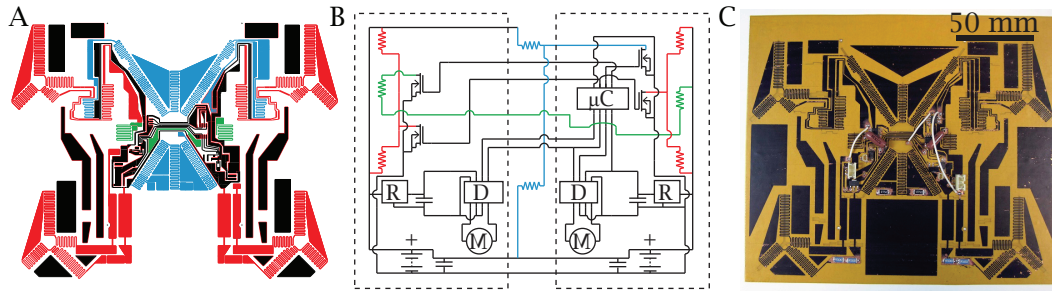


Figure 4.6: The electrical circuit of the self-folding robot. The crawling machine uses a flexible printed circuit board (PCB) integrated into the laminate to control both assembly and locomotion. (A) The trace pattern of the machine's PCB. Red, blue, and green traces indicate the current path during activation of the first, second, and third folding steps, respectively. (B) The machine's circuit diagram, including one microcontroller (μC), two motor drivers (D), two voltage regulators (R), two motors (M), two batteries, and four MOSFETs. (C) The flexible PCB layer of the machine, with all electrical components installed.

control the two motors. Folding is triggered by current that is gated by four MOSFETs. Locomotion is actuated through the motors, which are controlled via motor driver integrated circuits. The self-assembly process comprises five steps, three of which involve actuated folding (Figure 4.3):

1. From 0 to 75 s, the outer legs and dynamic linkages fold into position, and alignment tabs fold into place.
2. At 85 s, the motors turn downward 180° to align the crank arm pins with the alignment tabs.
3. From 85 to 182 s, the body folds and locking tabs fold over the crank arm pins.
4. At 212 s, the motors turn 180° , causing the robot to stand up.
5. From 212 to 260 s, the middle legs fold downward.

Self-assembly is programmed to occur ten seconds after power is connected to the circuit, and each step occurs at a preprogrammed time. After each folding step, 10 to 30 s were allowed to pass before the next step commenced so that the hinges could cool and harden. Power is supplied from two batteries with a nominal voltage of 7.4 V. The resistive circuits are voltage limited, so the resistance of each trace is adjusted to result in a current that varies from 2 to 2.5 A for desired heating. Voltage to the microcontroller and motor drivers is controlled by two voltage regulators.

This method of autonomous self-folding presents a few design challenges. First, our flexible circuit only has a single layer, so multiple sets of resistive traces must be laid out so that they do not intersect. Each trace must also contain a MOSFET which is connected to a central microcontroller, requiring additional wiring to a central location. For the crawler, we had to include three off-surface wires and two through-hole resistors in order to route the traces (Figure 4.6C). Second, the traces must be drawn to minimize the heat generation everywhere except at the self-folding hinges. Non-heating traces must be made as wide as possible, which is made more difficult by having to pack multiple traces in small areas. During the design process, we witnessed problems with excess heat including pre-activation of folding hinges, melting solder, and thermally overloaded integrated circuits. Finally, the resistance for each trace must be controlled so that the current is approximately 2.5 A for a given voltage. A voltage regulator could be used in this situation, but that would require additional traces and components, which make the first two challenges more difficult. Instead, we included surface mount and through-hole resistors to increase the trace resistances where necessary. This method should be used sparingly, as the resistors produce a substantial amount of heat.

4.3 Fabrication

The robot and crane were assembled in a method similar to the SMCs in Section 3.3. Both pieces required two sheets of 250 μm thick PS and two sheets of 510 μm thick paper (Figure 4.7B, Appendix A.4). The CuPI layer was masked using a solid ink printer (Colorcube, Xerox) (Figure 4.7A) and etched with ferric chloride (CE-100, Transene). Each layer was machined individually with layer-specific features (Figure 4.7C) using a CO₂ laser system

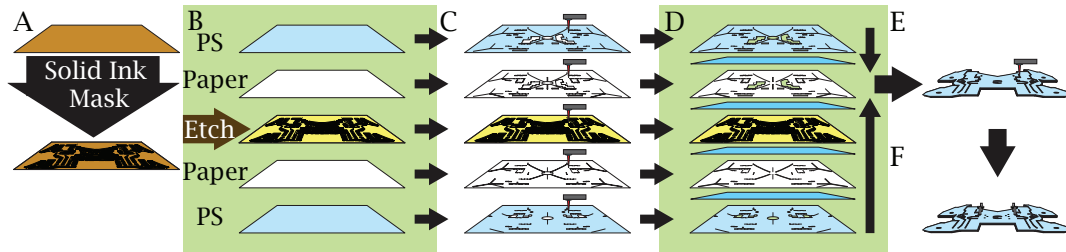


Figure 4.7: The fabrication process of the self-folding robot. (A) A mask is applied to a sheet of CuPI using a solid ink printer. (B) The CuPI is etched with ferric chloride. (C) The CuPI layer, as well as two sheets of PS and two sheets of paper, are laser-machined with layer-specific features. (D) These layers are bonded together by hand, using silicone tape. (E) The final composite is laser-machined again. (F) Electrical components, motors, and batteries are added manually.

(VLS 2.3, Universal Laser Systems), and then pin-aligned and bonded together with silicone tape (Figure 4.7D). The final composite was laser-cut (Figure 4.7E). Electrical and electromechanical components were manually installed when the robot was in the flat conformation (Figure 4.7F).

For the robot, electrical components include seven integrated circuits, eight resistors, and four capacitors. Additional components include two 3.9 g DC motors and two 7.4 V, 180 mAh LiPo batteries. A detailed part list can be found in Appendix A.8. Mounts for the batteries and motors were 3D printed using an Objet 30 Scholar and installed with screws.

The crane composite took approximately one hour to build by hand. Fabricating the machine composite and installing the electrical components took two hours by hand. This was possible in part because the composite is two-dimensional, allowing for easy installation and soldering. Our process was designed around readily available parts and materials, but the assembly time could be substantially reduced and completely automated with the use of pick-and-place electrical component assembly machines and automated adhesive dispensers.

4.4 Results

The crane folded in approximately three minutes and two sequential steps. Two amperes of current were first supplied to all except the two most distal wing hinges, causing the body to fold. Once it had folded, two amperes were supplied to the remaining distal hinges to bring the wings down. The current was supplied from an external power supply and manually controlled by an operator observing the folding process.

The robot self-assembled in 270 s, after which it was able to walk without human intervention (Figure 4.3). The linkage mechanisms operated effectively, demonstrating both the efficacy of the composite's dynamic hinges, and its ability to precisely align folds to couple the motors to the linkages. When operating, the robot moved at a speed of 0.43 body lengths per second (5.4 cm/s). It was also able to turn at an average speed of 0.56 rad/s with an average turning radius of 6.1 cm. The folding process required approximately 8.8 kJ of electrical energy to activate. We calculate that the mechanical work required to assemble the machine was at least 3.8 mJ, based on the mass (78 g) and final center-of-mass height (10 mm) of the machine.

Out of three attempted self-assemblies, one robot was able to complete the assembly

process and achieve the desired functionality. In the other two, a single hinge failed to fold into the necessary position. In one robot, the locking tab failed to align with the crank arm pin, preventing coupling. In the other, the locking tab failed to fold at all, and the PSPS in that area delaminated from the paper. During these trials, the failed hinge was pushed into place manually so that the assembly process could finish and we could observe if there were other points of failure. Considering that each robot consists of 28 self-folding hinges, the hinge success rate is 98%.

4.5 Discussion

The robot embodied features that can be combined to create arbitrarily complex machines. By demonstrating self-folded cyclic folds and linkage mechanisms, and integrating them into functional machines, we have shown that, geometrically, self-folding can produce a wide range of structures and mechanisms. By embedding all of the necessary electrical components into the body of the robot, we have demonstrated that the self-folding process can occur autonomously.

However, there are still limitations to what we can make through self-folding. The precision and spatial resolution of our technique limit the size and complexity of a potential machine. Seemingly small errors of 5° and hinge failure rates of 2% propagate, resulting in incomplete folding in two out of three robots. The low stiffness of our materials result in inefficient mechanisms and reduced lifespan. Packing multiple sets of resistive traces on a single layer limits the total number of folding steps. Many of these problems are exacerbated from using only a single functional layer, which limits the total surface area from which we can create features.

Most of these limitations are due to the hinge-level capabilities in our composite, such as angular precision, maximum fold angle, folding torque, minimum hinge length, and composite thickness. As these capabilities improve, so will the complexity and functionality of self-folded robots.

4.5.1 Design Process

One strength of this technique is the speed of the development cycle. This robot design evolved through prototyping over 40 iterations (Figure 4.8). Many limitations, such as minimum hinge size, trace width, and linkage lengths, were determined experimentally,



Figure 4.8: The self-folding robot was designed through over 40 iterations, 6 of which are shown here.

and this would have been prohibitively expensive using traditional machining techniques. However, we were able to design, build, and test new robots quickly, sometimes in less than four hours.

4.5.2 Adaptability

The materials and components in this robot were chosen in part because of their low cost and availability. The robot was designed to operate indoors in a typical room environment, and the fold pattern was chosen to demonstrate the complexity that the SMC was capable of. However, there are many ways to alter the self-folding technique for different applications and environments.

For the machine presented here, folding was initiated by a simple timing program in the microcontroller, designed to trigger assembly ten seconds after the batteries were connected. However, more complex triggers could be integrated, including wireless activation or response to an environmental change.

We focused on an origami style of folding, meaning that everything was folded from a single functional layer. However, there are other types of folding. Pop-up style folding involves multiple functional layers stacked on top of each other and connected by hinges. It has been used to build mesoscale devices, and has several advantages over origami-style folding [40, 77]. Pop-up devices generally have a single degree of freedom, which reduces folding errors. Because of the multiple functional sheets, features don't need to

be pulled in from the edges. This increases precision, because errors don't propagate along sequential folds, and it reduces the torque necessary for assembly by reducing the moment arm. It also reduces the footprint of the unfolded device, allowing larger structures to be built from similarly-sized laminates. All of these strengths could greatly improve the performance of our self-folding techniques.

Depending on the application, the stimulus for self-folding can be changed in a variety of ways. If the inclusion of a circuit layer is prohibitively expensive, but self-assembly is occurring in a dedicated facility, sequential activation could be accomplished via an external heater such as a laser [55]. For simpler geometries, a modified technique could be accomplished by heating the composite in an oven [78]. For space applications, an embedded heating source may not be necessary. Black lines could be used to absorb thermal radiation from the sun along the hinges [61, 78]. For environments with large thermal variations, the transition temperature can be raised as high as 150 °C [79], and SMPs can be used that are triggered by non-thermal stimuli. There are several published examples of SMPs that exhibit a shape change in response to water [80], light [81], magnetic fields [82], or mechanical stress [83].

4.5.3 Energy Consumption

The electrical energy required during folding is the dominant factor in determining the size and type of batteries that are installed and carried, and reducing this energy requirement would substantially decrease the weight and cost of the machine. It is important to note that the amount of mechanical energy released during folding is decoupled from the amount of energy needed to trigger that folding. The mechanical energy density E_m is a function of the shrink ratio S_R and contractile stress σ_c of the SMP, and can be expressed, assuming a perfectly elastic contraction, by Equation (4.1). For the PS in our composite, $E_m \approx 350 \text{ kJ/m}^3$.

$$E_m \approx \sigma_c (S_R - 1) / 2 \quad (4.1)$$

The specific energy E_a necessary for activation is a function of the heat capacity ρc_p and relative transition temperature ΔT of the material. For PS, $E_a = 134 \text{ MJ/m}^3$.

$$E_a = \Delta T \rho c_p \quad (4.2)$$

This would be the activation energy if the SMP was heated with perfect efficiency. However, heat loss due to convection and diffusion are always present. The electrical energy E_e released per meter hinge length is a function of the resistance, current, and the time t_e spent folding.

$$E_e = I^2 R t_e \quad (4.3)$$

For the hinges in the crawling robot, $E_e \approx 5 \text{ kJ m}^{-1}$. These hinges have 250 mm^3 of contractile SMP per meter of hinge length, so the electrical energy released per unit volume of SMP is approximately 20 GJ/m^3 .

There are two approaches to reducing the energy expenditure. The first is to reduce E_a by altering the transition temperature of the SMP. Xie et al. have already demonstrated a practical method for setting the transition temperature of an epoxy SMP anywhere from room temperature to 89°C [84]. While reducing the transition temperature of a self-folding machine would make the device more susceptible to premature assembly due to heat, in many circumstances this risk would be worth the substantial reduction in activation energy. Based on the models in Chapter 3, we estimate that if we reduced the transition temperature of the SMP to 60°C , we could reduce the activation current by 70% and the energy expended during self-assembly by 50%.

Alternatively, we could reduce E_e by delivering a larger current at a higher voltage. While this requires greater power, the reduction in folding time would reduce the total expended energy. Based on our thermal model in Chapter 3, Increasing the voltage and current by 40% would double the power and reduce the fold time by 93% (expected fold time of 3 s instead of 45 s), resulting in total energy expenditure of 86% less than our current implementation. The complication with this technique is that if the current is supplied for too long a period, the SMP would overheat and melt. Because of this, we recommend that this method be used with sensors embedded in the hinges to provide angle and temperature feedback during the folding process. In this way, the controller would know when to switch off current to a folding hinge.

The size of the machine will also affect the power expended during self-assembly. For a given self-folding device, the energy released is relatively uniform along the length of the hinges. For a machine of a given complexity, the total length of the hinges will scale directly with the length of machine, and so the energy consumed during assembly will also

scale directly with machine length. Based on our results in Chapter 3, SMP thickness and hinge torque have little effect on power requirements, so the weight of the machine would have a minimal impact on energy consumption during assembly. However, more complex machines will require more folds, and therefore more energy.

4.5.4 Manufacturing Comparison

Because of its potential as a form of printable manufacturing, self-folding draws comparisons to other manufacturing methods. In particular, we're interested in how self-folding compares to other shaping processes—the subset of manufacturing processes that change the geometry of the raw material. Shaping processes can be divided into three categories: additive manufacturing, sometimes referred to as solidification or particulate processing, involves taking a raw liquid or powdered material, forming it into the desired shape, and hardening it. Common additive processes include injection molding, metal casting, and 3D printing. Subtractive manufacturing, also known as material removal processing, involves removing material from a solid shape. This encompasses most traditional machining methods such as milling and lathing. Finally, there is deformation processing, in which a solid material is plastically deformed through force. This method includes sheet metal bending and self-folding.

We are interested in the relative cost and speed of manufacturing equivalent devices across different processes, and determining when self-folding is an appropriate manufacturing process. We compare self-folding to other machining methods by considering as a test-case the crane structure shown in Figure 4.1A. We treat this shape in three possible forms, depending on the manufacturing method: Either a flat sheet folded into our desired shape, a solid volume in which the material has been added to the structure, or a solid volume that has been formed by removing surrounding material from a rectangular cuboid. Our estimated values for time and cost for setup and unit production are shown in table 4.2, and the calculations for these values can be found in Appendix D.

3D printers have a wide range of equipment costs because there is a sizeable market for consumer-grade printers. It is reasonable to get a printer for \$1000 [85], and many industrial printers are available for \$10k to \$100k [86]. Depending on the quality, printable polymers can cost between \$30 [87] and \$500 per kilogram. Once a solid geometry is generated in a design program, setting up the printing process only takes a few minutes

and does not require significant training. Because of the wide range of options, we include both industrial and consumer-grade 3D printers in our comparison.

Injection molding is the process of filling a mold with liquid polymer, usually by pumping it in under high temperatures, and then allowing it to cool and solidify. It is commonly used for mass-manufacturing plastic parts, and the speed of production is governed by the injection time and cooling time, which are determined by the part quality and size. The approximate setup costs vary between \$10k and \$80k, and per-unit costs of \$0.10 to \$3 are common [88].

Milling, lathing, and other machining processes are common methods for prototyping parts because a single machine can produce arbitrary geometries with a finite set of tool bits. It is, however, expensive; machining takes time, and even the simplest parts require a trained user. More complicated parts require extensive experience, and most machine shops are manned by professionals, leading to labor costs ranging from \$50 to \$100 per hour. Computer-controlled machines can speed up the process and improve precision, but these machines are more expensive. Typical set up costs are dominated by programming and labor, and vary between \$50 and \$500, while each unit can cost between \$10 and \$400 in labor and material [88].

Sheet metal stamping is an excellent method for producing large volumes, typically 100k to 10M units, because of its speed and relatively low cost. This is in part due to the fact that only a small amount of material is used, and often requires only a single stroke to produce the part. Total set-up costs can run between \$20k and \$200k, while typical unit costs range between \$0.06 and \$0.60 [88].

Table 4.2: Estimated costs and time associated with manufacturing a crane.

Method	Machine Cost	Setup Time	& Cost	Unit Time	& Cost
<i>Additive</i>					
3D Printing (industrial)	\$25k	0	\$0	21 h	\$270
3D Printing (consumer)	\$3k	0	\$0	7 h	\$41
Injection Molding	\$50k	196 h	\$7.8k	28 s	\$0.49
<i>Subtractive</i>					
CNC Milling	\$85k	1.5 h	\$90	9 min	\$37
<i>Deformation</i>					
Sheet Metal Stamping	\$150k	184 h	\$7.4k	8 s	\$0.15
Resistive Self-Folding	\$13k	0	\$0	1 h	\$24
Oven Self-Folding	\$12k	0	\$0	0.5 h	\$2

The prices for our self-folding method base costs off of the low-volume, high margin prices that we buy in lab, and we assume that labor is free. Many of our processes could be sped up with the right materials (such as wider tape for faster bonding) or automated in a straightforward process.

When comparing these fabrication methods, it is worth considering the resolution they are capable of. For injection molding, milling, and sheet stamping, the resolution is correlated with manufacturing cost, but features at length scales of 1 μm or smaller are possible [89–91]. For 3D printers, The resolution is dependent on the printer. The Objet 30 Pro can print layers as thin as 16 μm and has a print accuracy of 100 μm [92], while the Form 1 can print 25 μm thick layers and features as small as 300 μm [93]. In contrast, our self-folding technique has a the minimum folded face size is 10 mm and the composite thickness is approximately 2 mm. However, other techniques have demonstrated self-folding hinges under 10 μm long [62].

The pricing is highly dependent on the final product, including whether it has any electromechanical components, which would require additional assembly steps. This is particularly noticeable for the resistively self-folded composite, in which the circuit board increases the price substantially, but provides an existing substrate for other electrical components. However, our estimates indicate that this technique is well-suited for production volumes of 10 to 1000 units, and could be competitive with 3D printing as a rapid prototyping technique.

We see in order to move; we move in order to see.

William Gibson

5

Sensors for Self-Folding Machines

5.1 Introduction

Many machines require a way to accept external inputs, either for sensing the environment or interacting with a human operator. Traditionally, sensors have operated using a combination of electrical and mechanical systems to translate a physical property into an electrical signal, which is then interpreted by the control system of the machine. Measured properties include contact, distance, force, velocity, and temperature, and each of these properties can be measured in different ways. For example, physical contact can be measured with latches [94], pushbuttons [95], or mercury switches [96], while force can be measured by a spring [97] or by a capacitive change between two plates [98]. The majority of existing sensors require discrete components and three-dimensional features.

In order to make arbitrary and functional self-folding machines, we must demonstrate that self-folding is capable of producing functional sensors and input mechanisms. In

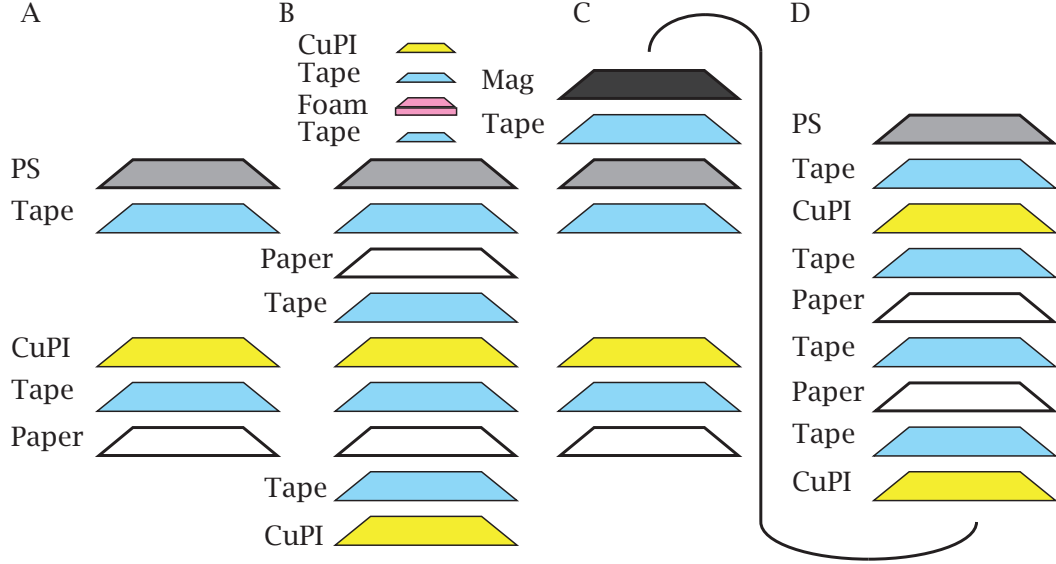


Figure 5.1: The composites for each of the three sensor designs were based off of the unidirectional composite presented in Section 3.2. This composite consists of three layers: the PS, the CuPI circuit, and the paper substrate. (A) The capacitive contact sensor does not require any additional layers; the capacitive pad is included in the original circuit layer. (B) The mechanical switch includes three additional layers: a second CuPI circuit layer on the bottom, a small foam pad on the top of the PS, and a small copper pad on top of the foam. (C-D) The velocity sensor consists of two unattached composites. (C) The frame composite includes an additional magnetic layer on top. (D) The slider includes an additional CuPI layer on the bottom to house the sensor loop, and an additional paper layer for structural support.

this chapter we present designs for three sensors built from planar materials that can be integrated into self-folding devices. We designed and built a capacitive contact sensor, a bistable switching mechanism, and an electromagnetic velocity sensor, all based on our unidirectional composite from Section 3.2. We accomplish this by integrating new, functional layers into the self-folding composite and creating 3D features and mechanisms through folding. We integrate the capacitive sensor and mechanical switch into a self-folding lamp, demonstrating the use of these sensors in functional devices. Much of the content in this chapter is previously published [99], but some of the models have been modified to reflect our improved understanding of these systems.

5.2 Capacitive Touch Sensor

The capacitive sensor consists of a copper plate embedded in the flexible circuit board that contains the heating traces. The laminate does not require any additional materials (Figure 5.1A).

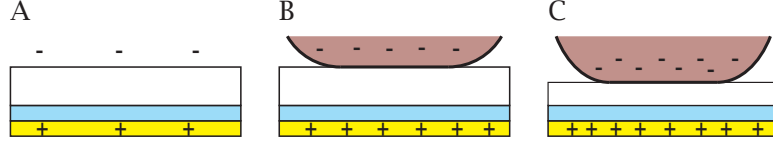


Figure 5.2: The capacitive sensor consists of a copper pad (yellow) underneath a paper substrate (white) and silicone tape (blue). The capacitance between the plate and the air (A) is small, but the capacitance when in contact with a finger (B) is relatively high. If the finger presses down (C), the paper and silicone compress, further increasing the capacitance.

5.2.1 Model

The capacitance C of two parallel plates is governed by Equation (5.1):

$$C = \epsilon \frac{A_p}{d_p} \quad (5.1)$$

ϵ is the relative permittivity of the dielectric layer, d_p is the distance between the plates, and A_p is the overlapping area. In this case, the copper pad makes up one plate, and the second plate is the surrounding environment. When the switch is not in use, the atmosphere acts as the second plate and the corresponding capacitance is low (Figure 5.2A), but when a finger is pressed to the sensor, the finger becomes the second plate and the capacitance increases (Figure 5.2B). The dielectric layer is made up of the silicone tape and paper substrate. When the finger is lightly pressed on the sensor, d_p is the resting thickness of the dielectric layer. However, if pressure is applied, the paper and tape will compress, reducing d_p and increasing C (Figure 5.2C).

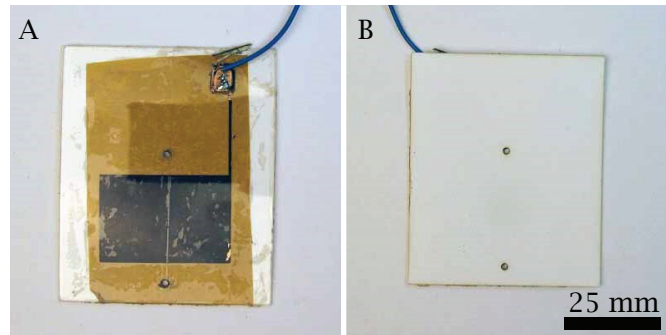


Figure 5.3: Image of the front (A) and back (B) of the standalone capacitive sensor. The yellow is the polyimide layer, and the black is the wax used to mask and etch the circuit. The copper is underneath the wax.

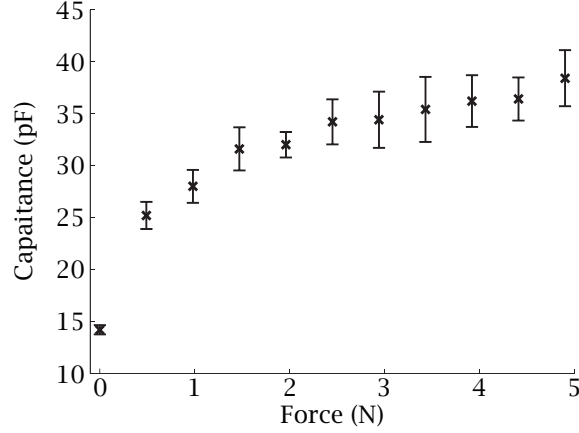


Figure 5.4: The measured capacitance as a function of finger force. Error bars indicate standard deviation, $N=5$.

5.2.2 Results

A standalone capacitive sensor was built (Figure 5.3) and tested manually. The capacitance was measured with a surface-mount device tester while the user applied increasing force through their finger in increments of 0.49 N. The sensor registered a capacitance of 25 pF when first touched at 0.49 N, and the capacitance increased as the force increased from 0.49 to 4.9 N (Figure 5.4). The average standard deviation of the capacitance at each point is 2.0 pF. Over this range, the mean capacitance increases from 25.2 to 38.4 pF, indicating that, after contact, the capacitance increases 3.0 pF/N. Because of this, we expect a standard deviation of 0.67 N for a given capacitance reading.

5.3 Mechanical Switch

The design of the self-folding switch is inspired by the compliant mechanisms presented by Howell [100]. We designed a four-bar linkage that acts as a bistable mechanism based on existing kinematic models [100, 101]. In order to create this mechanism, we used sequential folds to first bring the linkages into position, and then trap one end, effectively closing the loop (Figure 5.5A-C). The self-folding hinges are stiff but compliant, so the hinge that folds in Figure 5.5B is effectively a spring for kinematic purposes.

The composite for this device is similar to the basic self-folding composite, but includes three additional layers (Figure 5.1B). A second circuit layer is included between the heating circuit and the paper substrate. This layer contains the sensor circuit, which is a copper

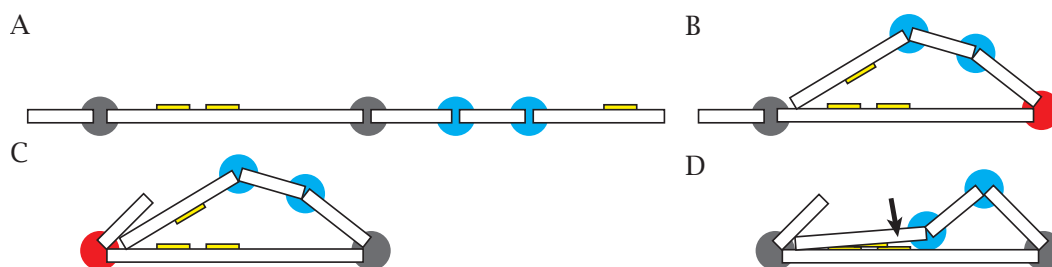


Figure 5.5: The mechanical switch is a four-bar linkage mechanism created through sequential self-folding. Blue indicates a passive hinge, red indicates a hinge that is self-folding, and gray is a self-folding hinge that is inactive. The rightmost hinge is stiff but still compliant, and acts as a spring.

loop broken at one point. A small foam pad with a copper layer is attached to the top paper layer. The copper pad acts as a bridge. When the sensor is assembled this copper pad is folded over, facing down and located above the break in the sensor loop (Figure 5.5C). when the switch is flipped, the pad is pressed down and makes contact with the circuit layer, closing the loop (Figure 5.5D). The foam layer allows the pad to be compliant, ensuring a connection between the two copper layers.

To validate the design, a standalone switch was fabricated and induced to self-fold by supplying two amperes of current in two sequential steps (Figure 5.6A-B).

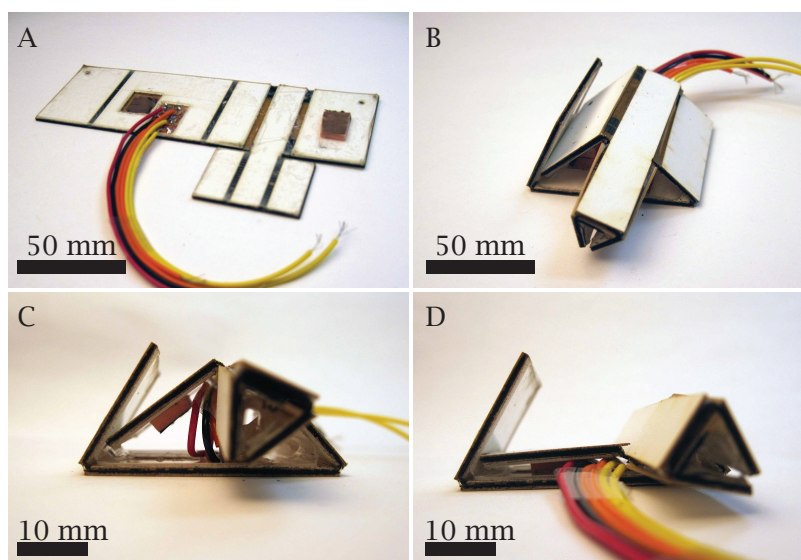


Figure 5.6: (A) A standalone mechanical switch before folding. (B) The switch after folding. (C) The switch in the open position. The foam contact pad can be seen on the upper linkage. (D) The switch in the closed position. The foam pad is pushed against the bottom circuit layer, closing the circuit.

5.4 Electromagnetic Velocity Sensor

The standalone velocity sensor consists of two components: a slider and a frame. The frame has two 90° folds on either side set nine millimeters apart, so that they approximate a single 180° fold. These folds constrain the slider motion to a single degree of freedom and hold it flush with the frame. The frame also has a single magnetic Halbach array on top (Figure 5.1C). This array is a row of magnets arranged so that each set of dipoles is rotated 90° relative to its neighbors [102]. It is commonly used in refrigerator and other sheet magnets. Because of constructive and destructive interference, This orientation creates a sheet with a negligible magnetic field on one side and a strong alternating field on the other.

The slider has a handle on top for manual control and an additional circuit mounted to a second paper substrate layer on the bottom (Figure 5.1D). The extra circuit is the sensing layer, and it contains a copper coil in which a voltage is induced by the magnetic flux produced by Halbach array. In order to maximize the flux, the coil consists of fingers arranged in a row with the same spatial frequency as the magnetic array, so that it can be positioned over the positive (or negative) regions of the array only (Figure 5.7). This design is similar to many magnetic encoders, which produce a voltage peak when moved a certain step length [103].

5.4.1 Model

Faraday's law of induction states that a magnetic field induces a voltage V along a closed path according to the following equations:

$$V = -\frac{d\Phi}{dt} \quad (5.2)$$

$$\begin{aligned} \Phi &= \int_S \vec{B} \cdot \hat{n} dA \\ &= \int_S B_y dA \end{aligned} \quad (5.3)$$

A is the area inside of the path, Φ is the magnetic flux through that area, \vec{B} is the flux density, and B_y is the flux density through the surface. The strong-side magnetic field of the Halbach array has a spatial period λ and spatial angular frequency $k = 2\pi/\lambda$. Equation (5.4) expresses the magnetic potential φ on the strong side of the array [104, 105], and

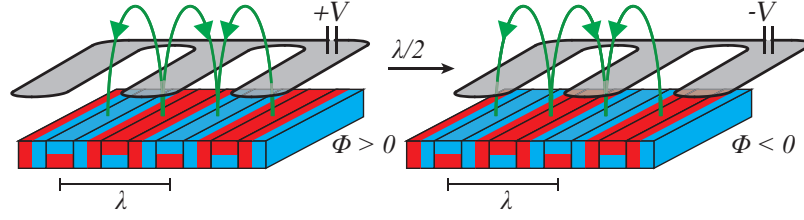


Figure 5.7: A Halbach array is a series of permanent magnets in which adjacent dipoles are rotated 90° , resulting in an alternating magnetic field on one side of the array with a spatial period λ . A serpentine copper loop with a similar spatial period is held parallel to the magnet. When the coil moves, the magnetic flux Φ changes, inducing a voltage V in the loop.

Equation (5.6) expresses the magnetic flux density B_y , which is dependent on the magnetization M_0 of the array, the position y above the array and x alongside it, the thickness d of the array, and the free-space permeability μ_0 .

$$\varphi = -\frac{M_0}{k} (1 - e^{-kd}) e^{-ky} \cos(kx) \quad (5.4)$$

$$\vec{B} = -\mu_0 \vec{\nabla} \varphi \quad (5.5)$$

$$\begin{aligned} B_y &= -\mu_0 \frac{\partial \varphi}{\partial y} \\ &= M_0 (1 - e^{-kd}) e^{-ky} \cos(kx) \end{aligned} \quad (5.6)$$

We can apply this equation to our coil geometry. The coil is made up of N fingers extending from a base, so that the entire loop is similar to an array of smaller loops all connected at one end (Figure 5.8C). This array has the same spatial period λ as the Halbach array and each finger has a length $l = \pi/k$ that is half of the period. The width w of each finger is also equal to the width of the Halbach array. The coil is held flush with the surface of the Halbach array, so d and y are both constant, and the other constant terms can be lumped into the maximum flux density B_0 at the surface of the magnet. With these assumptions, we can solve for V as a function of the position r of the coil relative to the

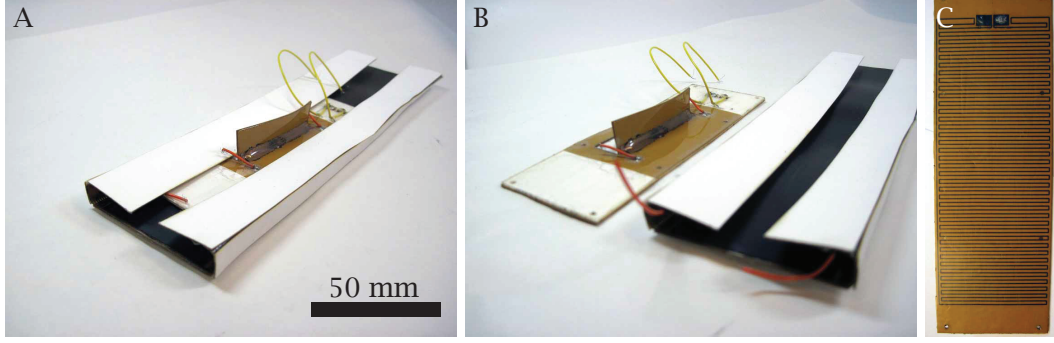


Figure 5.8: (A) The self-folded electromagnetic velocity sensor. The slider and frame fold together. (B) The slider and frame shown separately. (C) The bottom of the slider contains a copper loop consisting of several fingers extending along its width. These fingers have a spatial period matching the magnetic field of the Halbach array.

magnet and the velocity $v = dr/dt$.

$$B_y = B_0 \cos(kx) \quad (5.7)$$

$$\begin{aligned} \Phi &= NwB_0 \int_r^{r+\frac{\pi}{k}} \cos(kx) dx \\ &= \frac{-2NwB_0}{k} \sin(kr) \end{aligned} \quad (5.8)$$

$$V = 2NB_0w \cos(kr) \frac{dr}{dt} \quad (5.9)$$

As the slider moves, the copper loop produces a sinusoidal signal (5.9). The velocity of the slider relative to the frame can be determined from either the frequency or the amplitude of the signal.

5.4.2 Results

The velocity sensor self-folded with the application of two amperes to the resistive circuits (Figure 5.8A). The signal voltage from the slider was measured using an external microcontroller (Uno R3, Arduino) after the signal was amplified with an operational amplifier (LM741, Texas Instruments) circuit with a gain of 459.33. The slider was manually moved through the frame at different velocities. The velocity of the slider was measured via video recording, while the voltage amplitude was recorded.

The velocity v varied between 0 and 0.5 m/s, corresponding to a range in signal voltage amplitude V from 0 to 9 mV. The relationship between velocity and voltage appeared to be linear (Figure 5.9). The relationship between velocity and amplitude was fit with a linear

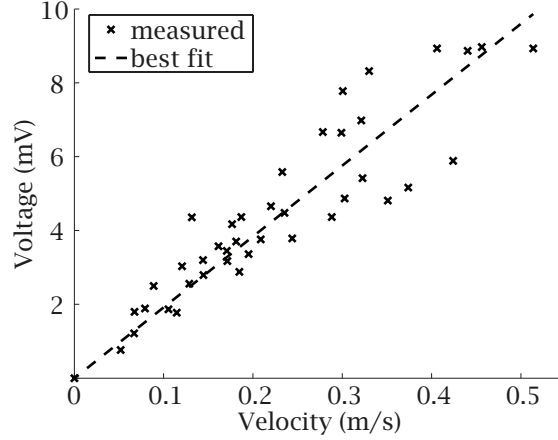


Figure 5.9: The measured signal voltage amplitude is shown as crosses as a function of slider velocity. The dashed line indicates a linear best fit model with an R^2 value of 0.8234

model, $V = 19.2v$ with an R^2 value of 0.8234. From this relationship we can define a measured signal coefficient $C_m = 19.2 \text{ mVs m}^{-1}$. From Equation (5.9) in our model, and given that for our sensor, $\lambda = 3.2 \text{ mm}$, $N = 27$, $w = 45 \text{ mm}$, and maximum magnetic field of our Halbach array was measured to be 9.2 mT , we estimated an ideal signal coefficient $C_i = 30.6 \text{ mVs m}^{-1}$. This difference could be due to an error in matching the copper loop period to the magnetic field period. Even small errors would propagate over the length of the sensor, resulting in the flux in some fingers cancelling out the flux in others. The signal could also be affected by the width of the copper trace, which we did not account for, or variations in the distance between the slider and the frame.

5.5 Lamp

We constructed a self-folding lamp to demonstrate that printable sensors could be integrated into a functional device (Figure 5.10). The lamp incorporated a capacitive sensor and a bistable switch, which were both used to turn the lamp on and off, and an LED to provide light. The lamp was folded in eight sequential steps by selectively supplying the resistive circuits with two amperes of current. The angle of each fold was limited by the fold before it to ensure geometry alignment. Current was supplied by an external power supply and controlled by a human operator. After folding, the lamp was attached to an external microcontroller (Uno R3, Arduino) that read and interpreted the sensor signals.

The lamp was used as a platform for testing the reliability and durability of the bistable switch. The switch was flipped on and off 350 times; It successfully completed the circuit

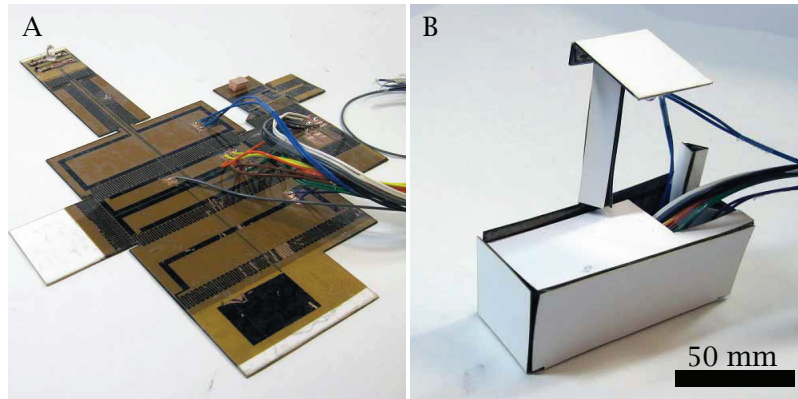


Figure 5.10: A functional self-folding lamp integrated the capacitive sensor and mechanical switch into a working device. A) The lamp in its flat state. B) The lamp after folding.

and turned on the lamp the first 156 consecutive times, and 335 times total. Failures in the switch were due to insufficient contact between the top and bottom copper layers, preventing the circuit from closing. The capacitive switch was also capable of turning the lamp on and off.

5.6 Discussion

The sensors presented here were all functional and compatible with our self-folding processes, and they could be combined or altered for other measurements as well. Multiple capacitive sensors could be arranged in a row to create a position or velocity sensor, or oriented in a grid for 2D positioning or to act as a keyboard. Two capacitive sensors could also be placed over one-another and allowed to slide, creating a continuous switch. The electromagnetic sensor can be wrapped around an axle and bearing to create a continuous rotation sensor, or it could act as a magnetic encoder by counting voltage peaks.

These sensors could be improved, particularly with regards to precision. The capacitive sensor's accuracy is approximately one newton. This could be improved with a softer dielectric layer, which would allow for a similar displacement with less force. The bistable switch worked well after folding, but began to fatigue after approximately 150 switches. This could be improved by optimizing the geometry and material selection. The switch is also limited by its size. It currently takes up an area of 12 cm^2 , and the minimum size for this switch is constrained by the length of the self-folding hinges, which must be over 10 mm long to ensure actuation, as well as the geometric measurements required to maintain stiffness and minimize fatigue. The velocity sensor was also less accurate than similar non-

printable sensors. This could be due to less precise fabrication or the low signal voltage. We expect that as self-folding techniques improve and functional materials become more advanced, laminate sensors will become a viable part of self-folding engineering.

There is plenty of room at the bottom.

Richard P. Feynman

6

Self-Folding at the Millimeter Scale

6.1 Introduction

So far in this dissertation, SMCs have only demonstrated a feature length range of 10 to 100 mm (Chapter 3). Not only does this limit the complexity of these machines, but it is also inappropriate for several applications. Many centimeter-scale devices are built using folding techniques, including robots [40] and medical tools [106], and the fabrication of these devices can be automated using self-folding to increase speed and precision. Some devices, such as microfluidic reactors [107] and biochips [108], require ‘ship-in-a-bottle’ geometries, in which one structure is embedded inside another. Self-folding can be used to assemble the internal structure when it is otherwise unreachable.

In this chapter we present an improved SMC capable of folding faces at length scales ranging from 0.5 to 40 mm. This is accomplished through thinner materials, new machining techniques, new adhesion layers, and additional structural layers to prevent delami-

nation. We begin by presenting our first attempt at miniaturizing the SMC, and show our design, fabrication process, and results. This version had insufficient precision and reliability, so we continue with an improved SMC that corrects for these deficiencies with a better fabrication process and more design options. The size reduction of the composite results in a more favorable torque-to-weight ratio, which allows us to experiment with new design parameters. We demonstrate simultaneous folding of an aluminum-based composite activated by a hot plate, and sequential folding of a composite based around a glass-reinforced epoxy (FR-4) and activated by internal resistive heating. We compare the minimum feature size and angular resolution of these designs and demonstrate their efficacy with a resistively heated model ship and a uniformly heated model bumblebee. Much of the content in this chapter is previously published [109] or will be [110].

6.2 First Generation

6.2.1 Composite Design

The miniaturized SMC consists of three different materials in seven layers. In the middle is a polymer flexural layer. On either side of the flexural layer is a sublamine consisting of an SMP layer sandwiched between two substrate layers. In our previous designs, the minimum feature size was limited by delamination of the SMP from the substrate (Section 3.3.5). To mitigate this, this composite includes two additional substrate layers on the outside of the SMP to prevent delamination. This has the added benefits of increasing stiffness and maintaining a uniform outer surface.

Actuated hinges in the laminate are created by cutting a gap with an arbitrary width in the two substrate layers on the concave side, and cutting a line in the substrate and SMP layers on the convex side (Figure 6.1A-B). Flexural hinges are created by cutting a gap in the substrate and SMP layers on both sides of the laminate, leaving only the flexural layer. The stiffness is adjusted by varying the length and gap width of the hinge.

This composite is activated by uniform heating in an oven instead of resistive heating. The CuPI used in our previous composites is too stiff for use at this scale, and we had not developed a technique for printing smaller circuits at the time of these experiments.

We chose to use the following materials in our composite: 50 μm aluminum (Al) as the substrate because of its high stiffness-to-weight ratio; 18 μm polyolefin (PO) as the SMP

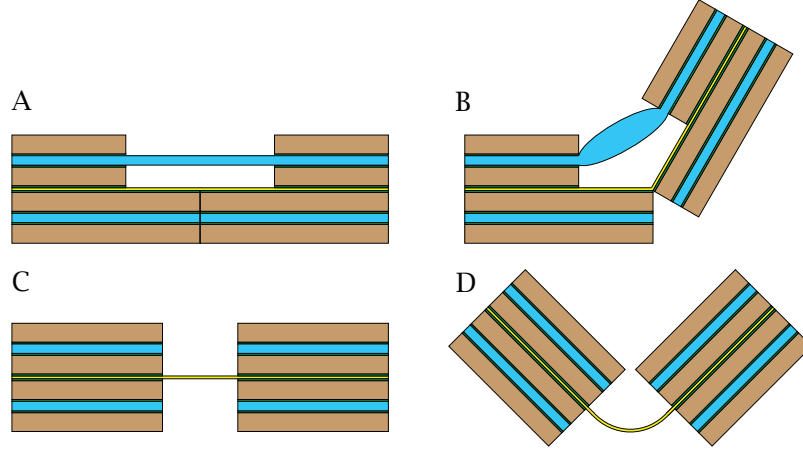


Figure 6.1: The self-folding composite consists of a stiff substrate (brown), a polyolefin SMP (blue), a flexural layer (yellow), and an adhesive (green). A diagram of a self-folding hinge is shown before (A) and after (B) activation. This composite is also capable of bidirectional flexure hinges (C-D) for dynamic mechanisms.

(different from the material used in Section 3.2) because it is non-toxic and commercially available as heat shrink wrap; and 2.5 μm polyester (PE) as the flexural layer because it is thin and flexible. A cyanoacrylate adhesive (CA) was used to bond each layer together. Therefore, the final laminate consists of two similar sublaminate composed of Al and PO (Al-CA-PO-CA-Al) on either side of a flexural layer (CA-PE-CA). More material information can be found in Appendix A.9.

6.2.2 Fabrication

Each self-folding laminate is assembled in five steps. First, each of four aluminum layers is machined with layer-specific features using a diode-pump solid-state laser (DC150H-355, Photonics Industries). A cyanoacrylate adhesive is spin coated onto each aluminum layer and these layers are bonded to either side of a sheet of prestretched PO, using pins to align the layer features. This results in a top and bottom composite, each comprising one PO and two aluminum layers. These composites are laser-machined again with additional features such as cuts through the PO layers. Adhesive is spin coated on each composite, and these are pin aligned and bonded to either side of a polyester thin film sheet. The full laminate is laser-machined to release the desired mechanism.

For example, in order to create a single 90° self-folding hinge, we first cut a 0.5 mm gap in two aluminum layers along the length of the hinge. We then spin coat adhesive on these two aluminum layers, lay a single layer of PO between them, align them with pins,

and bond them together. We also spin coat adhesive onto two uncut aluminum layers and bond them to either side of another layer of PO. After curing, we cut a single line into the second Al-PO-Al composite along the hinge. We then spin coat adhesive onto each Al-PO-Al composite and bond them to either side of a PE layer, aligning the two composites with pins. Finally, we cut the composite into its final outline, releasing the hinge.

6.2.3 Models and Results

Angle Control

The final angle of an actuated hinge is mechanically programmed into the laminate, similar to the method shown in Section 3.3.6. The final angle varies with the gap width w_g of the substrate on the concave side. The relationship between w_g , composite thickness t_c , and fold angle θ is shown in Equation (6.1) (Figure 6.2A).

$$\theta = 2 \arctan(w_g/t_c) \quad (6.1)$$

We built self-folding hinges with uniform face size and varying w_g to determine the relationship between w_g and θ . Each folding face was five millimeters long by five millimeters wide, with a gap width of 0.2 to 0.8 mm. We placed five samples for each set in an oven preheated to between 140 °C and 150 °C for 45 s in order to ensure complete folding. Figure 6.2B compares the experimental results with the predictive model. The data indicates

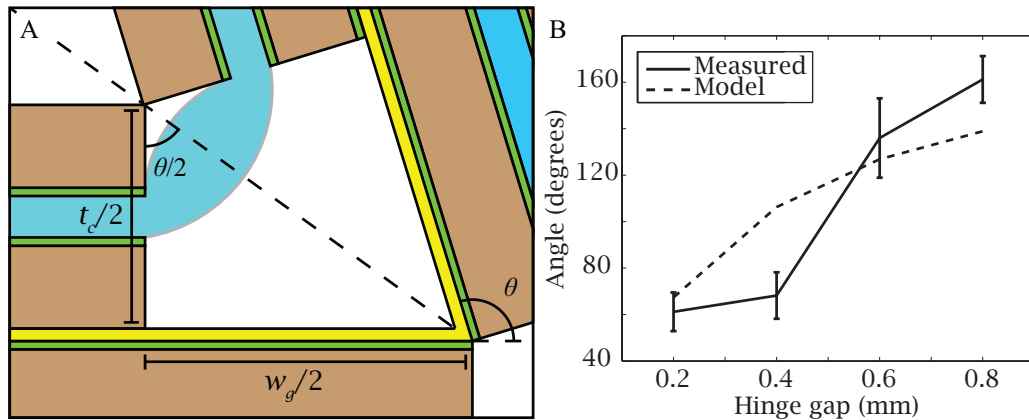


Figure 6.2: (A) A model for predicting final fold angle based on hinge geometry was developed based on the assumption that folding stopped when the two faces came into contact. The fold angle θ is dependent on the composite thickness t_c and the width of the gap w_g cut into the substrate. (B) The experimental data (solid) and model (dashed) relating w_g to θ . Error bars indicate the standard deviation, N=5.

a positive correlation between w_g and θ , but the folding is not precise.

Thermal Behavior

The time required to fold these composites is less than one minute because the composite can be rapidly heated. The time this takes in an oven can be predicted by assuming that conduction within the composite occurs more quickly than heat transfer into the composite and that conduction between the ceramic floor of the oven and the composite is greater than the heat flux due to convection and radiation. This allows us to use a lumped thermal model to express the energy transfer rate \dot{Q} as a function of the surface area A_s , time varying temperature T , and thermal contact conductivity h_o of the composite, as well as the constant temperature T_o of the oven. h_o was estimated to be from the calculations of Yovanovich et al. [111].

$$\dot{Q} = h_o A_s (T_o - T) \quad (6.2)$$

We can also express the temperature in terms of the initial temperature T_i , the total energy transfer Q , and the total heat capacity of the composite, which is dependent on the composite volume V , lump density ρ , and lump specific heat capacity c_p .

$$(T - T_i) = \frac{Q}{\rho V c_p} \quad (6.3)$$

Equations (6.2) and (6.3) can be combined into a differential equation, and the temperature can be solved explicitly as a function of time t . Here the area density $\rho_A = \rho V / A_s$.

$$\frac{\rho_A c_p}{h_o} \dot{T} = T_o - T \quad (6.4)$$

$$T = (T_i - T_o) \exp\left(-t \frac{h_o}{\rho_A c_p}\right) + T_o \quad (6.5)$$

The time required for the activation of self-folding is the time it takes for T to reach the glass transition temperature T_g of the composite, when folding is activated.

$$t = \frac{\rho_A c_p}{h_o} \log\left(\frac{T_i - T_o}{T_g - T_o}\right) \quad (6.6)$$

Here we assume that the composite's initial temperature T_i is the room temperature, 20 °C, the oven temperature T_o is 140 °C and the transition temperature T_g is 130 °C. Because of

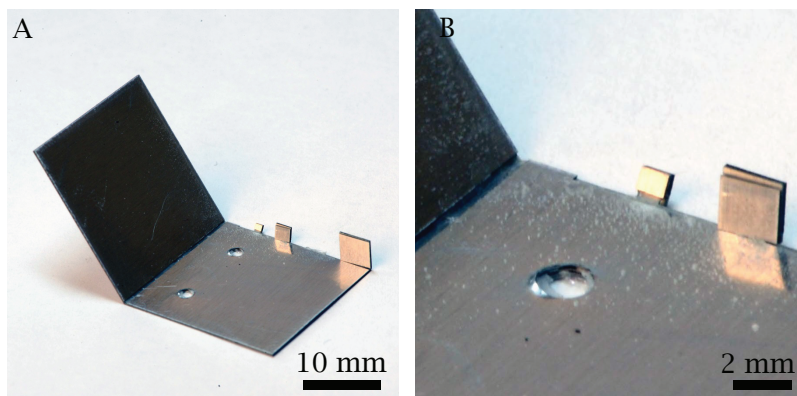


Figure 6.3: Self-folding hinges were built that were 1 mm, 2 mm, 3 mm, 4 mm, and 20 mm long in order to determine the minimum feature size this self-folding technique was capable of creating. All hinges successfully self-folded except the 3 mm hinge, which delaminated during the folding process. This indicates that the spatial resolution of this technique is at least 1 mm.

this, we expect folding to occur within five seconds of contact with the ceramic surface.

Minimum Feature Size

We built self-folding hinges with square faces that varied in size from 1 to 20 mm long. The 1 mm, 2 mm, 4 mm, and 20 mm faces all folded successfully (Figure 6.3). The 3 mm face failed to fold because the aluminum delaminated from the PO during folding, and was subsequently removed. This indicates that the composite can fold hinges as short as one millimeter, although it is not reliable at lengths shorter than five millimeters.

Sample Structures

We built a self-folding cube to demonstrate the ability of this method to produce structures (Figure 6.4). The unfolded composite was placed into an oven preheated to between 140 °C

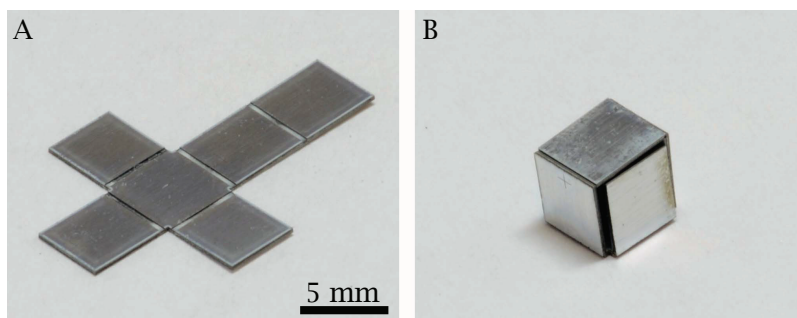


Figure 6.4: A five-millimeter self-folding cube before (A) and after (B) folding.

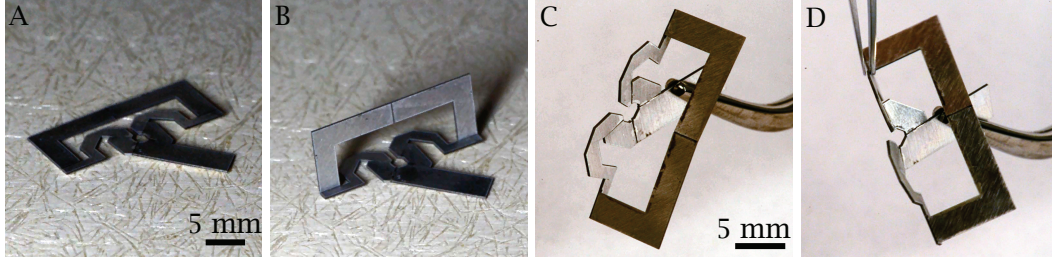


Figure 6.5: A spherical five-bar linkage before (A) and after (B) folding. (C) The mechanism in its resting state. (D) The mechanism transmitting motion from one linkage to another.

and 150 °C for 20 s, until folding was completed. The cube weighed 80 mg.

We fabricated a spherical five-bar linkage using this self-folding technique to demonstrate the ability to produce complex mechanisms (Figure 6.5). This linkage has two degrees of freedom and transforms two angular inputs into one or two decoupled angular outputs. This linkage is based on a similar one demonstrated by Sreetharan et al. [40] and is used in multiple microrobotic designs [41, 112]. The design requires five dynamic hinges to be arranged so that their coincident lines intersect at a single point. The unfolded version of this linkage was placed into an oven preheated to between 140 °C and 150 °C for 20 s, during which the out-of-plane component of the linkage folded into place. Afterwards, the ability of the linkage to transmit an angular displacement from one linkage to another was verified by applying a torque to one linkage with tweezers. After the torque was removed, the linkage returned to its resting state, indicating that the flexural hinges behaved elastically. The mechanism weighed 120 mg.

6.3 Second Generation

The previous composite was capable of hinges as short as one millimeter, but was not reliable or precise. In addition, we had only demonstrated simultaneous folding with uniform heating. These issues stemmed primarily from the adhesive used and the lack of resistive heaters. We developed a new millimeter-scale SMC to address these issues.

6.3.1 Composite Design

The second composite also consists of three different materials in seven layers. In the middle is the flexural layer, a 7.5 μm thick polyimide (PI) film. On either side of the flexural layer is a sublamine consisting of a 25 μm thick PO SMP sandwiched between two 50 μm

substrate layers. The layers are bonded together with 5 μm thick acrylic tape. More material information can be found in Appendix A.10. In this composite we can activate folding either by supplying heat from an external source, such as a hot plate, or by embedding resistive circuits along each hinge, similar to the bidirectional composite in Chapter 3.3.

The substrate can be any sufficiently stiff material. In our devices we use two different substrates: aluminum in the uniformly heated structures and FR-4 in the resistively heated structures; in both cases the substrate is 50 μm thick. Aluminum was chosen for the uniformly heated structures because of its high stiffness and high thermal conductivity (170 W/m-K). This enables the entire structure to maintain a uniform temperature even when parts of it lose contact with the hot plate, ensuring that folding continues over the entire structure. In contrast, FR-4 is used in the resistively heated structures because of its low thermal conductivity (0.4 W/m-K). When folding sequentially, insulation is necessary between adjacent folds to prevent the heat from one hinge from prematurely activating another.

In order to compare the thermodynamics between substrate materials, we developed a COMSOL thermal finite element model of two composites, one made with aluminum and one with FR-4. The simulation assumed each hinge was generating heat at a constant rate, and the PO temperature at the center was approximately 150 $^{\circ}\text{C}$ after 20 s. The temperature profile of the SMP layer in both situations is shown in Figure 6.6. In the aluminum substrate, the temperature five millimeters from the hinge only dropped to 145 $^{\circ}\text{C}$, while

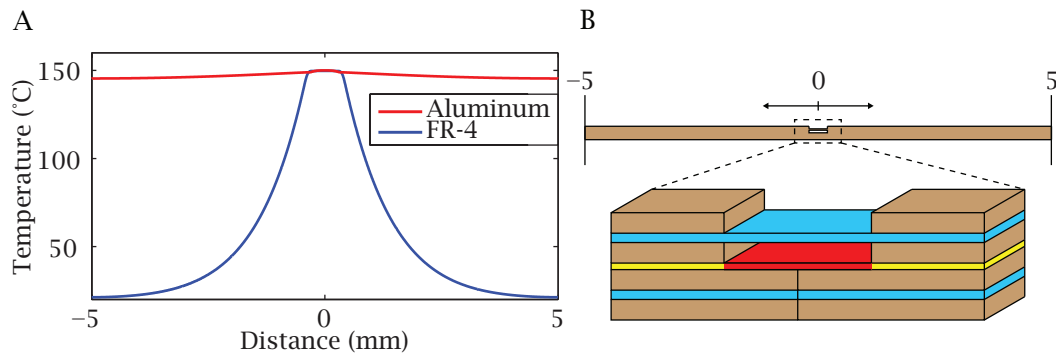


Figure 6.6: A thermal finite element model of the hinge was built in order to determine the temperature profile of the SMP when the hinge is internally heated to 150 $^{\circ}\text{C}$. (A) Hinge temperature as a function of distance from the hinge. The red line indicates the temperature profile of the PO when the substrate is aluminum, and the blue line is the temperature profile when the substrate is FR-4. (B) A diagram of the model hinge is shown at scale with the graph, and below that a section is blown up to illustrate the hinge geometry. In this figure, red indicates the volume of the hinge which is generating heat.

in the FR-4 substrate the same location is 21 °C. The transition of an SMP often occurs over a 30 °C range [72], so a difference of at least a 30 °C between hinges would be necessary in order to achieve sequential folds. This indicates that aluminum is not suited for sequential folding, but FR-4 is.

If the structure requires an embedded circuit, either for resistive heating or for its final function, a copper trace is included on the flexural layer. Copper is used in the devices presented here because it is flexible, easy to sputter coat, and has adequate resistivity for our trace geometry. The copper layer is approximately 200 nm thick; however, we found that our sputtering rate varies from 90 to 200 nm/min, so the trace thickness varied commensurately. In most hinges (and unless otherwise noted) the resistive portion of the trace is 800 μm wide and runs coincident to the midline of the hinge.

6.3.2 Fabrication

The composites are assembled in steps alternating between laser machining with a diode pump solid-state laser (DC150H-355, Photonics Industries) and bonding (Figure 6.7). First, the two top substrate layers (T1, T2) and bottom substrate layers (B1, B2) are prepared by applying the tape to both sides of two layers (T1, B1), and one side of the other two (T2, B2). The tape backing is left on the outer sides of the tape. The features exclusive to the

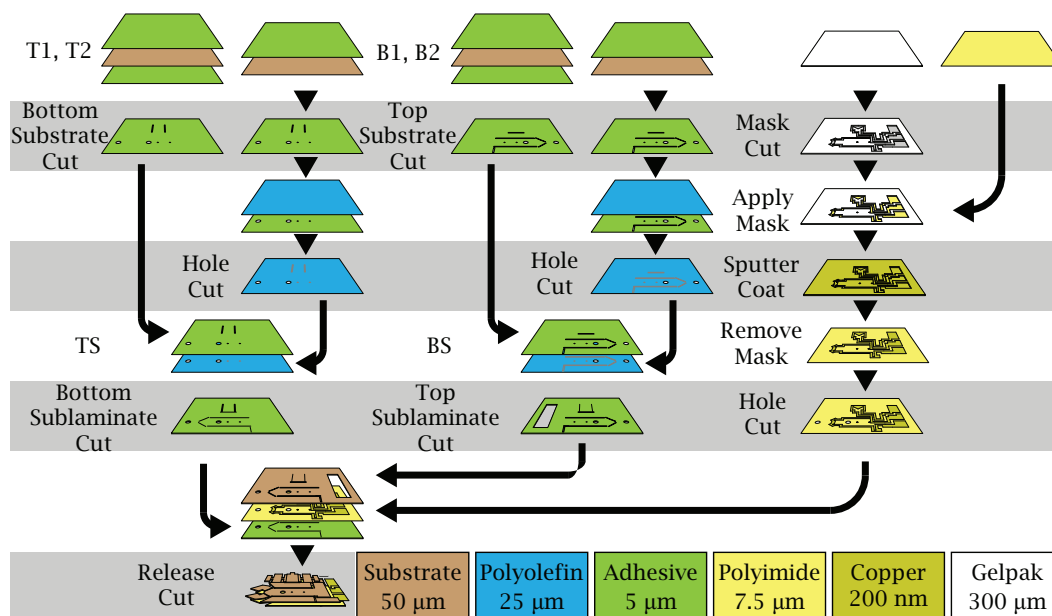


Figure 6.7: Fabrication occurs in sequential steps alternating between laser machining and bonding layers together.

substrate are then machined into the layers. This step uses two different cut patterns: one cut pattern for the substrate layers of the top sublaminate (T1, T2), and one for the layers of the bottom sublaminate (B1, B2). After machining, the PO layers are bonded to T2 and B2 and machined again to remove the PO at the alignment holes. Layers T1 and B1 are then pin-aligned and bonded to the other side of the PO, resulting in the top sublaminate (TS) and bottom sublaminate (BS). Each is machined with another cut pattern, removing material from both the substrate and PO layers. At this point there is adhesive on one side of the TS and BS sublaminate.

Making the flexural circuit layer requires four steps. First, the flexural thin film is rolled onto a piece of Gel-Pak (WF Film, Delphon Industries), which keeps it flat during handling. A mask made of Gel-Pak is cut with the circuit trace pattern and applied with pressure to the flexural layer. It is then sputter-coated with copper for a total of 110 s until the copper layer is approximately 200 nm thick, after which the mask is removed and alignment holes are machined in both the flexural layer and supporting Gel-Pak. If the flexural layer does not include a circuit, the thin film is still attached to the supporting Gel-Pak and machined, but is not masked or sputter-coated.

Once the flexural layer is prepared and the two sublaminate are machined, the TS sublaminate is pin-aligned and bonded to the exposed side of the flexural layer. The supporting Gel-Pak is then removed, and the BS sublaminate is aligned and bonded to the other side. The complete composite is then machined with the release cut pattern, resulting in the final planar structure. This structure is pressed with approximately 2.5 MPa for 45 minutes. For our resistively heated samples, the composite is secured to a glass slide with double-sided tape and the exposed traces are connected to copper pads with conductive epoxy (8331-14G, MG Chemicals).

6.3.3 Models and Results

Maximum Feature Size

The maximum face length is generally limited by the torque of the hinge, and we use a model similar to the one in Section 3.3.4 to predict the maximum face size a self-folding hinge can lift against gravity (Figure 6.8). This model assumes that the forces and mechanical behavior of the SMP are quasistatic, and that if the hinge begins to fold, it continues to fold to completion (Appendix C.3). Therefore, we are primarily interested in whether

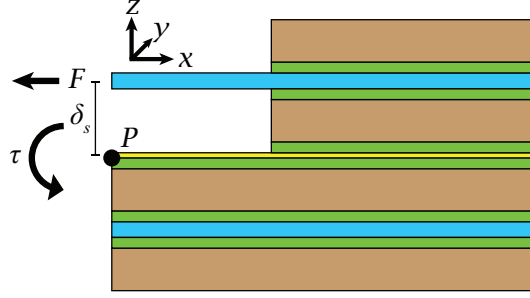


Figure 6.8: The hinge torque τ_s is caused by the force F due to the stress of the SMP while contracting, as well as the lever arm δ_s of the SMP layer from the point of rotation P , which is the intersection of the flexural layer and the hinge line.

the torque exerted by the SMP in the flat state is enough to overcome the torque due to gravity and start the folding motion.

The torque τ_s exerted by the SMP is a function of the contractile stress σ , the thickness t_s , the hinge length L_h and the distance δ_s of the SMP from the bending point. The moment due to gravity per meter hinge length τ_g is proportional to the mass m_f of the face and the distance d_f between the hinge and the center of mass of the face. These values are a function of the area density ρ_A , face length L_f , and shape of the folding face. Equations (6.7-6.11) solve for the maximum face length L_{max} that can be folded with our composite, assuming a rectangular face.

$$\tau_s = L_h t_p \sigma \delta_s \quad (6.7)$$

$$d_f = L_f / 2 \quad (6.8)$$

$$m_f = \rho_A L_f L_h \quad (6.9)$$

$$\tau_g = g m_f d_f \quad (6.10)$$

$$\begin{aligned} L_{max} &= L_f \big|_{\tau_g = \tau_s} \\ &= \sqrt{2 t_p \sigma \delta_s / g \rho_A} \end{aligned} \quad (6.11)$$

ρ_A is the sum of the density of each layer multiplied by its thickness. n is the total number of layers, and ρ_i and t_i are the density and thickness of the i^{th} layer, respectively. In our composite, ρ_A depends on t_p , the PO density ρ_s , the substrate thickness t_p and density ρ_p , the PI thickness t_h and density ρ_h , and the adhesive thickness t_d and density ρ_d . δ_s is the

distance between the SMP and the flexural layer.

$$\begin{aligned}\rho_A &= \sum_{i=1}^n \rho_i t_i \\ &= 4\rho_p t_p + 2\rho_s t_s + \rho_h t_h + 6\rho_d t_d\end{aligned}\tag{6.12}$$

$$\delta_s = t_p + t_s/2 + t_h/2 + 2t_d\tag{6.13}$$

The stress was measured to be 5.1 ± 0.3 MPa (Appendix C.2.3), and the maximum face lengths were calculated to be 65 mm for the FR-4 composites and 56 mm for the aluminum composites (Appendix C.1.3).

We built aluminum test hinges that were 30 mm wide and of varying lengths (30 mm, 40 mm, 50 mm, and 60 mm) to confirm our predictions. These hinges were activated on a hot plate (97042-574, VWR) set to 130 °C. The 30 mm and 40 mm long faces folded to completion in approximately 15 s, judged by observing a fold of more than 90°, at which point gravity no longer limits the fold angle. The 50 mm and 60 mm long faces took approximately two minutes to stop moving, and neither folded to completion. The 50 mm face stopped at approximately 46°, and the 60 mm face stopped at approximately 32°. These results underperform our model, which predicted a maximum face length of 56 mm. We believe that this could be due to two factors. Our model ignores the viscoelasticity of the PO in its rubbery state, but the stress relaxation could be a significant part of the material behavior at higher loads. The other possibility is that the higher loads caused the layers in the hinge to delaminate, changing the hinge geometry and blocking folding.

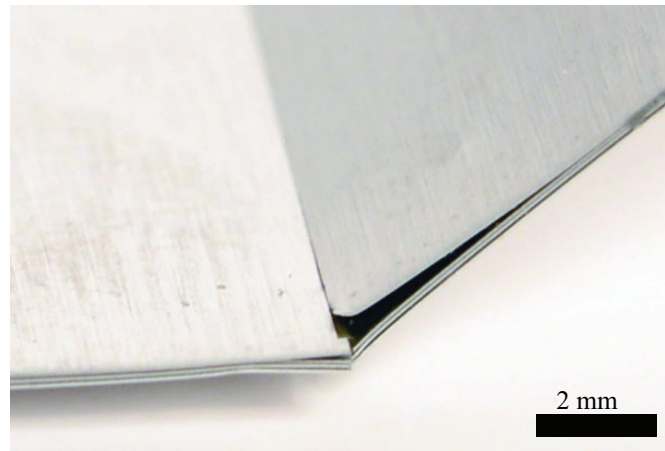


Figure 6.9: The self-folding hinge after folding a 50 mm long face. The layers of the composite partially delaminate when folding large hinge faces, which may stop folding prematurely.

In the 50 mm and 60 mm samples we can see signs of delamination, as well as contact between the two folding faces, suggesting that folding stopped when the two sides collided (Figure 6.9).

Minimum Feature Size

The minimum face size is governed by fabrication precision and adhesion between layers, and was determined experimentally. We built experimental hinges with square faces of variable lengths. We first built uniformly heated hinges with an aluminum substrate and faces varying from 0.5 to 3 mm mm long on a single sample (Figure 6.10A). Each hinge had a 400 μm gap width. The completed sample was placed on a hot plate set to 130 °C and left to fold for approximately one minute. These faces all folded successfully. However, there was a noticeable trend that larger faces folded to greater angles. We built resistor-heated hinges with FR-4 and faces from one to three millimeters long (Figure 6.10B). Smaller faces were not possible because the size of the trace and separating gaps were too fine for our masking process. Because of the small size, the resistive traces were 400 μm wide. These faces also folded successfully when supplied with 100 mA of current (using a 1666 BK Precision power supply). However, they showed greater individual variation in final fold angle. This is likely due to the differences in heat profiles at each hinge; different sized hinges have different edge effects where the traces enter and leave the hinge line. In this case, the smaller faces folded at a lower current than the larger faces. When the current was increased to activate the larger faces, the increased heat led to some deformation in the smaller faces.

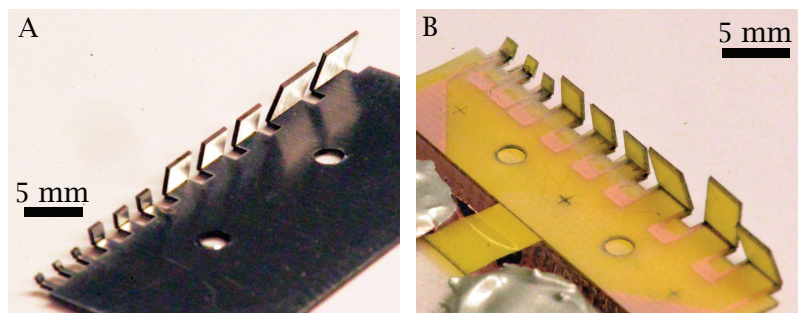


Figure 6.10: Experimental pieces were built with square faces of variable length to determine the minimum feature size that could be self-folded. (A) A composite with an aluminum substrate was activated by uniform heating from a hot plate, and folded faces from 0.5 to 3 mm in length. (B) A composite with an FR-4 substrate was activated through resistive heating, and successfully folded faces one to three millimeters in length.

Angle Control

We used the model from Section 6.2.3 to predict θ based on w_g (Equation 6.1), and built experimental hinges consisting of square faces five millimeters long, attached to a stationary base face. These hinges had gap widths of 0.1, 0.2, 0.4, 0.6, 1.2, and 1.8 mm wide. They were supplied with 180 to 250 mA of current for 20 to 60 s, until folding was completed. This variation is due to the variable resistivity of the heating trace.

The measured fold angles can be seen in Figure 6.11 as a function of w_g , along with the analytical model. The model overestimates the final fold angle; we believe this may be due to the substrate increasing in thickness as the SMP contracts and thickens. A thicker composite results in the two faces coming into contact sooner and stopping the folding process prematurely.

We created more experimental hinges with the same geometries and 0.4 mm gap widths. One of these pieces was made with aluminum, and the other was made with an FR-4 substrate, but without the copper traces. Both were uniformly heated on a hot plate set to 130 °C for approximately 15 s. The uniformly heated FR-4 hinges folded to a final angle of 82° with a standard deviation of 1°. This demonstrated more precision than the resistively heated hinges with the same gap width, which had a mean final angle of 90° with a standard deviation of 6°. The aluminum hinges folded to a mean final angle of 122° with a standard deviation of 5°. This increase in angle may be due to the increased rigidity of the aluminum, which would better constrain the PO. Constraining the PO would prevent it from thickening, which in turn would keep t_c from increasing and θ from decreasing.

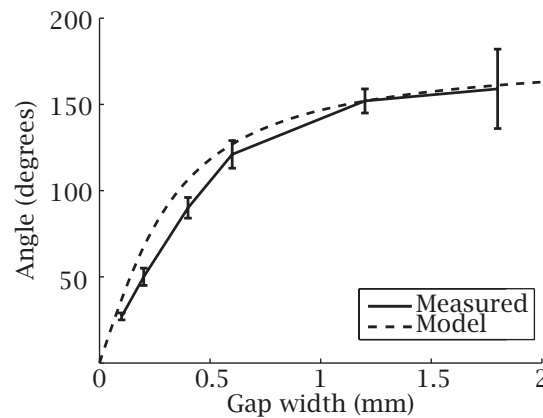


Figure 6.11: The fold angle was measured as a function of gap width (solid line, $N=8$, error bars indicate standard deviation). These results were compared to an analytical model (dashed line) shown in Equation (6.1).

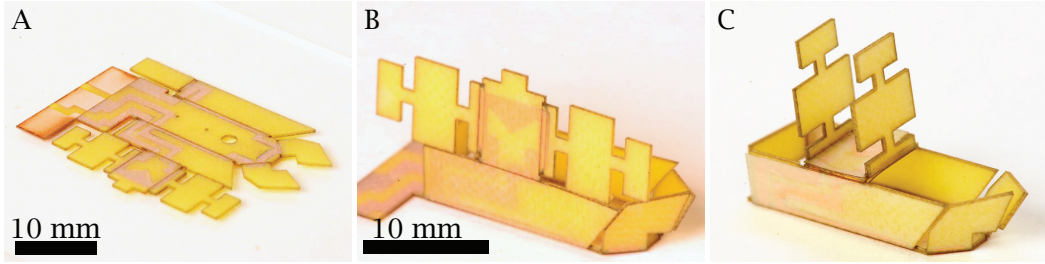


Figure 6.12: (A) The flat composite programmed to fold into a ship-like structure. (B) The ship after the hull is folded in the first folding step. (C) The ship after the sails are folded in the second folding step.

The standard deviation of the aluminum hinges was less than the standard deviation of the resistively heated hinges with a similar mean fold angle; the resistive hinges with a 0.6 mm gap folded to an angle of $121^{\circ} \pm 8^{\circ}$.

Demonstration Structure: Ship

We designed a structure resembling a miniature ship to demonstrate the possible complexity of a structure folded sequentially via resistive heating (Figure 6.12). This structure assembled through two sequential folding steps. The first folds created the hull of the ship and were activated with 220 mA of current. The second set raised the sails and was activated with 160 mA. Each step took approximately 20 s. We believe the difference in activating currents may be related to differing thermal profiles in the hinges. The hinges ranged in length from 3 to 13 mm in length, and included both mountain and valley folds.

Demonstration Structure: Bumblebee

We designed and built a structure that resembled a bumblebee to demonstrate that uniform folding could produce static structures and dynamic mechanisms (Figure 6.13). The

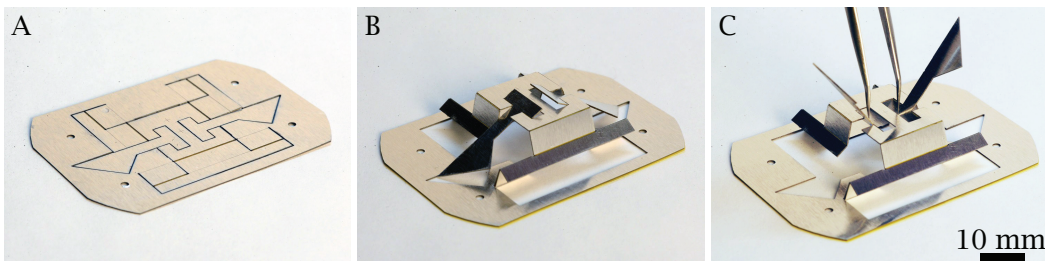


Figure 6.13: (A) The flat composite programmed to fold into a bumblebee-like structure. (B) The bumblebee after folding. (C) The bumblebee with its wings raised.

bumblebee assembled during a single folding step that was activated by a hot plate set to 130 °C. Assembly took eight seconds. This structure includes a self-folding Sarrus linkage which comprises the 'body' of the bee, and wings that are attached to the body via flexural hinges. The wings can be actuated by pushing on tabs in the body of the bee. The Sarrus linkage is a single degree-of-freedom mechanism which allows two surfaces to move towards or away from each other while constraining them to remain parallel. This linkage is particularly significant because it forms the basis around which Pop-Up Book MEMS [40, 77] devices are designed, indicating that the self-folding technique presented here is compatible with Pop-Up Book MEMS and could be used to actuate the assembly process. The self-folding hinges ranged in length from 8 to 15 mm in length, and included both mountain and valley folds. The flexural hinges were each three millimeters long.

6.4 Discussion

This self-folding technique is appropriate for features from 0.5 to 40 mm long and is compatible with different materials and activation methods. Previous electrically activated hinges demonstrated an average standard deviation of 6° for hinges folded up to 120° (Section 3.3.6), while this new composite exhibited an average standard deviation of 5° for hinges across the same range. It is also capable of achieving a maximum fold angle of 159°, in comparison to a maximum angle of 118° for the previous design (Section 3.3.6).

This composite is also capable of greater complexity than our earlier composites. If the maximum face length indicates the largest structure we can fold, and the minimum face length indicates the smallest feature we can make, then the ratio between the maximum and minimum lengths indicates how many features we can fit in a single device, or the complexity of the device. The complexity ratio of our earlier paper based composite was $(100\text{ mm})/(10\text{ mm}) = 10$, while the complexity ratio for the aluminum-based composite in this chapter is $(40\text{ mm})/(0.5\text{ mm}) = 80$.

Despite the high fabrication precision required, this is a relatively inexpensive and fast process. For uniformly activated hinges, the only significant piece of equipment needed is a laser cutter with an appropriate resolution. For mass production, the cutting step could be replaced with stamping. Resistively activated hinges also require a means to fabricate the trace, but this was performed without a cleanroom or any hazardous materials.

Our results indicate that geometry is not sufficient for predicting hinge behavior. Alu-

minum hinges exhibit greater fold angles than FR-4 hinges with similar gap widths, which we believe is due to their greater stiffness. In addition, uniformly heated hinges demonstrate greater precision and smaller faces than equivalent resistively heated hinges. This variability may be due to their thermal behavior. These hinges have variable temperature profiles depending on their trace geometry, hinge size, and sputtering process. When this issue is combined with the heat sensitivity of the composite, it can result in delamination and inaccurate fold angles. For instance, the PO used in these experiments has a nominal transition temperature of 130 °C, yet the adhesive has a nominal maximum operating temperature of 150 °C, resulting in a narrow operational range for the composite. If the current is too low, some faces might not fold completely, and if it is too high, other faces might delaminate. When faces delaminate, the joint stops programmed into the composite via gap width are no longer reliable. Unfortunately, the thermodynamics of these anisotropic systems are difficult to predict. During our experiments the appropriate current for each sample was determined experimentally.

This issue could be corrected by selecting new materials with different thermal properties, or by adjusting individual features of each hinge, such as the supplied current or the trace width. These adjustments would benefit from a thorough characterization of the SMP, the thermodynamics, and the hinge behavior. The uniformly heated hinges were more precise, but there was still angular variation depending on the hinge length, which also warrants further investigation.

It is worth noting that the minimum folded feature length (0.5 mm) is close to the thickness of the composite (0.3 mm). To increase feature resolution, we could combine self-folding with other micromachining techniques. These techniques generally involve etching features into a flat material, so they can only produce features as tall as the thickness of the raw material. In the case of our composite, these techniques could be used to machine features into the surface of the composite up to 0.3 mm in height, while features greater than 0.5 mm could be self-folded. Only features with heights between 0.3 and 0.5 mm would be unmachineable by either method.

We used popupCAD to design the bumblebee; this has demonstrated the potential of folding-focused computer design tools to speed up our prototyping process. Further work could automate the generation of sequential folding steps, trace patterns, and the control system to supply the necessary currents. We are also interested in integrating electromechanical components such as actuators and sensors into our self-folded mechanisms to

produce autonomously folding machines. Finally, while we have studied the geometric capabilities of this technique, further work must be done to determine its mechanical properties. For example, the self-folding hinges, while nominally static after cooling, are actually noticeably compliant.

By scaling shape memory composites down, integrating new materials, and demonstrating pop-up style folding, these results represent a link between self-folding techniques and fold-based mesoscale manufacturing.

There are no facts about the future.

Thomas Wilson

7

Future Work and Conclusion

7.1 Introduction

The work in this dissertation has demonstrated that functional and complex structures can self-fold at a range of sizes. However, there are still substantial limitations to this technique. The majority of our research was motivated by the idea of printable manufacturing, so we worked to make our self-folding fast and inexpensive. This is why, for example, the majority of our results are paper-based and we focused on a laminate approach instead of discrete components. However, some of our work has been motivated by the applications for self-folding to increase functionality. Autonomous folding, for example, has limited applications in terms of manufacturing, but is valuable for applications like space exploration or search and rescue. By accommodating both of these goals, we have ignored opportunities to develop features that would aid one problem at the expense of another. In this chapter we discuss possible improvements for shape memory compos-

ites, alternative methods for functional self-folding, and new folded components that are both within and adjacent to our vision of printable self-folding machines.

7.2 Improving Shape Memory Composites

We dealt with many restrictions when designing our shape memory composites. One of the strictest limitations we faced was our choice of SMP. For larger scale folding, the only suitable material available to us was prestretched PS, sold commercially as a child’s toy known as Shrinky-Dinks. Most other commercially available SMPs are too thin, too soft, or do not contract bidirectionally. Relying on a single SMP has led to several limitations in our design space. First, contractile stress and SMP thickness are two of the three significant factors in hinge torque, which in turn limits a structure’s size and geometry (Chapter 3). Because these parameters were fixed by our material, the size and complexity of our designs was constrained. In addition, the shrink ratio limits the maximum possible fold angle. Fortunately, a variety of SMPs have been developed [113–116], and future self-folding composites could use this work to customize an SMP for a specific application. There are a variety of ways to alter SMP material properties, such as increasing stiffness, increasing crosslink density, or adding fillers to the polymer matrix [117]. Table 7.1 displays some representative SMPs, along with their maximum measured contractile stress and recoverable strain (100% strain is equivalent to a 2-to-1 shrink ratio). There are several SMPs with substantially higher shrink ratios and contractile stresses, and these could be integrated into an SMC for better performance.

Another aspect of our technique that needs improvement is angular precision. Our current method results in errors of approximately 5°, likely because paper is easily deformable and our adhesive delaminates slightly at the edges so that opposite faces are not aligned. One way to improve fold precision is to use more precise machining methods and more intricate features. Stiffer substrates and stronger adhesives would prevent deformations,

Table 7.1: Material properties of experimental shape memory polymers.

Material	Contractile stress (MPa)	Recoverable strain
Polystyrene (PS)	0.7	100%
Polyurethane [113]	2.8	75%
Polyurethane with nanoclay particles [114]	4.9	90%
Epoxy Resin with SiC particles [115]	6	35%
Acrylate with Xini [116]	4	600%

which lead to unpredictable folds. Automated alignment and lamination would increase the precision of hinge geometries.

Another method is to integrate sensors into each hinge and introduce a control system for the folding process. Electrically activated SMCs already contain most of the necessary components: there is an existing embedded circuit board, we have demonstrated that the folding stimulus (electric current) can be controlled and gated with a MOSFET, and the resistive heating circuit can double as a temperature sensor by measuring resistance change. The angle of a hinge can be measured with encoders [103, 118], strain gauges [119], or gyroscopes [120], and controlled self-folding in non-printable applications has already been demonstrated using soft strain sensors [121]. Many of these methods would require installation of discrete components, which would make the entire process more expensive, more time consuming, and less printable. However, strain gauges can be printed with conductive inks [122], and so could be integrated into a printable process.

7.3 Alternative Self-Folding Methods

SMCs have some intrinsic limitations which would be difficult to overcome. Polymers are generally soft, especially in their rubber phase, so there's a limit to how much torque could be produced even with tailored materials. In addition, the shape change in the SMP is not reversible, so SMCs are not suited for certain applications. Fortunately, a variety of other self-folding methods exist, and some of these could be adapted for functional machines.

7.3.1 Pneumatics

Pneumatic pouches have been used as limited-range rotary actuators, and if attached to two flat faces, can cause them to fold [123]. Pouch motors are notable in particular as a printable method for actuation and self-folding [60, 124]. These motors are made when two sheets of PVC are selectively bonded into pouches with arbitrary shapes. This process allows for rapid fabrication without investing in customized tools.

Pneumatic hinges have two distinct advantages over SMCs. First, they are repeatable. This allows for new applications, such as structures that must fold and unfold multiple times. It also makes them more precise, since any control scheme used to govern the folding process can correct for overfolding. The second advantage is substantially higher folding torque. The torque is governed by the pressure in the pouch, which is only limited

by the material and seal of the pouch. Pouch motors have demonstrated torques as high as 100 mN m at a pressure of 10 kPa, and the data indicates a linear relationship between torque and pressure [60]. Similar actuators have withstood pressures of over 100 kPa, so we expect that pneumatic hinges could reasonably produce at least 1 N m of torque [125].

7.3.2 Shape Memory Alloys

Shape Memory Alloys (SMAs) are similar to SMPs in that they undergo a phase change at a specific temperature, and this can lead to a preprogrammed shape change. There are some key differences however. SMAs can usually be activated repeatably, and have been used as actuators in robots [66] and other systems [126]. They can exhibit contractile stresses of up to 500 MPa, but have maximum recovery strains of only 1% to 8% [127]. SMAs have already been used for some self-folding applications, but in many cases the fold had to first be mechanically programmed into the SMA [56]. Making each hinge was time consuming, and the hinges and faces were discrete parts that had to be assembled, so it was not a printable process.

An alternative method would be to create a laminate consisting of one or more layers of active SMA and one passive substrate. A thin bimorph actuator can achieve large displacements with small material strains [54, 128]. The SMA layer can be programmed through local annealing [126] to produce both active and passive sections, resulting rigid faces and active hinges.

7.3.3 3D Printing

In this dissertation we have often treated folding as an alternative to 3D printing. However, it is possible to 3D print sheets which are then folded into more complex structures [129], harnessing the two fabrication techniques in succession. Batteries, actuators, and high-resolution features could be 3D printed and folding could be used to make the larger structures efficiently. Previous examples of 3D printed origami have been folded manually [129] or actuated with polymer swelling [130]. It is unclear whether mechanically preprogrammed materials like SMPs and SMAs could be utilized in the 3D printing process, but other techniques, such as utilizing gravity along with selective softening [131], could be appropriate for many applications.

7.4 Components

One noticeable limitation in the self-folding crawling robot is the bulky discrete components on top of the composite. Electric motors are effectively the default actuation method for robotic systems, but only exist in 3D geometries. Sensors come in a larger variety of designs, but many of these rely on 3D features as well. There are many examples of flat actuators and sensors, in particular in microelectromechanical system (MEMS) devices, but further work is necessary to harness their full potential in a system that transforms from flat to 3D.

7.4.1 Printable Sensors

There are many examples of printable sensors beyond those we presented in Chapter 5. A variety of conductive inks can be used to sense strain and pressure, and these have been fabricated with inkjet [132] and 3D printers [49]. MEMS sensors generally consist of 2D geometries and can sense many mechanical effects including force [133] and acceleration [134]. Some of these designs can be scaled and integrated directly into our folded machines. For example, conductive surfaces can be embedded in larger folded structures to measure macroscale deformations and forces [135].

We predict it will be more challenging to design non-mechanical sensors into self-folding laminates. Optical [136] and chemical [137] sensors, for example, require special materials and fabrication processes, which may be incompatible with a generic and inexpensive printable process. However, many of these sensors can be manufactured with a sub-100 μm thickness, and so could be set inside a via in the substrate without increasing the thickness of the SMP.

7.4.2 Printable Actuators

In order to build truly flat self-folding machines, methods for folding and coupling actuators will need to be developed. Many flat actuators already exist, such as piezoelectric actuators [138], dielectric elastomers [139], and pneumatic pouch motors [60]. SMA wires are also suitable [66], and Chen et al. have even developed a paper-based electrostatic actuator specifically for printable robots [140]. Each of these actuators has strengths and weaknesses, but they all produce an oscillating motion, which can be a limitation when compared to rotary motors. Many machines use a cyclic actuation to produce a continu-

ous or asymmetric motion, such as a wheel-driven robot [141] or a walking linkage with a single degree of freedom [142].

An oscillating input cannot achieve these motions directly, but this limitation has been overcome in a variety of ways. Centimeter-scale walking robots can create a walking gait with two piezoelectric actuators and a five-bar linkage mechanism [41]. asymmetric friction can be used to transform linear motion into rotary motion through a stick-slip drive [143], and asymmetric geometry such as a ratchet can be used to extract rotary motion from linear forces [144].

In many of these situations, the most challenging part of the self-folding process will be coupling the motor to the transmission. Linkages are an effective method for getting arbitrary motions from the input of an actuator, and these mechanisms create a structural loop consisting of the linkages, the mechanical ground of the machine, and the actuator. In many situations, before self-folding, the actuator will only be attached to the ground layer, and must be joined to the transmission during the folding process. In the crawling robot, this joining was accomplished with alignment and locking tabs, but these required precise folds and were not robust. At this point we don't believe there is a single best practice for designing this coupling system, but instead it must be designed on a case-by-case basis.

An alternative actuator schema is to have the actuator be the only connection between two independent components, such as a car wheel to its axle. In this case, either the two structures must be installed in sequence, or an actuator layer must be integrated into the self-folding laminate.

7.5 Conclusion

We have successfully demonstrated that self-folding can be applied to complex and functional machines. This includes demonstrations of several composites for different applications, controlled fold angles, predictable thermal and mechanical behavior, and the integration of folded sensors and linkage mechanisms at a range of sizes. However, the majority of all possible machine designs are still beyond our capabilities. Our experiments have demonstrated the size, weight, complexity, and spatial resolution all depend on the self-folding technique and materials, and these parameters define the design space. Future work can address these challenges by building on the substantial existing research in materials science and computational geometry.

Bibliography

- [1] R. J. Lang, *Origami Design Secrets: Mathematical Methods for an Ancient Art, Second Edition*. CRC Press, 2011.
- [2] J. Montroll, *Origami and Math: Simple to Complex*. Dover Press, 2012.
- [3] J. Rutzky, *Kirigami: Exquisite Projects to Fold and Cut*. Sterling Innovation, 2007.
- [4] P. Jackson, *The Pop-Up Book: Step-by-Step Instructions for Creating Over 100 Original Paper Projects*. Macmillan, 1993.
- [5] C. Barton, *The Pocket Paper Engineer: How to Make Pop-Ups Step-by-Step*. Popular Kinetics Press, 2008.
- [6] E. D. Demaine and J. O'Rourke, *Geometric Folding Algorithms: Linkages, Origami, Polyhedra*. Cambridge University Press, 2007.
- [7] E. D. Demaine, M. L. Demaine, and J. S. B. Mitchell, "Folding flat silhouettes and wrapping polyhedral packages: New results in computational origami," *Computational Geometry*, vol. 16, no. 1, pp. 3-21, 2000.
- [8] T. Tachi, "Origamizing polyhedral surfaces," *Visualization and Computer Graphics, IEEE Transactions on*, vol. 16, no. 2, pp. 298-311, 2010.
- [9] E. D. Demaine and T. Tachi, "Origamizer: A practical algorithm for folding any polyhedron," 2015.
- [10] N. M. Benbernou, E. D. Demaine, M. L. Demaine, and A. Ovadya, "Universal hinge patterns to fold orthogonal shapes," in *Proc. Fifth International Meeting of Origami Science, Mathematics, and Education*, 2011, pp. 405-21.
- [11] Z. Abel, E. D. Demaine, M. L. Demaine, S. Eisenstat, A. Lubiw, A. Schulz, D. L. Souvaine, G. Viglietta, and A. Winslow, "Algorithms for designing pop-up cards," in *30th International Symposium on Theoretical Aspects of Computer Science (STACS 2013)*, vol. 20, 2013, pp. 269-280.
- [12] M. Kapovich and J. J. Millson, "Universality theorems for configuration spaces of planar linkages," *Topology*, vol. 41, no. 6, pp. 1051-1107, 2002.
- [13] T. G. Abbott, "Generalizations of Kempe's universality theorem," Master's thesis, Massachusetts Institute of Technology, 2008.

- [14] S. Coros, B. Thomaszewski, G. Noris, S. Sueda, M. Forberg, R. W. Sumner, W. Matusik, and B. Bickel, "Computational design of mechanical characters," *ACM Transactions on Graphics (TOG)*, vol. 32, no. 4, p. 83, 2013.
- [15] A. Lehninger, D. Nelson, and M. Cox, *Principles of Biochemistry*. W.H. Freeman and Company, 2005.
- [16] I. Luque, S. A. Leavitt, and E. Freire, "The linkage between protein folding and functional cooperativity: two sides of the same coin?" *Annual Review of Biophysics and Biomolecular Structure*, vol. 31, no. 1, pp. 235-256, 2002.
- [17] S. Yang and B. Roux, "Src kinase conformational activation: thermodynamics, pathways, and mechanisms," *PLoS Computational Biology*, vol. 4, no. 3, p. e1000047, 2008.
- [18] E. M. Moody, J. T. Lecomte, and P. C. Bevilacqua, "Linkage between proton binding and folding in RNA: A thermodynamic framework and its experimental application for investigating pKa shifting," *RNA*, vol. 11, no. 2, pp. 157-172, 2005.
- [19] T. Eisner, "Leaf folding in a sensitive plant: A defensive thorn-exposure mechanism?" *Proceedings of the National Academy of Sciences*, vol. 78, no. 1, pp. 402-404, 1981.
- [20] P. Todd, "A geometric model for the cortical folding pattern of simple folded brains," *Journal of Theoretical Biology*, vol. 97, no. 3, pp. 529-538, 1982.
- [21] H. Gray, *Anatomy of the Human Body*. Lea & Febiger, 1918.
- [22] A. Vander, J. Sherman, and D. Luciano, *Human Physiology: The Mechanisms of Body Function*. 1998. WCB McGraw-Hill International Ed, New York, 1998.
- [23] H. Kobayashi, B. Kresling, and J. F. Vincent, "The geometry of unfolding tree leaves," *Proceedings of the Royal Society of London. Series B: Biological Sciences*, vol. 265, no. 1391, pp. 147-154, 1998.
- [24] F. Haas, S. Gorb, and R. Wootton, "Elastic joints in dermapteran hind wings: materials and wing folding," *Arthropod Structure & Development*, vol. 29, no. 2, pp. 137-146, 2000.
- [25] F. Haas and R. G. Beutel, "Wing folding and the functional morphology of the wing base in coleoptera," *Zoology*, vol. 104, no. 2, pp. 123-141, 2001.
- [26] S. Heimbs, S. Kilchert, S. Fischer, M. Klaus, E. Baranger, *et al.*, "Sandwich structures with folded core: mechanical modeling and impact simulations," in *SAMPE Europe International Conference, Paris*, 2009, pp. 324-31.
- [27] R. Konings and R. Thijs, "Foldable containers: a new perspective on reducing container-repositioning costs," *European Journal of Transport and Infrastructure Research*, vol. 1, no. 4, pp. 333-352, 2001.
- [28] K. Miura, "Method of packaging and deployment of large membranes in space," *The Institute of Space and Astronautical Science report*, vol. 618, pp. 1-9, 1985.

- [29] S. A. Zirbel, R. J. Lang, M. W. Thomson, D. A. Sigel, P. E. Walkemeyer, B. P. Trease, S. P. Magleby, and L. L. Howell, "Accommodating thickness in origami-based deployable arrays," *Journal of Mechanical Design*, vol. 135, no. 11, p. 111005, 2013.
- [30] A. S. Verge, "Rapidly deployable structures in collective protection systems," Defense Technical Information Center, Tech. Rep., 2006.
- [31] J. M. Mejia-Ariza, T. W. Murphey, and E. L. Pollard, "Manufacture and experimental analysis of a concentrated strain based deployable truss structure," Defense Technical Information Center, Tech. Rep., 2006.
- [32] D. J. Sentinella, "US Army engineer support to expeditionary warfare," Defense Technical Information Center, Tech. Rep., 2004.
- [33] D.-Y. Lee, G.-P. Jung, M.-K. Sin, S.-H. Ahn, and K.-J. Cho, "Deformable wheel robot based on origami structure," in *Robotics and Automation (ICRA), 2013 IEEE International Conference on*. IEEE, 2013, pp. 5612–5617.
- [34] S. M. Felton, D.-Y. Lee, K.-J. Cho, and R. J. Wood, "A passive, origami-inspired, continuously variable transmission," in *Robotics and Automation (ICRA), 2014 IEEE International Conference on*. IEEE, 2014, pp. 2913–2918.
- [35] H. Okuzaki, T. Saïdo, H. Suzuki, Y. Hara, and H. Yan, "A biomorphic origami actuator fabricated by folding a conducting paper," in *Journal of Physics: Conference Series*, vol. 127. IOP Publishing, 2008, p. 012001.
- [36] C. Sung and D. Rus, "Foldable joints for foldable robots," *Journal of Mechanisms and Robotics*, vol. 14, no. 1193, p. 1, 2015.
- [37] L. L. Howell and A. Midha, "A method for the design of compliant mechanisms with small-length flexural pivots," *Journal of Mechanical Design*, vol. 116, no. 1, pp. 280–290, 1994.
- [38] B. P. Trease, Y.-M. Moon, and S. Kota, "Design of large-displacement compliant joints," *Journal of Mechanical Design*, vol. 127, no. 4, pp. 788–798, 2005.
- [39] P. S. Gollnick, S. P. Magleby, and L. L. Howell, "An introduction to multilayer lamina emergent mechanisms," *Journal of Mechanical Design*, vol. 133, p. 081006, 2011.
- [40] P. S. Sreetharan, J. P. Whitney, M. D. Strauss, and R. J. Wood, "Monolithic fabrication of millimeter-scale machines," *Journal of Micromechanics and Microengineering*, vol. 22, no. 5, p. 055027, 2012.
- [41] A. T. Baisch and R. J. Wood, "Pop-up assembly of a quadrupedal ambulatory micro-robot," in *Intelligent Robots and Systems (IROS), 2013 IEEE/RSJ International Conference on*. IEEE, 2013, pp. 1518–1524.
- [42] K. L. Hoffman and R. J. Wood, "Myriapod-like ambulation of a segmented micro-robot," *Autonomous Robots*, vol. 31, no. 1, pp. 103–114, 2011.

- [43] M. Agheli, S. G. Faal, F. Chen, H. Gong, and C. D. Onal, "Design and fabrication of a foldable hexapod robot towards experimental swarm applications," in *Robotics and Automation (ICRA), 2014 IEEE International Conference on*. IEEE, 2014, pp. 2971-2976.
- [44] C. D. Onal, M. T. Tolley, D. Rus, and R. J. Wood, "Origami-inspired printed robots," *Mechatronics, IEEE/ASME Transactions on*, vol. to be published, 2015.
- [45] J. Cybulski, J. Clements, and M. Prakash, "Foldscope: Origami-based paper microscope," *PloS One*, vol. 9, no. 6, p. e98781, 2014.
- [46] D. M. Aukes, B. Goldberg, M. R. Cutkosky, and R. J. Wood, "An analytic framework for developing inherently-manufacturable pop-up laminate devices," *Smart Materials and Structures*, vol. 23, no. 9, p. 094013, 2014.
- [47] C. Sung, E. D. Demaine, M. L. Demaine, and D. Rus, "Edge-compositions of 3D surfaces," *Journal of Mechanical Design*, vol. 135, no. 11, p. 111001, 2013.
- [48] J. Rossiter, P. Walters, and B. Stoimenov, "Printing 3D dielectric elastomer actuators for soft robotics," in *SPIE Smart Structures and Materials + Nondestructive Evaluation and Health Monitoring*. International Society for Optics and Photonics, 2009, pp. 72 870H-72 870H.
- [49] J. T. Muth, D. M. Vogt, R. L. Truby, Y. Mengüç, D. B. Kolesky, R. J. Wood, and J. A. Lewis, "Embedded 3D printing of strain sensors within highly stretchable elastomers," *Advanced Materials*, vol. 26, no. 36, pp. 6307-6312, 2014.
- [50] K. Sun, T.-S. Wei, B. Y. Ahn, J. Y. Seo, S. J. Dillon, and J. A. Lewis, "3D printing of interdigitated li-ion microbattery architectures," *Advanced Materials*, vol. 25, no. 33, pp. 4539-4543, 2013.
- [51] T. G. Leong, A. M. Zarafshar, and D. H. Gracias, "Three-dimensional fabrication at small size scales," *Small*, vol. 6, no. 7, pp. 792-806, 2010.
- [52] M. Ataka, A. Omodaka, N. Takeshima, and H. Fujita, "Fabrication and operation of polyimide bimorph actuators for a ciliary motion system," *Microelectromechanical Systems, Journal of*, vol. 2, no. 4, pp. 146-150, 1993.
- [53] J. Guan, H. He, D. J. Hansford, and L. J. Lee, "Self-folding of three-dimensional hydrogel microstructures," *The Journal of Physical Chemistry B*, vol. 109, no. 49, pp. 23 134-23 137, 2005.
- [54] N. Bassik, G. M. Stern, and D. H. Gracias, "Microassembly based on hands free origami with bidirectional curvature," *Applied Physics Letters*, vol. 95, no. 9, p. 091901, 2009.
- [55] K. E. Laflin, C. J. Morris, T. Muqeem, and D. H. Gracias, "Laser triggered sequential folding of microstructures," *Applied Physics Letters*, vol. 101, no. 13, pp. 131 901-131 901, 2012.

- [56] E. Hawkes, B. An, N. M. Benbernou, H. Tanaka, S. Kim, E. D. Demaine, D. Rus, and R. J. Wood, "Programmable matter by folding," *Proceedings of the National Academy of Sciences*, vol. 107, no. 28, p. 12441, 2010.
- [57] S. L. Keller, "Sequential folding of a rigid wire into three-dimensional structures," *American Journal of Physics*, vol. 72, no. 5, pp. 599–604, 2004.
- [58] Y. W. Yi and C. Liu, "Magnetic actuation of hinged microstructures," *Journal of Microelectromechanical Systems*, vol. 8, no. 1, pp. 10–17, 1999.
- [59] A. Antkowiak, B. Audoly, C. Josserand, S. Neukirch, and M. Rivetti, "Instant fabrication and selection of folded structures using drop impact," *Proceedings of the National Academy of Sciences*, vol. 108, no. 26, pp. 10 400–10 404, 2011.
- [60] R. Niiyama, D. Rus, and S. Kim, "Pouch motors: Printable/inflatable soft actuators for robotics," in *Robotics and Automation (ICRA), 2014 IEEE International Conference on*. IEEE, 2014, pp. 6332–6337.
- [61] Y. Liu, J. K. Boyles, J. Genzer, and M. D. Dickey, "Self-folding of polymer sheets using local light absorption," *Soft Matter*, vol. 8, no. 6, pp. 1764–1769, 2012.
- [62] K. Malachowski, M. Jamal, Q. Jin, B. Polat, C. J. Morris, and D. H. Gracias, "Self-folding single cell grippers," *Nano Letters*, vol. 14, no. 7, pp. 4164–4170, 2014.
- [63] J.-H. Na, A. A. Evans, J. Bae, M. C. Chiappelli, C. D. Santangelo, R. J. Lang, T. C. Hull, and R. C. Hayward, "Programming reversibly self-folding origami with micropatterned photo-crosslinkable polymer trilayers," *Advanced Materials*, vol. 27, no. 1, pp. 79–85, 2015.
- [64] S. Felton, M. Tolley, E. Demaine, D. Rus, and R. Wood, "A method for building self-folding machines," *Science*, vol. 345, no. 6197, pp. 644–646, 2014.
- [65] S. M. Felton, M. T. Tolley, C. D. Onal, D. Rus, and R. J. Wood, "Robot self-assembly by folding: A printed inchworm robot," in *Robotics and Automation (ICRA), 2013 IEEE International Conference on*. IEEE, 2013, pp. 277–282.
- [66] C. D. Onal, R. J. Wood, and D. Rus, "Towards printable robotics: Origami-inspired planar fabrication of three-dimensional mechanisms," in *Robotics and Automation (ICRA), 2011 IEEE International Conference on*. IEEE, 2011, pp. 4608–4613.
- [67] C. L. Randall, E. Gultepe, and D. H. Gracias, "Self-folding devices and materials for biomedical applications," *Trends in Biotechnology*, vol. 30, no. 3, pp. 138–146, 2012.
- [68] C. H. Company, "PEEKTM film," <http://catalog.cshyde.com/viewitems/films/all-categories-high-performance-film-peek-film>, 2015.
- [69] S. M. Felton, M. T. Tolley, B. Shin, C. D. Onal, E. D. Demaine, D. Rus, and R. J. Wood, "Self-folding with shape memory composites," *Soft Matter*, vol. 9, no. 32, pp. 7688–7694, 2013.

- [70] M. T. Tolley, S. M. Felton, S. Miyashita, D. Aukes, D. Rus, and R. J. Wood, "Self-folding origami: shape memory composites activated by uniform heating," *Smart Materials and Structures*, vol. 23, no. 9, p. 094006, 2014.
- [71] D. P. Dewitt and F. P. Incropera, *Fundamentals of Heat and Mass Transfer*. Wiley, 2002.
- [72] H. Tobushi, K. Okumura, S. Hayashi, and N. Ito, "Thermomechanical constitutive model of shape memory polymer," *Mechanics of materials*, vol. 33, no. 10, pp. 545-554, 2001.
- [73] J. Diani, Y. Liu, and K. Gall, "Finite strain 3d thermoviscoelastic constitutive model for shape memory polymers," *Polymer Engineering & Science*, vol. 46, no. 4, pp. 486-492, 2006.
- [74] T. D. Nguyen, H. J. Qi, F. Castro, and K. N. Long, "A thermoviscoelastic model for amorphous shape memory polymers: incorporating structural and stress relaxation," *Journal of the Mechanics and Physics of Solids*, vol. 56, no. 9, pp. 2792-2814, 2008.
- [75] P. Gilormini and J. Diani, "On modeling shape memory polymers as thermoelastic two-phase composite materials," *Comptes Rendus Mécanique*, vol. 340, no. 4, pp. 338-348, 2012.
- [76] T. Tachi, "Rigid-foldable thick origami," *Origami*, vol. 5, pp. 253-264, 2011.
- [77] J. P. Whitney, P. S. Sreetharan, K. Y. Ma, and R. J. Wood, "Pop-up book MEMS," *Journal of Micromechanics and Microengineering*, vol. 21, no. 11, p. 115021, 2011.
- [78] M. T. Tolley, S. M. Felton, S. Miyashita, L. Xu, B. Shin, M. Zhou, D. Rus, and R. J. Wood, "Self-folding shape memory laminates for automated fabrication," in *Intelligent Robots and Systems (IROS), 2013 IEEE/RSJ International Conference on*. IEEE, 2013, pp. 4931-4936.
- [79] C. Liu, H. Qin, and P. Mather, "Review of progress in shape-memory polymers," *Journal of Materials Chemistry*, vol. 17, no. 16, pp. 1543-1558, 2007.
- [80] Y. Zhu, J. Hu, H. Luo, R. J. Young, L. Deng, S. Zhang, Y. Fan, and G. Ye, "Rapidly switchable water-sensitive shape-memory cellulose/elastomer nano-composites," *Soft Matter*, vol. 8, no. 8, pp. 2509-2517, 2012.
- [81] A. Lendlein, H. Jiang, O. Jünger, and R. Langer, "Light-induced shape-memory polymers," *Nature*, vol. 434, no. 7035, pp. 879-882, 2005.
- [82] J. Cuevas, J. Alonso, L. German, M. Iturrondobeitia, J. Laza, J. Vilas, and L. Leon, "Magneto-active shape memory composites by incorporating ferromagnetic microparticles in a thermo-responsive polyalkenamer," *Smart Materials and Structures*, vol. 18, no. 7, p. 075003, 2009.

- [83] B. Heuwers, D. Quitmann, F. Katzenberg, and J. C. Tiller, "Stress-induced melting of crystals in natural rubber: a new way to tailor the transition temperature of shape memory polymers," *Macromolecular Rapid Communications*, vol. 33, no. 18, pp. 1517-1522, 2012.
- [84] T. Xie and I. A. Rousseau, "Facile tailoring of thermal transition temperatures of epoxy shape memory polymers," *Polymer*, vol. 50, no. 8, pp. 1852-1856, 2009.
- [85] J. P. de Jong and E. de Bruijn, "Innovation lessons from 3-D printing," *MIT Sloan Management Review*, vol. 54, no. 2, pp. 43-52, 2013.
- [86] B. Berman, "3-D printing: The new industrial revolution," *Business Horizons*, vol. 55, no. 2, pp. 155-162, 2012.
- [87] R. M. Snyder, "An overview of the past, present, and future of 3D printing technology with an emphasis on the present," *Association Supporting Computer Users in Education "Our Second Quarter Century of Resource Sharing"*, p. 93, 2014.
- [88] K. T. Ulrich, *Product Design and Development, Third Edition*. Tata McGraw-Hill Education, 2003.
- [89] A.-C. Liou and R.-H. Chen, "Injection molding of polymer micro-and sub-micron structures with high-aspect ratios," *The International Journal of Advanced Manufacturing Technology*, vol. 28, no. 11-12, pp. 1097-1103, 2006.
- [90] A. Woronko, J. Huang, and Y. Altintas, "Piezoelectric tool actuator for precision machining on conventional cnc turning centers," *Precision Engineering*, vol. 27, no. 4, pp. 335-345, 2003.
- [91] M. K. Barnoski, D. Cohen, D. Harris, S. Kang, A. Levi, M. Pinilla, F. Prinz, and A. Tarasyuk, "Stamping system for manufacturing high tolerance parts," Mar. 18 2008, US Patent 7,343,770.
- [92] Stratasys, "Objet30 Pro," <http://www.stratasys.com/3d-printers/design-series/objet30-pro>, 2015.
- [93] Formlabs, "Form 1+ tech specs," <http://formlabs.com/products/form-1-plus/tech-specs/>, 2015.
- [94] T. Ichimaru, "Latch with switch," Feb. 21 2006, US Patent 7,002,092.
- [95] K. Naoki, H. Shoji, and T. Sadao, "Push button switch," July 5 1988, US Patent 4,755,645.
- [96] S. P. Johnston, "Mercury switch," Feb. 25 1986, US Patent 4,572,934.
- [97] R. J. Pluta and C. M. Ko, "Force sensor," Oct. 8 1996, US Patent 5,563,355.
- [98] B. M. Finio, K. C. Galloway, and R. J. Wood, "An ultra-high precision, high bandwidth torque sensor for microrobotics applications," in *Intelligent Robots and Systems (IROS), 2011 IEEE/RSJ International Conference on*. IEEE, 2011, pp. 31-38.

- [99] B. Shin, S. M. Felton, M. T. Tolley, and R. J. Wood, "Self-assembling sensors for printable machines," in *Robotics and Automation (ICRA), 2014 IEEE International Conference on*. IEEE, 2014, pp. 4417–4422.
- [100] L. L. Howell, *Compliant Mechanisms*. Wiley-Interscience, 2001.
- [101] B. D. Jensen, L. L. Howell, and G. M. Roach, "Bistable compliant mechanism," Apr. 10 2001, US Patent 6,215,081.
- [102] K. Halbach, "Design of permanent multipole magnets with oriented rare earth cobalt material," *Nuclear Instruments and Methods*, vol. 169, no. 1, pp. 1–10, 1980.
- [103] Y. Kikuchi, F. Nakamura, H. Wakiwaka, and H. Yamada, "Index phase output characteristics of magnetic rotary encoder using a magneto-resistive element," *Magnetics, IEEE Transactions on*, vol. 33, no. 5, pp. 3370–3372, 1997.
- [104] J. C. Mallinson, "One-sided fluxes-a magnetic curiosity?" *Magnetics, IEEE Transactions on*, vol. 9, no. 4, pp. 678–682, 1973.
- [105] H. A. Shute, J. C. Mallinson, D. T. Wilton, and D. J. Mapps, "One-sided fluxes in planar, cylindrical, and spherical magnetized structures," *Magnetics, IEEE Transactions on*, vol. 36, no. 2, pp. 440–451, 2000.
- [106] J. Gafford, S. Kesner, R. Wood, and C. Walsh, "Microsurgical devices by pop-up book MEMS," in *ASME/IDETC: Robotics and Mechanisms in Medicine*. ASME, 2013.
- [107] M. Masuda, K. Sugioka, Y. Cheng, T. Hongo, K. Shihoyama, H. Takai, I. Miyamoto, and K. Midorikawa, "Direct fabrication of freely movable microplate inside photo-sensitive glass by femtosecond laser for lab-on-chip application," *Applied Physics A*, vol. 78, no. 7, pp. 1029–1032, 2004.
- [108] D. Wu, S.-Z. Wu, J. Xu, L.-G. Niu, K. Midorikawa, and K. Sugioka, "Hybrid femtosecond laser microfabrication to achieve true 3D glass/polymer composite biochips with multiscale features and high performance: the concept of ship-in-a-bottle biochip," *Laser & Photonics Reviews*, vol. 8, no. 3, pp. 458–467, 2014.
- [109] S. M. Felton, M. T. Tolley, and R. J. Wood, "Mechanically programmed self-folding at the millimeter scale," in *Automation Science and Engineering (CASE), 2014 IEEE International Conference on*. IEEE, 2014, pp. 1232–1237.
- [110] S. M. Felton, K. P. Becker, D. M. Aukes, and R. J. Wood, "Self-folding with shape memory composites at the millimeter scale," *Journal of Micromechanics and Microengineering*, to be published.
- [111] M. Yovanovich, J. Culham, and P. Teertstra, "Calculating interface resistance," *Electronics Cooling*, vol. 3, no. 2, pp. 24–29, 1997.
- [112] Z. Teoh and R. Wood, "A flapping-wing microrobot with a differential angle-of-attack mechanism," in *Robotics and Automation (ICRA), 2013 IEEE International Conference on*. IEEE, 2013, pp. 1381–1388.

- [113] H. Jeong, B. Kim, and Y. Choi, "Synthesis and properties of thermotropic liquid crystalline polyurethane elastomers," *Polymer*, vol. 41, no. 5, pp. 1849–1855, 2000.
- [114] F. Cao and S. C. Jana, "Nanoclay-tethered shape memory polyurethane nanocomposites," *Polymer*, vol. 48, no. 13, pp. 3790–3800, 2007.
- [115] K. Gall, M. L. Dunn, Y. Liu, G. Stefanic, and D. Balzar, "Internal stress storage in shape memory polymer nanocomposites," *Applied Physics Letters*, vol. 85, no. 2, pp. 290–292, 2004.
- [116] W. Voit, T. Ware, R. R. Dasari, P. Smith, L. Danz, D. Simon, S. Barlow, S. R. Marder, and K. Gall, "High-strain shape-memory polymers," *Advanced Functional Materials*, vol. 20, no. 1, pp. 162–171, 2010.
- [117] I. A. Rousseau, "Challenges of shape memory polymers: A review of the progress toward overcoming SMP's limitations," *Polymer Engineering & Science*, vol. 48, no. 11, pp. 2075–2089, 2008.
- [118] T. Kojima, Y. Kikuchi, S. Seki, and H. Wakiwaka, "Study on high accuracy optical encoder with 30 bits," in *Advanced Motion Control (AMC), 2004, the 8th IEEE International Workshop on*. IEEE, 2004, pp. 493–498.
- [119] C.-W. Lin, Z. Zhao, J. Kim, and J. Huang, "Pencil drawn strain gauges and chemiresistors on paper," *Scientific Reports*, vol. 4, 2014.
- [120] P. Cheng and B. Oelmann, "Joint-angle measurement using accelerometers and gyroscopes—a survey," *Instrumentation and Measurement, IEEE Transactions on*, vol. 59, no. 2, pp. 404–414, 2010.
- [121] J. K. Paik, R. K. Kramer, and R. J. Wood, "Stretchable circuits and sensors for robotic origami," in *Intelligent Robots and Systems (IROS), 2011 IEEE/RSJ International Conference on*. IEEE, 2011, pp. 414–420.
- [122] M. Maiwald, C. Werner, V. Zoellmer, and M. Busse, "Inktelligent printed strain gauges," *Sensors and Actuators A: Physical*, vol. 162, no. 2, pp. 198–201, 2010.
- [123] Y.-W. Lu and C.-J. C. Kim, "Microhand for biological applications," *Applied Physics Letters*, vol. 89, no. 16, p. 164101, 2006.
- [124] X. Sun, S. M. Felton, R. Niiyama, R. J. Wood, and S. Kim, "Self-folding and self-actuating robots: a pneumatic approach," in *Robotics and Automation (ICRA), 2015 IEEE International Conference on*. IEEE, 2015.
- [125] Y.-L. Park, J. Santos, K. G. Galloway, E. C. Goldfield, and R. J. Wood, "A soft wearable robotic device for active knee motions using flat pneumatic artificial muscles," in *Robotics and Automation (ICRA), 2014 IEEE International Conference on*. IEEE, 2014, pp. 4805–4810.
- [126] Y. Bellouard, T. Lehnert, J.-E. Bidaux, T. Sidler, R. Clavel, and R. Gotthardt, "Local annealing of complex mechanical devices: a new approach for developing monolithic micro-devices," *Materials Science and Engineering: A*, vol. 273, pp. 795–798, 1999.

- [127] P. Krulevitch, A. P. Lee, P. B. Ramsey, J. C. Trevino, J. Hamilton, and M. A. Northrup, "Thin film shape memory alloy microactuators," *Journal of Microelectromechanical Systems*, vol. 5, no. 4, pp. 270-282, 1996.
- [128] A. Jain and H. Xie, "A single-crystal silicon micromirror for large bi-directional 2D scanning applications," *Sensors and Actuators A: Physical*, vol. 130, pp. 454-460, 2006.
- [129] B. Y. Ahn, D. Shoji, C. J. Hansen, E. Hong, D. C. Dunand, and J. A. Lewis, "Printed origami structures," *Advanced Materials*, vol. 22, no. 20, pp. 2251-2254, 2010.
- [130] S. Tibbits, "4D printing: Multi-material shape change," *Architectural Design*, vol. 84, no. 1, pp. 116-121, 2014.
- [131] S. Mueller, B. Kruck, and P. Baudisch, "Laserorigami: laser-cutting 3D objects," in *Proceedings of the SIGCHI Conference on Human Factors in Computing Systems*. ACM, 2013, pp. 2585-2592.
- [132] Y. Kawahara, S. Hodges, B. S. Cook, C. Zhang, and G. D. Abowd, "Instant inkjet circuits: lab-based inkjet printing to support rapid prototyping of ubicomp devices," in *Proceedings of the 2013 ACM International Joint Conference on Pervasive and Ubiquitous Computing*. ACM, 2013, pp. 363-372.
- [133] X. Liu, M. Mwangi, X. Li, M. O'Brien, and G. M. Whitesides, "Paper-based piezoresistive MEMS sensors," *Lab on a Chip*, vol. 11, no. 13, pp. 2189-2196, 2011.
- [134] A. Albarbar, A. Badri, J. K. Sinha, and A. Starr, "Performance evaluation of MEMS accelerometers," *Measurement*, vol. 42, no. 5, pp. 790-795, 2009.
- [135] S. Miyashita, L. Meeker, M. Gouldi, Y. Kawahara, and D. Rus, "Self-folding printable elastic electric devices: Resistor, capacitor, and inductor," in *Robotics and Automation (ICRA), 2014 IEEE International Conference on*. IEEE, 2014, pp. 1446-1453.
- [136] W. Noell, P.-A. Clerc, L. Dellmann, B. Guldemann, H.-P. Herzig, O. Manzardo, C. R. Marxer, K. J. Weible, R. Dandliker, and N. de Rooij, "Applications of SOI-based optical MEMS," *Selected Topics in Quantum Electronics, IEEE Journal of*, vol. 8, no. 1, pp. 148-154, 2002.
- [137] E. Timurdogan, B. E. Alaca, I. H. Kavakli, and H. Urey, "MEMS biosensor for detection of hepatitis A and C viruses in serum," *Biosensors and Bioelectronics*, vol. 28, no. 1, pp. 189-194, 2011.
- [138] R. Wood, E. Steltz, and R. Fearing, "Optimal energy density piezoelectric bending actuators," *Sensors and Actuators A: Physical*, vol. 119, no. 2, pp. 476-488, 2005.
- [139] F. Carpi, C. Salaris, and D. De Rossi, "Folded dielectric elastomer actuators," *Smart Materials and Structures*, vol. 16, no. 2, p. S300, 2007.
- [140] A. S. Chen, H. Zhu, Y. Li, L. Hu, and S. Bergbreiter, "A paper-based electrostatic zipper actuator for printable robots," in *Robotics and Automation (ICRA), 2014 IEEE International Conference on*. IEEE, 2014, pp. 5038-5043.

- [141] R. T. Schroer, M. J. Boggess, R. J. Bachmann, R. D. Quinn, and R. E. Ritzmann, "Comparing cockroach and whegs robot body motions," in *Robotics and Automation (ICRA), 2004 IEEE International Conference on*, vol. 4. IEEE, 2004, pp. 3288–3293.
- [142] P. Birkmeyer, K. Peterson, and R. S. Fearing, "DASH: A dynamic 16g hexapedal robot," in *Intelligent Robots and Systems (IROS), 2009 IEEE/RSJ International Conference on*. IEEE, 2009, pp. 2683–2689.
- [143] T. Hack, "Experiments with a new piezoelectric rotary actuator," in *Frequency Control Symposium, 1998. Proceedings of the 1998 IEEE International*. IEEE, 1998, pp. 724–732.
- [144] S. M. Barnes, S. L. Miller, M. S. Rodgers, and F. Bitsie, "Torsional ratcheting actuating system," in *Sandia National Laboratories, Albuquerque, NM, Technical Proceedings of the 2000 International Conference on Modeling and Simulation of Microsystems*, 2000, pp. 27–29.
- [145] J. Lloyd and W. Moran, "Natural convection adjacent to horizontal surface of various planforms," *Journal of Heat Transfer*, vol. 96, no. 4, pp. 443–447, 1974.
- [146] T. Fujii and H. Imura, "Natural-convection heat transfer from a plate with arbitrary inclination," *International Journal of Heat and Mass Transfer*, vol. 15, no. 4, pp. 755–767, 1972.
- [147] D. R. Lide, *CRC Handbook of Chemistry and Physics*. CRC press, 2002.
- [148] B. Suleiman, J. Larfeldt, B. Leckner, and M. Gustavsson, "Thermal conductivity and diffusivity of wood," *Wood science and technology*, vol. 33, no. 6, pp. 465–473, 1999.
- [149] R. Lopatkiewicz, Z. Nadolny, and P. Przybylek, "The influence of water content on thermal conductivity of paper used as transformer windings insulation," in *Properties and Applications of Dielectric Materials (ICPADM), 2012 IEEE 10th International Conference on the*. IEEE, 2012, pp. 1–4.
- [150] P. T. Mather, X. Luo, and I. A. Rousseau, "Shape memory polymer research," *Annual Review of Materials Research*, vol. 39, pp. 445–471, 2009.
- [151] T. Electronics, "RNF-100," <http://raychem.te.com/documents/webservice/fetch.ashx?fileid=7102&docId=1159>, 2015.
- [152] G. Boothroyd, P. Dewhurst, and W. A. Knight, *Product Design for Manufacture and Assembly, Third Edition*. CRC Press, 2010.
- [153] K. C. Polgar, "Simplified time estimation for basic machining operations," Master's thesis, Massachusetts Institute of Technology, 1996.

A

Parts and Materials

A.1 Inchworm Composite

Material	Thickness	Provider	Number
Polystyrene (PS)	300 μm	Grafix	KSF50-CIJ
Polyetheretherketone (PEEK)	125 μm	Victrex	APTIV 1000
Copper-clad polyimide (CuPI)	30 μm	DuPont	AC181200R
Silicone tape	50 μm	Adhesives Research	ARclad 7876

A.2 Inchworm Composite Cost

Component	Unit Cost
Polystyrene	\$7.21/m ²
Polyetheretherketone	\$270.00/m ²
Copper-clad polyimide	\$197.94/m ²
Silicone Tape	\$79.71/m ²
Complete composite	\$721.49/m ²

A.3 Unidirectional Paper Composite

Material	Thickness	Provider	Number
Polyolefin (PO)	410 μm	Raychem	RNF-100-1-BK-STK
	560 μm		RNF-100-2-BK-STK
	690 μm		TAT-125-2-0
Paper	510 μm	Epson	Cold Press Bright
Copper-clad polyimide (CuPI)	30 μm	DuPont	AC181200R
Silicone tape	50 μm	Adhesives Research	ARclad 7876

A.4 Bidirectional Paper Composite

Material	Thickness	Provider	Number
Polystyrene (PS)	250 μm	Grafix	KSF50-C
Paper	510 μm	Canon	0850V071
Copper-clad polyimide (CuPI)	43 μm	DuPont	AC182500R
Silicone tape	50 μm	Adhesives Research	ARclad 7876

A.5 Bidirectional Composite Cost

Component	Unit Cost
Polystyrene	\$7.21/m ²
Paper	\$14.85/m ²
Copper-clad Polyimide	\$197.94/m ²
Silicone tape	\$79.71/m ²
Complete composite	\$560.90/m ²

A.6 Uniformly Heated Paper Composite

Material	Thickness	Provider	Number
Polystyrene (PS)	250 μ m	Grafix	KSF50-C
Paper	510 μ m	Canon	0850V071

A.7 Uniformly Heated Composite Cost

Component	Unit Cost
Polystyrene	\$7.21/m ²
Paper	\$14.85/m ²
Complete composite	\$36.91/m ²

A.8 Crawling Robot Components

Component	Amount	Provider	Number
Microcontroller	1	Atmel	ATTiny13
Buffered H-bridge	2	Vishay Siliconix	Si9988
Dual MOSFET	2	Fairchild Semiconductor	FDS6930B
Voltage regulator	2	Vishay Diodes Inc.	AP1117
Resistors, 1.0 Ω	2	Vishay Dale	MRA-051R000FE12
Resistors, 0.75 Ω	2	Vishay Dale	RCWE2512R750FKEA
Resistors, 0.5 Ω	4	TT Electronics	LR2512-R50FW
Capacitors, 4.7 μ F	4	Kemet	C0402C475M7PACTU
DC motor	2	Precision Microdrive	210-002
LiPo battery, 7.4 V	2	E-flite	EFLB1802S20

A.9 Millimeter-Scale Composite 1

Material	Thickness	Provider	Number
Polyolefin (PO)	18 μ m	Syfan	Sytec MVP 75 G
Aluminum 1145-H19 (Al)	50 μ m	Shop-Aid	
Polyester (PE)	2.5 μ m	Chemplex	100
Liquid Adhesive (CA)	10 μ m	Loctite	496

A.10 Millimeter-Scale Composite 2

Material	Thickness	Provider	Number
Polyolefin (PO)	25 μm	U.S.Packaging&Wrapping	DU-POF-1000-8
Aluminum 1145-H19 (Al)	50 μm	Shop-Aid	
FR-4	50 μm	Isola Group	FR408HR
Polyimide (PI)	7.5 μm	Chemplex	440
Acrylic tape	5 μm	3M	82600

B

Thermal Model

B.1 Solution for PDE

We can model our thermal system as a sum of solutions, each representing the energy generated from a point along the resistive trace in the core region. Consider the solution $T_j(x, t)$ that represents the thermal diffusion due to a point heat source at $x = j$. The total thermal system T can be solved by integrating across every solution T_j at the same point x and time t .

$$T(x, t) = \int_{-w_t/2}^{w_t/2} T_j(x, t) dj \quad (\text{B.1})$$

Each T_j can be rewritten in a different spatial coordinate ξ as a single solution T_n for a point source at $\xi = 0$. This allows us to rewrite the integral for T .

$$\xi = x - j \quad (\text{B.2})$$

$$T_j(x, t) = T_n(\xi, t) \quad (\text{B.3})$$

$$\int_{-w_t/2}^{w_t/2} T_j(x, t) dj = \int_{x-w_t/2}^{x+w_t/2} T_n(\xi, t) d\xi \quad (\text{B.4})$$

B.2 Derivation of Convection Coefficient

The convection coefficient h of a fluid along the surface of a solid is dependent on the Nusselt number Nu of the fluid-solid interface, the conductivity k of the liquid, and the characteristic length L_{ch} of the geometry.

$$h = Nu L_{ch} / k \quad (\text{B.5})$$

In the case of the hinge, we consider the geometry directly above the resistive trace because the temperature at this location is significantly higher than elsewhere along the composite.

For a horizontal rectangle defining the core region, $L_{ch} = w_t L_h / (2w_t + 2L_h)$.

$$L_{ch} = \frac{(30 \text{ mm})(6 \text{ mm})}{72 \text{ mm}} = 2.5 \text{ mm} \quad (\text{B.6})$$

The Nusselt number can be determined from another dimensionless number, the Rayleigh Number (Ra), which is in turn the product of two more dimensionless numbers: the Prandtl number (Pr) and the Grashof number (Gr). The Nusselt equation is dependent on both the system geometry and Ra ; for this system we use an equation from Lloyd and Moran [145]. We simplify the model by solving for the convection and other properties at a constant temperature T_{char} .

For the unidirectional composite supplied with 2 A, $T_{char} = 150$ (170 °C).

$$Pr = \frac{\nu}{\alpha} = \frac{16.0 \times 10^{-6} \text{ m}^2/\text{s}}{22.4 \times 10^{-6} \text{ m}^2/\text{s}} = 0.71 \quad (\text{B.7})$$

$$\begin{aligned} Gr &= \frac{g \beta (T_{char} - T_{atm}) L_{ch}^3}{\nu^2} \\ &= \frac{(9.8 \text{ m/s}^2) (3.43 \times 10^{-3} \text{ 1/K}) (125 \text{ K}) (1.6 \times 10^{-8} \text{ m}^3)}{(16.0 \times 10^{-6} \text{ m}^2/\text{s})^2} = 308 \end{aligned} \quad (\text{B.8})$$

$$Ra = Pr \times Gr = 219 \quad (\text{B.9})$$

$$Nu = 0.96 Ra^{0.17} = 2.4 \quad (\text{B.10})$$

$$h = \frac{Nu L_{ch}}{k} = \frac{(2.3) (2.5 \times 10^{-3} \text{ m})}{26.2 \times 10^{-3} \text{ W/mK}} = 25 \text{ W/m}^2\text{K} \quad (\text{B.11})$$

For the same composite supplied with 1.75 A, $T_{char} = 80$ (100 °C).

$$Gr = 164 \quad (\text{B.12})$$

$$Ra = 117 \quad (\text{B.13})$$

$$Nu = 2.1 \quad (\text{B.14})$$

$$h = 22 \text{ W/m}^2\text{K} \quad (\text{B.15})$$

The bidirectional composite is experiencing convection on both the top and bottom surfaces, and the bottom surface is governed by a different Nu_b , which we derive using an equation from Fujii and Imura [146]. For the bidirectional composite supplied with 2 A,

$$T_{char} = 200 \text{ (220 } ^\circ\text{C)}.$$

$$Gr = 503 \tag{B.16}$$

$$Ra = Pr \times Gr = 359 \tag{B.17}$$

$$Nu_t = 2.6 \tag{B.18}$$

$$h_t = 25 \text{ W/m}^2\text{K} \tag{B.19}$$

$$Nu_b = 0.58 Ra^{0.2} = 1.9 \tag{B.20}$$

$$h_b = 18 \text{ W/m}^2\text{K} \tag{B.21}$$

For the bidirectional composite supplied with 1.5 A, $T_{char} = 90$ (110 $^\circ\text{C}$).

$$Gr = 226 \tag{B.22}$$

$$Ra = Pr \times Gr = 162 \tag{B.23}$$

$$Nu_t = 2.2 \tag{B.24}$$

$$h_t = 22 \text{ W/m}^2\text{K} \tag{B.25}$$

$$Nu_b = 1.6 \tag{B.26}$$

$$h_b = 16 \text{ W/m}^2\text{K} \tag{B.27}$$

For the bidirectional composite supplied with 1.75 A, $T_{char} = 150$ (170 $^\circ\text{C}$).

$$Gr = 377 \tag{B.28}$$

$$Ra = Pr \times Gr = 269 \tag{B.29}$$

$$Nu_t = 2.4 \tag{B.30}$$

$$h_t = 24 \text{ W/m}^2\text{K} \tag{B.31}$$

$$Nu_b = 1.8 \tag{B.32}$$

$$h_b = 17 \text{ W/m}^2\text{K} \tag{B.33}$$

Using an explicit model to calculate the marginal convection coefficient h_m is challenging

Table B.1: Material properties used in the hinge thermal model.

Property	Symbol	Value	Units
Air			
Thermal conductivity	k	26.2×10^{-3} [147]	W/mK
Viscosity	μ	18.6×10^{-6} [147]	Pa s
Density	ρ	1.16 [147]	kg/m ³
Kinematic viscosity	ν	16.0×10^{-6}	m ² /s
Specific heat capacity	c_p	1007 [147]	J/kg K
Thermal diffusivity	α	22.4×10^{-6}	m ² /s
Thermal expansion coefficient	β	3.43×10^{-3}	1/K
Polystyrene—SMP			
Thermal conductivity	k	0.2	W/mK
Density	ρ	1200	kg/m ³
Specific heat capacity	c_p	1400	J/kg K
Transition Temperature	T_g	105	°C
Transition Range	T_r	15	°C
Polyolefin—SMP			
Thermal conductivity	k	0.2	W/mK
Density	ρ	1200	kg/m ³
Specific heat capacity	c_p	1200	J/kg K
Transition Temperature	T_g	95	°C
Transition Range	T_r	30	°C
Paper—substrate			
Thermal conductivity	k	0.25 [148, 149]	W/mK
Density	ρ	650	kg/m ³
Specific heat capacity	c_p	1500	J/kg K
Silicone—adhesive			
Thermal conductivity	k	0.2	W/mK
Density	ρ	1100	kg/m ³
Specific heat capacity	c_p	1000	J/kg K
Acrylic—table surface			
Thermal conductivity	k	0.18	W/mK
Density	ρ	1150	kg/m ³
Specific heat capacity	c_p	1470	J/kg K

because the temperature varies along the length of the marginal region, and one edge of the region is adjacent the core region with a significantly higher temperature. This heat would convect away from the core and over the margin, reducing the effective convective transfer coefficient over the hottest part of the marginal region. Therefore, we settled for approximating h_m by assuming $h_m = h_c/5$ for a given system.

B.3 1D Approximation

The geometry of the hinge is effectively constant in the y-direction, so we assume that the hinge is isothermal in that direction. Experimentally we observed that there were variations in the temperature at the edges of the material, but these regions are relatively small and difficult to model. Figure B.1 shows the measured temperature across a bidirectional composite hinge at 50 s and 150 s. When the hinge is reaching the transition temperature of the SMP, the marginal area is about 15% of the total hinge length, but the edge effects appear to grow larger as the temperature increases.

In the z-direction (vertical), we calculated the Biot number $Bi = h_s t_s / k_s$, which indicates the ratio between conduction through a material and the convection at its surface. For the SMP layer, Bi is much smaller than one for all hinges tested, indicating that conduction through the SMP will occur more quickly than convection. Because of this, we can ignore the transient effects of vertical conduction, and assume that the vertical heat conduction

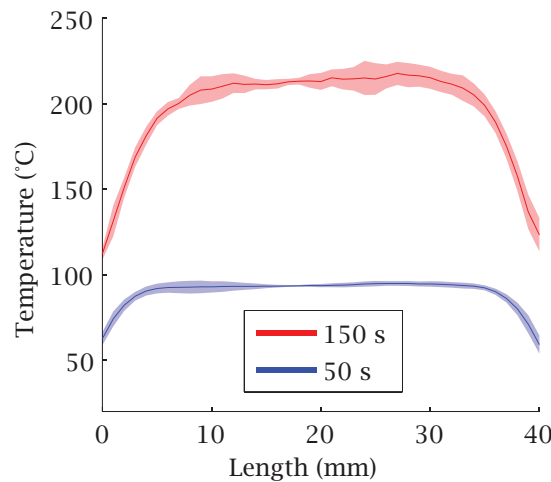


Figure B.1: The thermal profile along the hinge of a bidirectional composite after being supplied two amperes of current for 50 s (blue) and 150 s (red). Shaded region indicates standard deviation, $N=4$.

through the SMP is equal to the convection from the SMP surface.

$$h_{smp}T_s = \frac{(T - T_s)k}{t_s} \quad (\text{B.34})$$

$$T_s = C_s T = \frac{k}{k + ht_s} T \quad (\text{B.35})$$

In this way we can solve for the ratio C_s of the surface SMP temperature T_s to the inner SMP temperature T . For all of our experimental hinges, $C_s > 0.9$. Therefore, for the sake of simplification, we assume the material is isothermal in the z-direction, and can be treated as a one-dimensional system.

B.4 Derivation of Bulk Conductivity and Diffusivity Terms

Our 1D models assume uniform material properties. We derive the bulk conductivity k and diffusivity α from the material properties and thicknesses of each layer in the composite. k can be expressed as the sum of the conductivities k_i multiplied by the thicknesses t_i of all n layers.

$$k = \frac{\sum_{i=0}^n k_i t_i}{\sum_{i=0}^n t_i} \quad (\text{B.36})$$

α is a function of k and the bulk heat capacity c .

$$\alpha = \frac{k}{c} \quad (\text{B.37})$$

$$c = \frac{\sum_{i=0}^n \rho_i c_i t_i}{\sum_{i=0}^n t_i} \quad (\text{B.38})$$

B.5 Derivation of Core Convection Term

The convection at the core h_c is proportional to the heat transfer coefficient at the surface of our ideal system h . However, These two values are not equal, because h is occurring along the virtual length of the surface L_c and h_c is occurring along the width of the trace w_t . Instead, we estimate h as a function of h_c , L_c , and w_t .

$$Q_{vc} = hL_c = h_c w_t \quad (\text{B.39})$$

$$h = \frac{w_t}{L_c} h_c \quad (\text{B.40})$$

The temperature T is also increasing the resistance of the circuit, which increases the power generated. Fortunately, this effect can be lumped in with the convection term in the model because both result in heat transfer at the surface that's linearly proportional to the temperature. If we consider the total thermal flux Q_{tot} occurring in the core as a function of the core convection Q_{vc} and heat generation Q_g from the heating element, we can rearrange it as seen below, resulting in lump convection h . R_0 is the resistance of the heating trace at $T = 0$ and α_{tc} is the temperature coefficient of resistance.

$$\begin{aligned} Q_{tot} &= Q_g - Q_{vc} \\ &= I^2 R - h_c T L_h w_t \\ &= I^2 R_0 (1 + \alpha_{tc} T) - h_c T L_h w_t \\ &= I^2 R_0 - T (h_c L_h w_t - I^2 R_0 \alpha_{tc}) \\ &= I^2 R_0 - T (\bar{h} L_h w_t) \end{aligned} \quad (\text{B.41})$$

$$\bar{h} = \frac{h_c L_h w_t - I^2 R_0 \alpha_{tc}}{L_h w_t} \quad (\text{B.42})$$

$$h = \frac{h_c L_h w_t - I^2 R_0 \alpha_{tc}}{L_c L_h} \quad (\text{B.43})$$

B.6 Validation of Core Convection Approximation

In order to test our assumption that the core convection can be approximated as a function of trace width, $\bar{h} = h_c w_t / L_c$, we compared our analytical model to a numerical solution for a hinge system without any convection along the marginal area and trace widths of 3 mm, 6 mm, and 9 mm when supplied a fixed amount of current (2 A or 1.5 A). We used the composite design for the bidirectional hinge, assuming an elevated hinge so that there was no z-direction conduction, and the only form of heat loss was through core convection. The results can be seen in Figure B.2, indicating that our approximation of surface convection

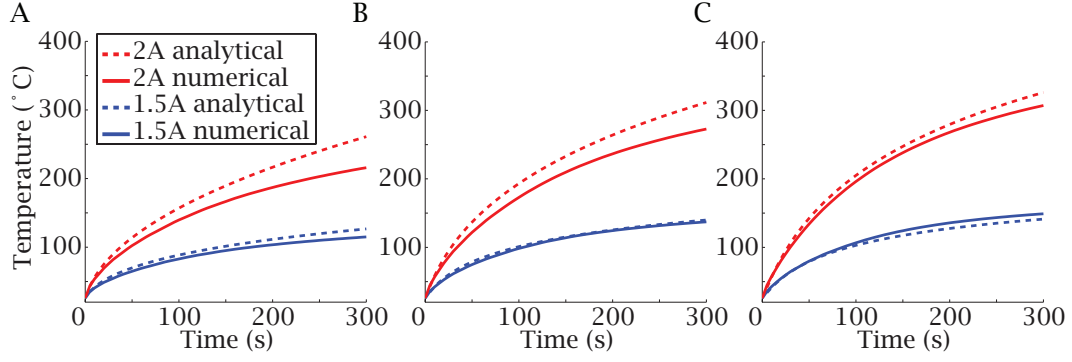


Figure B.2: Analytical (dashed) and numerical (solid) model predictions of hinge temperature as a function of time, assuming no marginal convection, for trace widths of (A) 3 mm, (B) 6 mm, and (C) 9 mm when supplied either 2 A or 1.5 A.

is reasonable.

B.7 Derivation of Dissipation Term

The dissipation along the margin due to convection with a heat transfer coefficient h_m can be simplified to a single term β . In order to determine β , we solve for the energy balance for a discrete element of length dx .

$$\frac{\Delta Q_i}{\Delta t} = \frac{k t (T_{i+1} - T_i)}{\Delta x} + \frac{k t (T_{i-1} - T_i)}{\Delta x} - h T_i \Delta x \quad (\text{B.44})$$

$$\frac{\Delta T_i}{\Delta t} = \frac{\Delta Q_i}{t \Delta x \rho c_p \Delta t} = \frac{k \Delta^2 T_i}{(\Delta x)^2 \rho c_p} - \frac{h T_i}{t \rho c_p} \quad (\text{B.45})$$

$$\frac{\partial T}{\partial t} = \frac{\partial^2 T}{\partial x^2} - dT \quad (\text{B.46})$$

$$\beta = \frac{h_m}{t \rho c_p} \quad (\text{B.47})$$

B.8 Derivation of Regime Transition Time

Our analytical solution consists of two regimes: The initial regime when $T \approx 0$, and the steady-state regime when $\partial T / \partial t \approx 0$. We consider the boundary between these two regimes

based on when the initial solution would intersect with the steady-state solution at $x = 0$.

$$T_i(0, t) = \frac{q}{h} \left(1 - \exp \left(\frac{h^2 \alpha t}{k^2} \right) \operatorname{erfc} \left(\frac{h \sqrt{\alpha t}}{k} \right) \right) \quad (\text{B.48})$$

$$T_o(0) = \frac{q}{h + k \sqrt{\frac{\beta}{\alpha}}} \quad (\text{B.49})$$

$$T_i(0, t_r) = T_o(0) \quad (\text{B.50})$$

$$\psi = \frac{h^2 \alpha t_r}{k^2} \quad (\text{B.51})$$

$$\frac{h}{h + k \sqrt{\frac{\beta}{\alpha}}} = C_h = 1 - \exp(\psi) \operatorname{erfc}(\sqrt{\psi}) \quad (\text{B.52})$$

We can solve for ψ numerically, but for our models we use the following analytical approximation.

$$1 - \exp(-\sqrt{\psi}) \approx 1 - \exp(\psi) \operatorname{erfc}(\sqrt{\psi}) \quad (\text{B.53})$$

$$\psi \approx \log(1 - C_h)^2 \quad (\text{B.54})$$

$$t_r = \psi \frac{k^2}{\alpha h^2} \quad (\text{B.55})$$

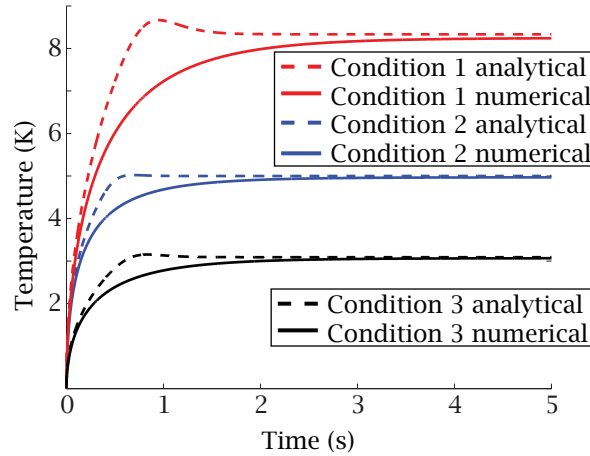


Figure B.3: Comparison of analytical (dashed) and numerical (solid) models for a 1D, transient, semi-infinite system with convection and heat generation at the surface, and dissipation throughout its length. Red indicates condition 1, blue indicates condition 2, and black indicates condition 3 (see Table B.2 for parameters).

Table B.2: Physical parameters used when comparing analytical and numerical models.

Condition	q	k	h	α	β
1	10 W/m ²	1 W/(mK)	0.2 W/(m ² K)	1 m ² /s	1 s ⁻¹
2	10 W/m ²	1 W/(mK)	1 W/(m ² K)	1 m ² /s	1 s ⁻¹
3	10 W/m ²	5 W/(mK)	1 W/(m ² K)	1 m ² /s	1 s ⁻¹

B.9 Validation of Regime Transition Model

To find an approximate solution to the governing PDE (B.56) and boundary conditions, we find separate solutions for the initial regime T_i and steady-state regime T_o and combine them using an equation F_s .

$$\frac{\partial T}{\partial t} = \alpha \frac{\partial^2 T}{\partial x^2} - \beta T \quad (\text{B.56})$$

$$T(x, 0) = 0 \quad (\text{B.57})$$

$$-k \left. \frac{\partial T(x, t)}{\partial x} \right|_{x=0} = q - hT(0, t) \quad (\text{B.58})$$

$$T_i(x, t) = \frac{q}{h} \left[\operatorname{erfc} \left(\frac{x}{\sqrt{4\alpha t}} \right) - \exp \left(\frac{hx}{k} + \frac{h^2 \alpha t}{k^2} \right) \operatorname{erfc} \left(\frac{x}{\sqrt{4\alpha t}} + \frac{h\sqrt{\alpha t}}{k} \right) \right] \quad (\text{B.59})$$

$$T_o(x) = \left(\frac{q}{h + k\sqrt{\frac{\beta}{\alpha}}} \right) \exp \left(-\sqrt{\frac{\beta}{\alpha}} x \right) \quad (\text{B.60})$$

$$F_s = \frac{1}{1 + \exp(5(1 - t/t_r))} \quad (\text{B.61})$$

$$T(x, t) = T_i(x, t) + F_s(T_o(x) - T_i(x, t)) \quad (\text{B.62})$$

To validate this model, we compare it to a discrete-time linear state-space model of the full PDE, written in Matlab. Figure B.3 compares the analytic and numerical models for three different systems. The parameters for these systems are shown in Table B.2.

B.10 Explanation of the Virtual Surface Thickness

To approximate the 2D diffusion of heat into the surface on which the hinge is resting, we include an additional layer in our model composite. This layer has identical material properties to the table surface (for our experiments, this material is acrylic). We must also give this layer a representative thickness t_v , to account for the total energy flux at the surface of our system and approximate the specific flux into a given thickness of the

composite. t_v can be thought of as a semicircle around the hinge, so that our analytical model effectively sweeps the 1D solution in a radial pattern around the heat source. At $t = 0$, we expect that, for a point source, the characteristic length L_c of the material into which it is diffusing is small, so we assume $t_v = 0$ at $t = 0$. As $t \rightarrow \infty$, we expect that the thermal system asymptotically approaches a steady state, so we assume that t_v approaches a constant. To capture this behavior in our model we use Equation (B.63); it was chosen because it has a form similar to the one found in Appendix B.8 to approximate the surface temperature with respect to time. We chose appropriate constants based on our experimental results. We do not have a physical justification for these values, but it is worth noting that $0.025 \text{ s} \sim h\sqrt{\alpha(1 \text{ s})}/k$ for the parameters of our experiments, and these parameters appear in this form in the original Equation (B.53).

$$t_v = (12 \text{ mm}) \left[1 - \exp \left(-0.025 \sqrt{t/(1 \text{ s})} \right) \right] \quad (\text{B.63})$$

Mechanical Model

C.1 Values for Determining Maximum Face Size

C.1.1 Bidirectional Composite

Value	Symbol	Value	Units
Density of polystyrene	ρ_s	1200	kg/m ³
Thickness of polystyrene	t_s	250	μm
Density of polyimide	ρ_h	1400	kg/m ³
Thickness of polyimide	t_h	25	μm
Density of adhesive	ρ_d	1100	kg/m ³
Thickness of adhesive	t_d	50	μm
Density of paper	ρ_p	650	kg/m ³
Thickness of paper	t_p	510	μm
Area density of composite	ρ_A	1.51	kg/m ²
Torque per meter	τ_s	70	mN m/m
Max face length	L_{max}	97	mm

C.1.2 Uniformly Heated Composite

Value	Symbol	Value	Units
Area density of composite	ρ_A	1.07	kg/m ²
Torque per meter	τ_s	96	mN m/m
Max face length	L_{max}	142	mm

C.1.3 Millimeter Scale Composite

Value	Symbol	Value	Units
Density of polyolefin	ρ_p	1000	kg/m ³
Thickness of polyolefin	t_p	25	μm
Density of polyimide	ρ_h	1400	kg/m ³
Thickness of polyimide	t_h	7.5	μm
Density of adhesive	ρ_d	1200	kg/m ³
Thickness of adhesive	t_d	5	μm
Density of aluminum	ρ_{al}	2700	kg/m ³
Density of FR-4	ρ_{fr}	1400	kg/m ³
Thickness of substrate	t_s	50	μm
Area density of aluminum composite	ρ_a	636	g/m ²
Area density of FR-4 composite	ρ_f	467	g/m ²
Lever arm	δ_s	76	μm
Torque per meter	τ	9.7	mN m/m
Max face length—aluminum	L_{max}	56	mm
Max face length—FR-4	L_{max}	65	mm

C.2 Shape Memory Polymer Characterization

The relationship between stress and strain in an SMP is complex. SMPs generally exhibit viscoelastic behavior and undergo large strains, often exceeding their linear elastic regime [150]. Their behavior is also temperature-dependent, especially as the SMP transitions from a glass to a rubber phase [72]. For the purposes of our models, we assume that the heating process occurs quickly enough that the SMP phase transition is a discrete event, allowing us to ignore the temperature dependence and viscoelastic effects.

C.2.1 Thick Polyolefin

The thick polyolefin used in our experiments (Section 3.2) contracts uniaxially and has a shrink ratio of 2-to-1, indicating it shrinks to 50% of its initial length. It has a transition temperature T_g of 95 °C and a full recovery temperature of 125 °C [151], indicating a transition range $2T_r$ of 60 °C.

To measure the Young's modulus of the SMP, a 25 mm wide by 15 mm long strip of 410 μm thick polyolefin (PO) was heated above 120 °C via joule heating from a flexible circuit. While heated, it was stretched at a rate of 500 $\mu\text{m s}^{-1}$ to a final length of 30 mm in a material testing machine (5566, Instron). During this time the resulting force was measured at 20 Hz. The force was found to be approximately linearly proportional to the displacement over the range measured (Fig. C.1). This indicates that the PO remained

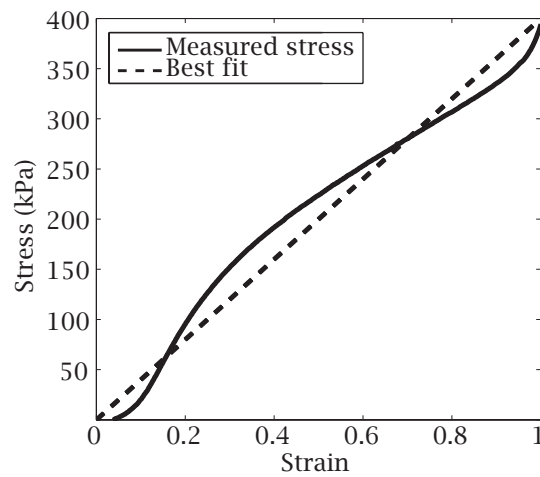


Figure C.1: The measured stress (solid line) of a single polyolefin sample as a function of strain under a constant strain rate of 0.033 s^{-1} . The dashed line indicates our linear model with a Young's modulus of 400 kPa.

elastic up to a strain of 1 in its rubber state, which is the effective strain its under when it is first activated. The Young's modulus in the rubber state was determined to be 400 kPa from the ratio of the engineering stress to the strain.

C.2.2 Polystyrene

In order to determine the transition temperature and range of the PS, we placed 216 mm long samples in a temperature-controlled oven at temperatures ranging from 70 °C to 140 °C for at least five minutes, and then removed, cooled, and measured. These measurements are shown in Figure C.2, and the data indicates that the transition temperature $T_g = 105^\circ\text{C}$, with a transition range $2T_r = 30^\circ\text{C}$

The contractile stress of the PS was measured using a material testing machine (5544A, Instron). Five dogbone samples with a width of 10 mm and a length of 50 mm were fixed in length and then activated with a heat gun. The peak contractile force was measured to be 1.74 N with a standard deviation of 0.16 N. Given that the PS is 250 μm thick, the contractile stress of the PS is $696 \pm 64\text{kPa}$.

C.2.3 Thin Polyolefin

The thin polyolefin (PO) used in our experiments (Chapter 6) has a shrink ratio of 4-to-1, meaning that it contracts to 25% of its original length when activated. This also means that if it transitions into its rubber phase while its length is fixed, it is under an equivalent strain of 300%.

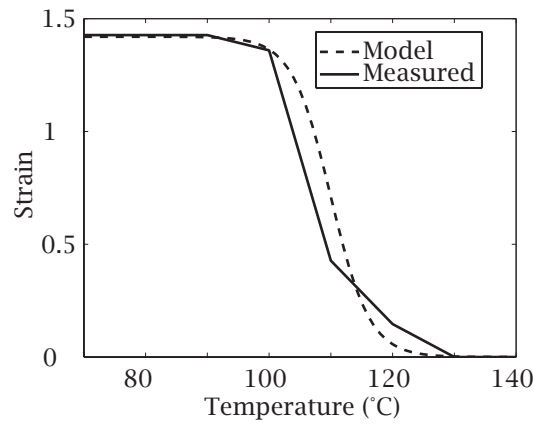


Figure C.2: The measured stress (solid line) indicates the resting strain of the PS as a function of the fully contracted length. The dashed line indicates our predicted lengths based on a $T_g = 105^\circ$ and $T_r = 15^\circ$

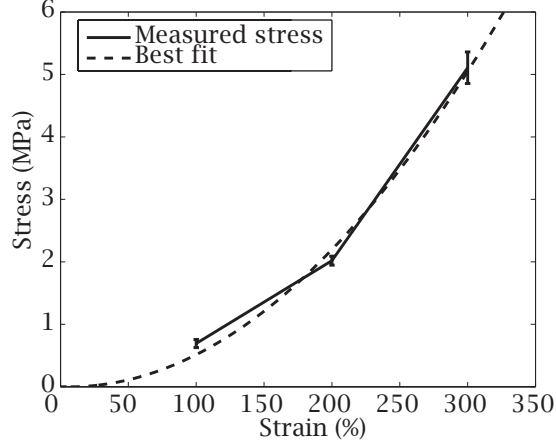


Figure C.3: The measured stress (solid line) of the polyolefin as a function of fixed strain after activation. A second order polynomial curve was fit to the data (dashed line). Error bars indicated standard deviation, $N=5$.

Rectangular samples of the PO were cut with a width of 40 mm and a length of 80 mm. Each sample was installed in a material testing machine (5544A, Instron) and clamped so that the length of the material between the clamps was 30 mm long. Each sample was heated with a heat gun until it had transitioned completely, and the peak stress of the material was recorded. This activation occurred within three seconds in order to minimize viscoelastic behavior. Five samples were measured, resulting in an average stress of 5.11 MPa with a standard deviation of 0.25 MPa.

To measure the contractile stress at different strains, a 30 mm length of the sample was clamped, and the clamps were then moved to 22.5 mm (to measure the stress at 200% strain) or 15 mm (for the stress at 100% strain) apart. This allowed the SMP to contract freely until reaching the target strain. Five samples were measured for each configuration.

The measured stress σ as a function of strain ϵ is displayed in Figure C.3. Because the unconstrained PO contracts to its resting length when activated, we expect that σ monotonically decreases until we reach complete contraction at 0% strain. However, the data indicates that σ and ϵ are not linearly related in this regime; the tangent modulus during initial contraction is higher than after partial relaxation. We fit the measured values to a second order polynomial (C.1) and used this to model the PO σ as a function of ϵ .

$$\sigma = (0.58\epsilon^2 - 0.07\epsilon) \text{ MPa} \quad (\text{C.1})$$

In each of these cases, the sample was fixed at a sufficient length that the sample was

allowed to contract freely in the orthogonal direction. However, in our hinges, the width of the PO is effectively fixed because it is clamped at both ends and the length is much smaller than the width. To determine if the aspect ratio of the PO sample affected the contractile stress, we ran additional experiments, clamping the PO at a length of 8 mm, replicating the aspect ratio of the PO in the hinges. We measured five samples and found that the PO clamped at an 8 mm length exerted a stress of 4.87 MPa, with a standard deviation of 0.25 MPa. This is similar to the stress measured in the PO clamped at 30 mm, indicating that the orthogonal contraction does not have a significant effect on the stress in the PO.

C.3 Angular Dependence of Hinge Torque

We generally solve for the torque exerted by a self-folding hinge in a flat and static state, and use this as a model for predicting whether or not a hinge will fold. We do this because we have observed experimentally that once a hinge begins to fold, it continues until either the motion is physically blocked or the SMP has contracted to its resting state. If this assumption is true, then as long as the initial torque is great enough to overcome gravity and begin the folding process, the hinge will fold to completion.

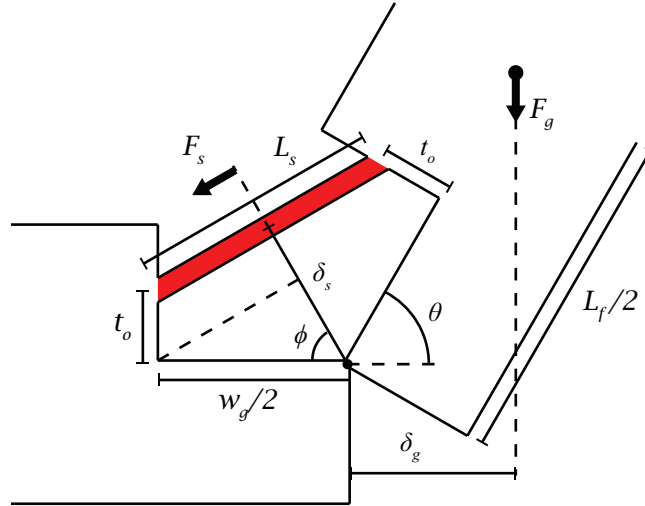


Figure C.4: A geometric model of torque due to SMP contraction as a function of hinge angle. Red indicates the contracting SMP. L_s is the length of the exposed SMP, F_s is the force exerted by the SMP layer, w_g is the gap width of the hinge, t_o is the offset distance of SMP layer from the flexural layer, L_f is the length of the folding face, δ_s is the distance of the SMP layer from the point of rotation, δ_g is the lever arm of the force of gravity F_g around the point of rotation, θ is the hinge angle, and ϕ is a dependent angle used in the model.

To justify this analytically, we consider the self-folding hinge at an arbitrary fold angle θ , experiencing a total torque τ_t that is the function of three separate components: a torque τ_s due to SMP contraction, a torque τ_g due to gravity, and a torque τ_h due to the stiffness of the flexural hinge (Fig. C.4). For the following equations, we have normalized each value to a hinge length of one meter, as this length affects each torque proportionally. At this angle, the length L_s of exposed SMP and the distance δ_s of that SMP from the hinge point can be calculated as a function of θ using an intermediary angle ϕ , as well as the gap width w_g and the offset distance between the SMP and the flexural layer t_o .

$$\phi = \frac{\pi - \theta}{2} \quad (\text{C.2})$$

$$L_s = 2 [(w/2) \sin(\phi) - t_o \cos(\phi)] \quad (\text{C.3})$$

$$\delta_s = t_o \sin(\phi) + (w/2) \cos(\phi) \quad (\text{C.4})$$

We use the shrink ratio S_R to calculate the resting length L_r and strain ϵ of the PO, and use the best-fit equation relating stress and strain (appendix A) to model the PO stress σ as a function of ϵ .

$$L_r = \frac{w}{S_R - 1} \quad (\text{C.5})$$

$$\epsilon = \frac{L_s - L_r}{L_r} \quad (\text{C.6})$$

$$F_s = t_s \sigma \quad (\text{C.7})$$

From these values we can calculate τ_s and τ_g .

$$\tau_s = F_s \delta_s \quad (\text{C.8})$$

$$F_g = g \rho_a L_f \quad (\text{C.9})$$

$$\delta_g = \frac{L_f}{2} \cos(\theta) \quad (\text{C.10})$$

$$\tau_g = \frac{g \rho_a L_f^2}{2} \cos(\theta) \quad (\text{C.11})$$

In the case of the composite in Chapter 6, the length of the flexing layer d_h is approx-

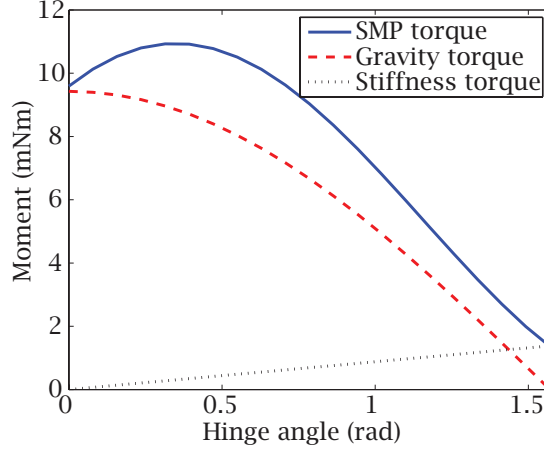


Figure C.5: The modeled torques exerted on the hinge due to SMP contraction (blue), gravity (red dashed), and hinge stiffness (black dotted) as a function of hinge angle for a representative hinge geometry (relevant values in Table C.1). This graph is for a hinge with a maximum possible face length, so the SMP torque and gravity torque are equal when the hinge is flat.

imately $100\text{ }\mu\text{m}$, which is due in part to the SMP delaminating from the substrate on the convex side. τ_h can be solved as a function of d_h , the curvature κ_h , the thickness t_h of the polyimide, and the Young's modulus E_h of the polyimide.

$$\kappa_h = \frac{\theta}{L_h} \quad (\text{C.12})$$

$$I_h = t_h^3/12 \quad (\text{C.13})$$

$$\tau_h = E_h I_h \kappa_h \quad (\text{C.14})$$

$$\tau_t = \tau_s - \tau_g - \tau_h \quad (\text{C.15})$$

Table C.1: Values used for calculating the hinge torque, gravity torque, and hinge stiffness in the millimeter-scale aluminum composite.

Value	Symbol	Value	Units
Polyolefin thickness	t_p	25	μm
Aluminum composite area density	ρ_a	636	g/m^2
Face length	L_f	55	mm
Offset thickness	t_o	76	μm
Shrink ratio	S_R	4	
Gap width	w_g	0.4	mm
Flexural thickness	t_h	7.5	μm
Flexural Young's modulus	E_h	2.5	GPa
Flexural length	d_h	100	μm

For the case of a typical hinge using the composite design presented in Chapter 6, we've plotted these three component torques as a function of hinge angle (Fig. C.5). In this graph the face length is set to be the maximum possible, so τ_s and τ_g are equal at 0 rad. This represents the maximum face size that can self-fold against gravity. The graph shows that τ_s initially increases as a function of fold angle, and then remains greater than τ_g , so if $\tau_t \geq 0$ in the hinge's flat state and the hinge begins folding, τ_t will only be larger at higher angles. The stiffness of the flexural layer is small but becomes significant at higher angles. Based on our observations, the hinges rarely stopped folding before reaching their mechanical stops, so we believe the stiffness never becomes great enough to stop folding. This may be due to the delamination between the flexural layer and the hinge. If delamination increases as fold angle increases, then d_h will also increase, decreasing the stiffness of the hinge and τ_h . This behavior would explain the large standard deviations we see when folding extremely high angles. If some of these hinges delaminated and others didn't, we would see some hinges fold completely and others stop prematurely.

The model here does indicate that we cannot assume that all hinge geometries will fold to completion. If w_g or S_r are too small, or t_o is too large, τ_s will fall below τ_g before reaching a 90° angle.

Manufacturing Estimates

D.1 3D Printing

We estimate the cost associated with both industrial and consumer-grade 3D printers in our comparison. Our example industrial printer is an Objet30 Scholar 3D printer, the cheaper of two printers our lab has access to. Printing the crane would consume 390 g of build material and 150 g of support material at a cost of $\$0.50 \text{ g}^{-1}$ (based on the prices paid in our lab), ignoring power consumption. This results in a part cost of \$270. The printing job would take 21 hours.

For a consumer-grade printer we used the Form-1 printer, currently available for \$3000. Printing this piece requires 7 hours and 275 mL of material. The polymer costs \$150 per liter, for a material cost of \$41 for each piece. This printer is cheaper and faster than an industrial printer, but has less material options, is less precise, and in our experience is less reliable. Both of these estimates are provided by the printing software written by the printer manufacturer.

D.2 Injection Molding

To estimate the cost of injection molding a plastic crane, we assume the geometry is a hollow shell with the same shape as the folded crane. Given a thickness of 2 mm and a surface area of $19\,200 \text{ mm}^2$, this requires $38\,400 \text{ mm}^3$ of material. The density of thermoplastics is approximately 1000 kg/m^3 and thermoplastics cost \$1 to \$10/kg, so we estimate each crane to cost about \$0.20 in material.

The time to injection mold each part depends on several factors, and equations for estimating the injection time can be found in Boothroyd et al. [152]. The injection cycle can be separated into three phases: The injection time t_f , the cooling time t_c , and the resetting time t_r .

$$t_f = \frac{2V_s p_j}{P_j} \text{ s} = 0.3 \text{ s} \quad (\text{D.1})$$

$$t_c = \frac{h_{max}^2}{\pi^2 \alpha} \ln \frac{4(T_i - T_m)}{(T_x - T_m)} \text{ s} = 22.3 \text{ s} \quad (\text{D.2})$$

$$t_r = 5 \text{ s} \quad (\text{D.3})$$

$$(\text{D.4})$$

We assume that operation of these machines costs \$40 per hour [152], the injection cycle takes a total of 28 s, so the per-part operation cost is \$0.28 and the full per-part cost is \$0.49.

For our estimates, we assume a typical injection molding machine with a clamping force of 1100 kN, a maximum clamp stroke of 37 cm, and a driving power P_j of 22 kW [152]. We use high-impact polystyrene as our example material because its properties result in a relatively fast production time.

The setup cost of an injection molding process is dominated by fabrication of the mold. The cost of machining the mold C_m can also be estimated using equations from Boothroyd et al. [152]. This cost can be expressed as a function of many factors, including the mold-making hours M_b , the ejector pin hours M_e , the hours due to complexity M_x , the hours due to size M_{po} .

$$M_b = 50 + 0.023 A_c h_p^{0.4} \text{ h} \quad (\text{D.5})$$

$$M_e = 2.5 A_p^{0.5} \text{ h} \quad (\text{D.6})$$

$$M_x = 5.83 (X_i + X_o)^{1.27} \text{ h} \quad (\text{D.7})$$

$$M_{po} = 5 + 0.085 A_p^{1.2} \text{ h} \quad (\text{D.8})$$

$$C_m = (M_b + M_e + M_x + M_{po}) f_a C_L \quad (\text{D.9})$$

From these equations we estimate that the time required to make the mold is 196 h and the cost is \$7.8k.

Table D.1: Values for estimating injection molding time and cost.

Symbol	Value	Description
t_f	0.5 s	injection time
t_c	22 s	cooling time
V_s	38.4 cm ³	shot volume
p_j	96.5 MPa[152]	injection pressure
P_j	22 kW[152]	injection power
h_{max}	2 mm	maximum thickness
α	0.09 mm ² /s [152]	thermal diffusivity
T_i	218 °C [152]	injection temperature
T_m	27 °C [152]	mold temperature
T_x	77 °C [152]	ejection temperature
M_b	84 h	base mold-making hours
M_e	51 h	ejection mold-making hours
M_x	26 h	complexity mold-making hours
M_{po}	121 h	size mold-making hours
A_c	410 cm ²	area of mold cavity plate
A_p	410 cm ²	area of project part
h_p	24.4 cm	combined plate thickness
X_i	1.6	inner complexity
X_o	1.6	outer complexity
f_a	1.1 [152]	appearance factor
C_L	\$40 h ⁻¹ [152]	cost of labor
C_m	\$12400	total mold cost

D.3 Milling

For our analysis we consider a computerized numerical cutting (CNC) three-axis milling system operating on aluminum. A CNC mill can remove 1500 to 7000 mm³/s of aluminum [153]. Assuming that our crane is cut from a single block of aluminum with a volume of 1.50×10^6 mm³ and the final product has a volume of 2.3×10^5 mm³, the mill will need to remove 1.27×10^6 mm³, taking 3 to 15 minutes. In addition, it takes approximately 45 minutes to set up one machine and approximately 30 minutes to program for cutting the geometry of the crane [153]. The starting block is estimated to cost \$16 to \$40 [152].

D.4 Sheet Metal Stamping

For these estimates we assume the crane will be bent from a 0.5 mm thick sheet of steel. The area of the raw material needed for a single crane is 420 cm², and the cost of a steel sheet at this thickness is about \$0.79/kg, so the raw material for each crane would cost a total of \$0.13.

The part would be manufactured by a pair of press-brake machines in series, one for

shearing and one for bending. Based on equations provided by Boothroyd et al. [152] we can estimate the time and money required to set up the manufacturing line and produce each unit.

The shear die manufacturing time M_s can be broken into a few different components. It is dependent on the base die machining time M_{ds} , the time due to the perimeter complexity M_{p0} , and additional factors accounting for the die plate thickness f_p , the plan area $f_L W$, and the die-type f_d .

$$M_{ds} = 3 + 0.009 A_u \text{ h} \quad (\text{D.10})$$

$$h_p = 9 + 2.5 \ln \left(\frac{U}{U_{lc}} V h^2 \right) \text{ mm} \quad (\text{D.11})$$

$$f_p = 0.5 + 0.02 h_p \quad (\text{D.12})$$

$$X_p = \frac{P}{\sqrt{LW}} \quad (\text{D.13})$$

$$M_{p0} = f_d (28 + 1.03 X_p) \text{ h} \quad (\text{D.14})$$

$$M_s = f_p (f_{LW} f_d M_{p0} + M_{ds}) \text{ h} \quad (\text{D.15})$$

$$C_s = M_p \$40 \text{ h}^{-1} \quad (\text{D.16})$$

The bending die is a separate machine which transforms the sheared piece. The cost C_b of the bending die can be estimated from the following set of equations:

$$f_d = 0.9 + 0.02 D \quad (\text{D.17})$$

$$M_{p0} = f_d (18 + .023 L W) \text{ h} \quad (\text{D.18})$$

$$M_{pn} = 0.68 L_b + 5.8 N_b \text{ h} \quad (\text{D.19})$$

$$M_b = M_{pn} + M_{p0} \quad (\text{D.20})$$

$$C_b = M_p C_L \quad (\text{D.21})$$

The total machinery setup time and cost is $M_s + M_b = 184 \text{ h}$ and $C_s + C_b = \$7.4\text{k}$, respectively.

A typical 200 kN press has a speed of 100 strokes per minute, and a typical operating cost of \$55 per hour [152]. This indicates that operating these two machines will cost \$0.02 per unit. Including material cost, each unit will have a total production cost of \$0.15.

Table D.2: Values for estimating sheet metalworking time and cost.

Symbol	Value	Description
M_{ds}	6.78 h	base die set time
M_{p0}	32.44 h	perimeter complexity time
M_s	12.5 mm	total shear die time
h_p	6.78 h	die plate thickness
f_p	0.75	thickness factor
X_p	4.3	complexity index
U	$4.4 \times 10^5 \text{ kN/m}^2$ [152]	ultimate tensile stress
U_{lc}	$4.4 \times 10^5 \text{ kN/m}^2$ [152]	ultimate tensile stress of low-carbon steel
V	100	production volume, in thousands
h	0.5 mm	sheet metal thickness
P	88.3 cm	perimeter length
L	20.5 cm	rectangular length
W	20.5 cm	rectangular width
f_d	1 [152]	die-type factor
f_{LW}	3 [152]	plan area correction factor
L_b	83 cm	total length of bends
N_b	19	number of bends
C_L	$\$40 \text{ h}^{-1}$ [152]	cost of labor

D.5 Resistive Self-Folding

The total cost of the composite is $\$570/\text{m}^2$ (Appendix A), and the area of the composite is $42 \times 10^3 \text{ mm}^2$, resulting in a total material cost of $\$24$, based on the prices we paid in lab. At high volumes we expect these costs to be roughly half of that. The assembly process takes approximately one hour by hand, but does not require special training or safety considerations. In addition, the process is primarily one of cutting and laminating layers, which could be easily automated.

The equipment required for this process includes three pieces of equipment. The most expensive component is a laser cutter. We used a Universal Laser Systems VLS 2.30, which cost us $\$11\,700$. We also require a power supply capable of supplying up to three amperes, and a ferric chloride etch tank. Each of these items can be purchased for $\$500$.

D.6 Oven Self-Folding

The cost for the oven-activated composite is much less than for the current-activated composite due to having fewer layers. In particular, this composite does not have a flexible circuit board, which is the most expensive component of the current-activated composite. The composite cost is $\$37/\text{m}^2$ (Appendix A), and the total area is the same as for the

current-activated folding sample, resulting in a material cost of \$2.

Machining this composite requires the same laser machining system as for the current-activated folding, but instead of a power supply and an etch tank, it requires an oven or hot plate. These are also available for less than \$500.